Fermi National Accelerator Laboratory

FERMILAB-Pub-87/217-E
[E-537]

High Mass Dimuon Production in $\bar{p}N$ and $\pi^{-}N$ Interactions at 125 GeV/c*

E. Anassontzis, S. Katsanevas, P. Kostarakis, C. Kourkoumelis, A. Markou, L. K. Resvanis, and G. Voulgaris
University of Athens
Athens, Greece

M. Binkley, B. Cox, J. Enagonio[a], C. Hojvat, D. Judd[b], R. D. Kephart, P. K. Malhotra[c], P. O. Mazur, C. T. Murphy F. Turkot, R. L. Wagner, D. Wagoner[b], and W. Yang
Fermi National Accelerator Laboratory
Batavia, Illinois 60510

H. Areti[d], S. Conetti, P. Lebrun[d], D. G. Ryan, T. Ryan[e], W. Schappert[f], and D. G. Stairs
McGill University
Montreal, Quebec, H3A 2T8, Canada

C. Akerlof, X. Cui, P. Kraushaar[g], D. Nitz, R. Thun, and L. Wang
University of Michigan
Ann Arbor, Michigan 48109

He Mao, Zhang Nai-jian
Shandong University
Jinan, Shandong
Peoples Republic of China

December 1987

*Submitted to Phys. Rev. D.

Operated by Universities Research Association Inc. under contract with the United States Department of Energy

HIGH MASS DIMUON PRODUCTION IN $\bar{p}N$ AND π^-N INTERACTIONS AT 125 GEV/C

E. Anassontzis, S. Katsanevas, P. Kostarakis, C. Kourkoumelis, A. Markou, L. K. Resvanis, and G. Voulgaris
University of Athens, Athens, Greece

M. Binkley, B. Cox, J. Enagonio[a], C. Hojvat, D. Judd[b], R. D. Kephart, P. K. Malhotra[c], P. O. Mazur, C. T. Murphy, F. Turkot, R. L. Wagner, D. Wagoner[b], and W. Yang
Fermi National Accelerator Laboratory, Batavia, Illinois 60510

H. Areti[d], S. Conetti, P. Lebrun[d], D. G. Ryan, T. Ryan[e], W. Schappert[f], and D. G. Stairs
McGill University, Montreal, Quebec H3A 2T8, Canada

C. Akerlof, X. Cui, P. Kraushaar[g], D. Nitz, R. Thun, and L. Wang
University of Michigan, Ann Arbor, Michigan 48109

He Mao and Zhang Nai-jian
Shandong University, Jinan, Shandong, Peoples Republic of China

ABSTRACT

Muon pairs with invariant mass between 4 and 9 GeV/c² have been produced in $\bar{p}N$ and π^-N interactions at an incident momentum of 125 GeV/c. The experiment was performed at Fermilab using a tungsten target and special beam enriched to contain 18% antiprotons. Differential distributions as functions of the dimuon invariant mass, Feynman-x, transverse momentum, and the decay angles of the dimuon are compared to the predictions of the Drell-Yan model including QCD corrections, and quark structure functions for the $\bar{p}$ and π^- are extracted. Comparisons of the antiproton data to the Drell-Yan model are particularly valuable because accurate valence quark structure functions from deep inelastic scattering measurements were used in the model calculations. The measured absolute cross sections require K-factors of 2.41 and 2.57 for the $\bar{p}$ and π^- respectively when compared to the naive Drell-Yan calculation.

I) INTRODUCTION

The comparison of experimental data with the predictions of the Drell-Yan mechanism for high mass lepton pair production in hadronic collisions provides a stringent test of simple quark-parton model ideas and the various QCD extensions required.[1,2,3] A study of the process $\bar{p}N\to\mu^+\mu^-X$ is particularly valuable because the cross section for this reaction is dominated by the annihilation of valence quarks and antiquarks whose structure functions have been accurately determined in deep inelastic lepton scattering (DIS) experiments.[4] Figure 1 shows the Feynman diagrams for the Drell-Yan process and its first order QCD corrections. In the leading log approximation of QCD, the cross section for hadronic muon pair production, integrated over the transverse momentum, p_T, of the dimuon, is given by[5]

$$\frac{d^2\sigma}{dMdx_F} = \frac{8\pi\alpha^2}{9M^3}\frac{(1-\tau)}{[x_F^2(1-\tau)^2+4\tau]^{\frac{1}{2}}}\sum_{q=u,d,s} e_q^2[\bar{q}^B(x_1,Q^2)\bullet q^T(x_2,Q^2) + q^B(x_1,Q^2)\bullet\bar{q}^T(x_2,Q^2)], \tag{1}$$

where M is the invariant mass of the muon pair, $\tau=M^2/s=x_1x_2$, $x_F=2p_L/[\sqrt{s}(1-\tau)]$ is the ratio of the longitudinal momentum of the pair to the maximum allowable momentum in the center of mass frame, e_q is the quark charge, x_1 (x_2) is the momentum fraction of the beam (target) particle carried by the interacting quark, and the $q(x,Q^2)$'s are the beam (B) and target (T) quark structure functions of the interacting hadrons. The quark structure functions should be identical to those measured in deep inelastic lepton scattering experiments at space-like values of Q^2 which are continued to the time-like region by making the identification $Q^2 = M^2$. Theoretical studies[6] have shown that the Drell-Yan cross section factorizes into functions of x_1 and x_2 to second order in QCD, reaffirming the validity of

(1).

First order QCD corrections[7] [Figures 1(b)-1(d)] are expected to increase the observed cross section over that of (1) by a factor which is nearly constant in the region of x_1 and x_2 probed by current experiments ($0.1<x_{1,2}<0.9$). This "K-factor" is substantial (1.5 to 2.5) and roughly independent of particle type. The first order QCD annihilation and Compton diagrams also contribute to the p_T of the dimuon. However, predictions of these diagrams require an unrealistically large value of the quark intrinsic p_T in order to fit existing pion and proton data, and (particularly in the case of the pion) predicts too small an increase of $\langle p_T^2 \rangle$ with s.[8] The perturbative calculation of annihilation and Compton diagrams is, in fact, only valid for $p_T \geq M$, while most of the data exists at much lower values of p_T. Calculations[9] which include the effects of soft gluon emission predict p_T distributions which require only a modest value of intrinsic p_T to reproduce the pion and proton data. These soft gluon graphs do not alter the first order K-factor in the region of the scaling variable τ probed by current experiments.

The primary goal of the present experiment is a comparison of the reaction $\bar{p}N \to \mu^+\mu^- X$ with (1) and higher order corrections calculated using quark structure functions measured in DIS. Data from the reaction $\pi^- N \to \mu^+\mu^- X$ are used to make detailed scaling checks of $M^3 d\sigma/dM dx_F$ as functions of τ and x_F by comparing with data from other experiments at different energies. Quark structure functions are extracted from both the $\bar{p}$ and π^- data, and a best estimate of the K-factor in the pion reaction is made via this procedure. The measured p_T distributions are compared to the QCD predictions, and the decay angular distributions of the dimuon are checked for consistency with the naive Drell-Yan model.

II) APPARATUS AND EVENT RECONSTRUCTION

A detailed description of the beam, experimental apparatus, and event reconstruction can be found elsewhere.[10] The experiment used a special tertiary beam of mean momentum 125 GeV/c and composed of 18% antiprotons and 82% pions resulting from $\bar{\Lambda}^0$, Λ^0, and K^0_S decays. The experiment normally operated at a beam intensity of 1.5×10^7 particles/sec. Incident pions as well as incident antiprotons were tagged by Cerenkov counters, resulting in less than 0.5% pion contamination of the antiproton data. Beam hodoscopes and proportional chambers were used to measure the trajectory and momentum of each incident beam particle.

Figure 2 shows the experimental spectrometer which included a tungsten target (0.416, 0.998, or 1.50 $\bar{p}$ absorption lengths), a 10.3 absorption length copper hadron absorber, 20 proportional and drift chamber planes, a large aperture analysis magnet, a two layer x-y charged particle scintillation counter hodoscope (180 elements), and a 13.2 absorption length steel and concrete muon detector with three scintillation counter hodoscope muon trigger planes of 60 elements each. The individual elements of the muon hodoscope planes were aligned so that a threefold coincidence between planes would point back to the target. The fast dimuon trigger required two threefold coincidences in the three muon hodoscope planes, at least two hits in the charged particle scintillation counter hodoscope, and a $\bar{p}$ or π^- signal from the beam tagging system. Events which produced a fast trigger were sent to an ECL-CAMAC trigger processor.[11] The processor used hits (within fiducial regions defined by the threefold coincidences) from the drift chambers downstream of the analysis magnet to calculate the momenta of muon candidates and subsequently the masses of all possible muon pairs in less than 10 μsec. Events with dimuon candidates of invariant mass greater than 2.0 GeV/c^2 were recorded on magnetic tape.

The offline analysis program reconstructed track segments in the drift chambers both upstream and downstream of the magnet and assumed a horizontal bend plane at the magnetic center to determine the momentum for matching segments. The 250 micron measured resolution of the drift chambers and the measured field integral of 2766 kG-cm resulted in a momentum resolution of $\Delta p/p=0.004p$. This momentum resolution contributed a negligible amount to the observed ψ mass resolution, which was dominated by uncertainty in the dimuon opening angle measurement due to multiple scattering in the target and hadron absorber.

Events which had at least two muon candidates with an invariant mass greater than 2.0 GeV/c^2 were subject to a second stage of reconstruction. Information from the beam chambers was used to determine the four momentum of the incident beam particle causing the interaction. This was combined with track coordinates from the absorber MWPC and upstream drift chambers to distinguish events originating in the target from events originating in the dump using an algorithm similar to that of Reference 12. The measurements of the positions and angles of the muons as they exited from the absorber and the positions of the muons as measured by the absorber chamber MWPC were used to calculate a probability function which depended on the vertex coordinates of the event and the initial angles of the muons before they entered the absorber. The probability function, which included measurement errors and multiple scattering in the absorber, was maximized as a function of the z coordinate of the vertex and the initial angles of the muons. The transverse coordinates of the interaction vertex were determined from the reconstructed incident beam track. The z coordinate distribution resulting from this fitting procedure is shown in Figure 3 for the 1.5 $\bar{p}$ absorption length (14.71 cm) tungsten target.

Requirements were also placed on the distance between the two tracks at the reconstructed vertex and on the position of the vertex to ensure that the muons did originate at a common point and were not the result of an accidental coincidence between a beam halo particle and a muon from the decay of a hadron. The reconstructed vertex was required to be within ± 9.144 cm in x and ± 10.16 cm in y of the nominal beam center at the target, that is, $x = 0.0$ cm and $y = 5.08$ cm. As shown in Figure 3, the z coordinate of the reconstructed vertex was required to be between -444.3 cm and -358.14 cm. These vertex requirements were tested in the Monte Carlo simulation, resulting in a loss of less than 1 percent of the real events with no bias as a function of any kinematic variable.

Events which reconstructed to the target region were reanalyzed assuming that the z coordinate of the production vertex was at the center of the target. This procedure improved the ψ mass resolution (for the 1.5 absorption length tungsten target) from σ=270 MeV/c^2 to σ=185 MeV/c^2. The comparable resolution for the 0.5 absorption length tungsten target was σ=140 MeV/c^2. The invariant mass spectra for both like-sign and opposite-sign dimuons produced in $\bar{p}$ and π^- interactions in the 1.5 absorption length target are shown in Figures 4(a) and 4(b) respectively. Data was taken with three different target lengths and Table I gives the integrated $\bar{p}$ and π^- beam fluxes and number of reconstructed events in the high mass continuum region ($4<M<9$ GeV/c^2) for each target.

III) CORRECTIONS TO THE DATA

Corrections were applied to the data for trigger processor inefficiency(1%), for scintillation counter inefficiency and gaps between adjacent counters (10%), and for vertex cut inefficiency(1%).[10] This section covers the additional corrections for muon energy loss in the spectrometer, for contamination by random muon pairs, for ψ and ψ' resonance tails in the high mass continuum region, and for reinteraction in the target. The corrections for Fermi Motion and track finding inefficiency were incorporated into the Monte Carlo acceptance program, which is the topic of Section IV.

A) MUON ENERGY LOSS IN THE SPECTROMETER

Muon track momenta were corrected for energy loss in the tungsten target and copper absorber using tables calculated from the Bethe-Bloch ionization formula with corrections for density effects, bremsstrahlung, and nuclear interactions.[13,14] The Monte Carlo program which simulated the acceptance and trigger logic included additional corrections for muon energy loss in the concrete and steel muon filter. The calculated values of energy loss for tungsten, copper, beryllium, iron, and concrete were parameterized for kinetic energies between 100 MeV and 125 GeV, and are plotted in Figure 5. The parameterization for iron was compared with other data in the literature[15,16] and all were found to agree to better than 1% for muon energies in the range of interest.

B) CONTAMINATION BY RANDOM MUON PAIRS

The number of like-sign events with masses between 4 and 9 GeV/c^2 is 1.5% of the opposite-sign sample in both the $\bar{p}$ and π^- data (Fig. 4). All of the like-sign events between 4 and 9 GeV/c^2 are negatively charged muon pairs produced by random coincidences between one relatively high momentum (between 20 and 125 GeV/c) halo muon which passed through the beam hole in the halo veto counters[10] and a low momentum (less than 10 GeV/c) muon from the decay of a pion or kaon which was produced in an interaction in the target.

By studying events with vertices outside the cuts used to define true dimuon events, we found that the number of random events observed with a positive decay muon accompanying the negative beam halo muon was equal within statistics to the similar sample with two negative muons. We therefore corrected our opposite-sign event sample by subtracting from it the like-sign events in all the distributions presented in this paper. The number of like-sign events was limited to 1.5% by using the vertex cuts and by rejecting events with a muon of momentum greater than 85 GeV/c.[17] The 85 GeV/c cut introduces a slight bias against events with very high x_F, but this was taken into account by making an identical cut in the Monte Carlo acceptance program. All accidental events fall near the region $\cos\theta = -1$, where the acceptance for true dimuon events is small (see Section IX).

C) CONTAMINATION BY THE ψ AND ψ' RESONANCES

Fits to the mass region between 2.6 and 4.5 GeV/c^2 with Gaussians centered at the ψ and ψ' masses and an exponentially falling background gave a production ratio of $\psi'/\psi = 0.02\pm0.01$ for both the $\bar{p}$ and π^- data. The contamination of the continuum above 4 GeV/c^2 by resonance tails was calculated using the Gaussians fits to be negligible for the ψ and $2.4\pm1.2\%$ for the ψ'. Two checks were made to insure that no significant non-Gaussian tails were introduced by the event reconstruction. First, the χ^2's of individual tracks from events at the ψ resonance and from events above 4 GeV/c^2 were compared and found to be identical. Second, simulated ψ and ψ' events were generated in the Monte Carlo acceptance program which included multiple scattering, real background tracks, and inefficiencies in the chambers, all of which may cause track distortions. These simulated events were reconstructed with the same programs that were used for data events and no evidence of a non-Gaussian tail was found.

D) REINTERACTION IN THE TARGET

The correction required for events produced by secondary interactions in the target was determined by comparing the cross sections for ψ's produced by pions from the different length tungsten targets. If tertiary interactions are ignored and the absorption cross section is assumed to be independent of energy, the measured cross section should depend on the length of the target as

$$\sigma_{\mathrm{Measured}}=\sigma_{\mathrm{Direct}}+\sigma_{\mathrm{Reint}}\{1 - \frac{(L/\lambda_{\mathrm{Abs}})}{[\exp(L/\lambda_{\mathrm{Abs}})-1]}\},$$

where L is the physical length, λ_{Abs} is the absorption length of the target material, σ_{Direct} is the cross section that would be measured using an infinitesimally thin target, and σ_{Reint} is a constant that depends on the details of the reinteraction but is independent of the target length. Measured cross sections for different length targets can therefore be used to obtain values for σ_{Direct} and σ_{Reint}.

The relative rates for ψ production by pions are shown as a function of target length in Figure 6. The fitted curve is the above parameterization of the cross section as a function of target length. Its intercept at zero target length gives the cross section for direct production of ψ's.

The Monte Carlo program CASIM[18] was used to compare pion produced ψ events and high mass continuum events in order to estimate the reinteraction correction for the continuum region. CASIM uses the Hagedorn-Ranft thermodynamic model to generate a spectrum of secondary particles. The known τ dependences of the ψ and Drell-Yan cross sections[19] were used to generate high mass muon pair events from this spectrum of secondaries. The muon pairs were propagated through the spectrometer using the Monte Carlo acceptance program which then allowed the reinteraction rate for the high mass region to be determined relative to ψ's produced by pions. The resulting correction factors for the cross sections with various target and beam combinations are given in Table I. The size of the overall correction is less than 5 percent for the high mass antiproton produced data and less than 4 percent for the pion data. Uncertainties in these corrections lead to a 2 percent uncertainty in the final cross sections.

IV) MONTE CARLO ACCEPTANCE PROGRAM

The acceptance of the apparatus was calculated with a Monte Carlo program. Events were generated randomly throughout phase space using the measured beam energy spectrum and profile and allowing for Fermi motion of the target nucleon. The resulting pairs of muons were propagated through the spectrometer taking into account multiple scattering and energy loss. The track coordinates at the chambers were digitized, the counter hits were tagged, and the results were recorded in the same format used for the data tapes. Background hits in the chambers were included to introduce electronics dead time and thus produce the same track finding efficiency as for real data events. The Monte Carlo events were then subject to the same set of analysis programs as the data, and both the initial and reconstructed values of the kinematic variables were saved. Using the maximum likelihood method, the Monte Carlo events were fit to the unbinned data events and reweighted to accurately simulate the acceptance as a function of all kinematic variables.

A) FERMI MOTION CORRECTION

The four-vector for the target nucleon was generated according to a simple Fermi gas model[20] to allow for motion of the nucleons inside the nucleus. The target nucleon was given an isotropic angular distribution in the laboratory frame and a momentum between 0 and the Fermi momentum distributed as $dN/dp = 3p^2/p^3_{Fermi}$. The Fermi momentum for the tungsten target was taken to be[21] p_{Fermi} = 265 MeV/c. High momentum tails[22] in the Fermi distribution were investigated in the simulation and found to have no significant effect.

B) TRACK FINDING EFFICIENCY

Background tracks which accompanied true dimuon events could be caused by beam halo particles or other interactions in the copper absorber. These sometimes produced inactive wires due to the 300ns discriminator dead time as well as backround wire hits. Both effects were simulated in the Monte Carlo program by including drift chamber hits (and hence inactive wires) from special data runs taken using only the beam signal as a trigger.[17] Good agreement was observed between the backgrounds in reconstructed dimuon data events and the backgrounds in Monte Carlo generated events which survived the reconstruction procedure. The overall efficiency for finding both tracks in a high mass dimuon event was 90% and is shown as a function of M and x_F in Figure 7. It is nearly constant over the measured range of all kinematic variables, the only exception being a decrease for large values of x_F. The overall systematic error introduced by the track finding correction is less than 4%.

C) ACCEPTANCE CALCULATION AND EMPIRICAL FITS TO THE DATA

The unbinned data events and reconstructed Monte Carlo events were used to fit the dependence of the cross section on the kinematic variables M, x_F, p_T, $\cos\theta$, and ϕ using the maximum likelihood method.[28] The cross section (by which the Monte Carlo events were initially generated and thereafter reweighted) was parameterized as a product of simple functional forms of each variable and the fit found the set of parameters which maximized the probability of observing the experimental data points obtained. This was accomplished by maximizing the product of likelihood functions $L(x_i|\Gamma)$ for individual data events, that is,

$$L(x|\Gamma) = \Pi_{i=1}^{N} L(x_i|\Gamma),$$

where N is the number of data events, $x_i = (M_i, x_{Fi}, p_{Ti}, \cos\theta_i, \phi_i)$ are the kinematic variables for the i^{th} event, Γ represents the set of parameters being fit, and the likelihood function is defined by

$$L(x_i|\Gamma) = P(x_i|\Gamma)\,[\int P(x|\Gamma)dx]^{-1},$$

where $P(x_i|\Gamma)$ is the multidimensional functional form being fit to the data points. The denominator of the likelihood function was evaluated using the Monte Carlo events, which were reweighted at each step of the fit.

Good fits to both the $\bar{p}$ and π^- high mass continuum data were obtained using the form

$$P(x|\Gamma)=P(M|\alpha_M)\bullet P(x_F|x_{F0},\sigma_x)\bullet P(p_T|p_{T0})\bullet P(\cos\theta|\lambda)\bullet P(\phi),$$

where

$$P(M|\alpha_M)=\alpha_M \exp(-\alpha_M M)\ [\exp(-\alpha_M M_{MIN})-\exp(-\alpha_M M_{MAX})]^{-1},$$

$$P(x_F|x_{F0},\sigma_x)=\sqrt{2/\pi}\ \exp(-0.5z^2)\ dz/dx_F$$

with $z=(1/\sigma_x)\{\ln[(x_F+1)/(1-x_F)]-\ln[(x_{F0}+1)/(1-x_{F0})]\}$,

$$P(p_T|p_{T0})=2(p_T/p_{T0})\sqrt{2/\pi}\ \exp[-0.5(p_T/p_{T0})^2],$$

$$P(\cos\theta|\lambda)=\{1/[2(1+\lambda/3)]\}\bullet(1+\lambda\ \cos^2\theta),\ \text{and}$$

$$P(\phi)=1/(2\pi).$$

The x_F distribution is a transformed Gaussian which vanishes at the kinematic limits, $x_F = \pm 1$. The polar and azimuthal decay angles, θ and ϕ, of the positive muon were defined in the Gottfried-Jackson rest frame.[24] Tables II(a) and II(b) give the results of fits with λ free and with $\lambda = 1$ as predicted by the Drell-Yan model. The fits with $\lambda = 1$ were used to generate acceptances as functions of the kinematic variables as shown for the $\bar{p}$ data in Figure 8. The acceptance for a bin from x_i to $x_i+\Delta x$ was defined as the ratio of the weighted number of accepted Monte Carlo events with a reconstructed value of x between x_i and $x_i + \Delta x$ to the weighted number of generated events with x between x_i and $x_i + \Delta x$. Calculating the acceptance in this manner compensated for smearing of the kinematic quantities due to Fermi motion of the target nucleon and apparatus resolution.

V) CROSS SECTIONS

The differential cross section for each value of the kinematic variable x was calculated using the formula

$$d\sigma/dx=(R\bullet N_{Events})/(\Delta x\bullet N_0\bullet \rho\bullet L_{Eff}\bullet \xi\bullet E\bullet N_{Beam}),$$

where x is one of the kinematic variables (M, x_F, or p_T), $d\sigma/dx$ is the differential cross section in cm^2/nucleon assuming an A dependence of A^1, Δx is the width of the bin, A is the atomic mass of the target, N_0 is Avogadro's number, ρ is the density of the target in gm/cm^3, L_{Eff} is the effective length of the target, R is the correction for reinteraction and resonance contamination, ξ is the acceptance for the bin, E is the correction for counter and trigger efficiency, N_{Events} is the number of data events in the bin, and N_{Beam} is the number of beam particles hitting the target.

Before presenting the data, we will briefly describe the calculation of the effective length of the target and discuss the assumption that the cross section varies with the atomic mass of the target as A^1.

A) EFFECTIVE LENGTH OF THE TARGET

Each of the tungsten targets was carefully weighed and measured, and its effective length, L_{Eff}, was calculated from

$$L_{Eff} = \lambda_{Abs}\ [1-\exp(-L/\lambda_{Abs})],$$

where $\lambda_{Abs} = \sigma_{Abs}\bullet\rho\bullet N_0\bullet A$ is the absorption length of the target material, L is the physical length of the target, and σ_{Abs} is the absorption cross section. The absorption cross sections for antiproton and pion beams in tungsten were interpolated from measurements made at beam energies of 60 and 200 GeV.[25] The errors in the measured absorption cross sections contribute a 1.7% uncertainty to the effective lengths and thus to our quoted cross sections.

B) A DEPENDENCE OF THE DRELL-YAN CROSS SECTION

As is well known, the total cross section for hadronic interactions in nuclei grows approximately as $A^{2/3}$. This is explained by the shadowing of the interior of the nucleus by the surface, and is thus dependent on the large strength of the hadronic interaction. In 1975 Farrar[26] proposed a model for strong interactions in nuclei which predicted that at high mass the Drell-Yan cross section should vary as A^1. The model assumed that the intrinsic strength of the strong interaction (i.e., the quark-gluon and gluon-gluon coupling) is small, with the apparent large strength of most hadronic processes being due to multiple interactions of quarks with small relative momenta over a long period of time. The fastest moving quarks will probably not interact and propagate freely through the nucleus. Infrequently, the fast quarks will annihilate to produce a high mass muon pair. Farrar estimated that the threshold for A^1 behavior would occur in the dimuon mass range between 2 and 6 GeV/c^2.

Kenyon[3] has reviewed subsequent high statistics A-dependence measurements using pion and proton beams showing that, for values of invariant mass greater than 4 GeV/c^2, the dimuon cross section increases as A^1 independent of M, x_F, and p_T in agreement with Farrar's prediction. From Kenyon's summary, we estimate the current experimental uncertainty in the power α of A^α to be ±2%, which corresponds to a ±11% uncertainty in the cross section per nucleon extracted from tungsten data. A recent publication by the NA10 collaboration[27] of very high statistics π^- data reports an overall A-dependence consistent with α=1.00±0.02, but notes a decrease in the tungsten to deuterium production at high x_2 consistent with the EMC effect in DIS. However, the effect is small compared to the statistical accuracy of our data at the relevant x_2 values. The error in the cross sections due to the uncertainty in the A-dependence correction will be indicated separately. Note that the cross sections given are per average nucleon which, for tungsten, is 40% proton and 60% neutron.

C) DATA AND OVERALL SYSTEMATIC ERROR

The differential cross sections as functions of M, x_F, and p_T^2 are shown in Figure 9. Values of the double differential cross sections in terms of (M,x_F), (M,p_T^2), and (x_F,p_T^2) are given in Table III. The errors shown in the figures and table are statistical only. The total integrated cross sections for $x_F>0$, $p_T>0$ and $4<M<9$ GeV/c^2 are $0.106\pm0.005\pm0.008$ nb/nucleon for the $\bar{p}$ induced reaction and $0.107\pm0.003\pm0.009$ nb/nucleon for the π^- induced reaction. The first error quoted is statistical and the second is systematic. In addition, there is an uncertainty due to the A dependence correction of $\pm11\%$. A breakdown of the experimental systematic error is given in Table IV. For the differential cross sections, we estimate any additional relative systematic error between extreme values of the variables to be less than 10%.

At our beam momentum of 125 GeV/c, the total cross sections and the differential cross sections as functions of M and p_T^2 are very similar for the $\bar{p}$ and π^- data. However, the pion data exhibits a substantially flatter dependence on x_F $[=(x_1-x_2)/(1-\tau)]$, which is consistent with the harder momentum distribution of the valence quarks inside the pion as expected from counting rules.[28]

VI) COMPARISON OF $\bar{p}$ DATA TO THEORETICAL PREDICTIONS

In the leading log approximation of QCD, the Drell-Yan cross section for hadronic production of dimuons integrated over p_T is given by (1) where the $q(x,Q^2)$'s are the quark structure functions of the beam and target particles. The structure functions needed in this equation should be identical to those measured in DIS with Q^2 identified as M^2. Figures 10(a) and 10(b) show the differential cross sections $d\sigma/dx_F$ (all p_T and $4<M<9$ GeV/c^2) and $d\sigma/dM$ (all p_T and $x_F>0$) for our $\bar{p}$ data. The solid curves are the predictions of (1) (after the appropriate integrations) obtained using structure functions from the QCD fit of Duke and Owens (DO)[29] with $\Lambda = 0.2$ GeV (set 1) to neutrino, muon, and electron DIS data. The predictions have been multiplied by a factor of K=2.41 to equal the measured total cross section. The valence-valence, valence-sea, sea-valence, and sea-sea components of the predictions are shown separately in Figures 10(a) and 10(b). The valence-valence interaction accounts for 87% of the $\bar{p}$ produced cross section.

Figure 11 shows $d\sigma/dx_F$ and the first order QCD prediction of Kubar et al.[7] The curve was calculated using $\Lambda = 0.2$ GeV and the structure functions of DO. It was multiplied by a factor of 1.39 to normalize to the measured total cross section. Also shown in the figure is the result of (1) multiplied by the same factor. The shapes of the leading log and first order calculations are almost identical and both are in good agreement with the data. Values of the ratio of the first order to leading log predictions are given as a function of x_F and M in Table V. It can be seen that this ratio is nearly constant over the kinematic range covered.

The ultimate accuracy of these comparisons is limited by several factors: 1) the statistical and systematic errors of our measurement; 2) the uncertainty in the A dependence correction due to the error in the measured dimuon production A dependence and the related EMC effect measured in DIS data; 3) systematic differences among DIS experiments using the same target; and 4) the uncertainty in the value of Λ extracted from the fits of DO when used for first order QCD calculations. The statistical and systematic errors in our measurement and the uncertainty in the A-dependence correction have already been described. We now consider the other two factors in more detail.

The DO structure functions[29] were derived from a simultaneous fit to data obtained with several different beams and targets. Appropriate (electromagnetic or weak) forms of $\int F_2(x)dx$ for the various data sets were compared in regions of Q^2 overlap, and all data were renormalized to agree with the μ-H_2 measurement of the EMC group. Table VI lists the renormalization factors for data used in the structure function fits and for other data found in the literature.[30,31,32] There are systematic differences of roughly $\pm 5\%$ about the μ-H_2 data of the EMC group which clearly cannot be attributed to an A-dependence or EMC effect. An error of 5% in the normalization of the derived quark structure functions propagates to become a 10% uncertainty in the Drell-Yan model predictions.

The first order QCD calculation is also sensitive to the value chosen for Λ. Duke and Owens find a correlation between the value of Λ and the "hardness" of the gluon distribution used in their fit. They state that the DIS data alone cannot distinguish between $\Lambda = 0.2$ GeV with a soft gluon distribution (set 1) and $\Lambda = 0.4$ GeV with a hard gluon distribution (set 2). However, they note that the structure functions obtained using a soft gluon distribution and Λ=0.2 GeV are in better agreement with another recent fit to DIS data[33], and, when used in a simple hadro-production model better predict the $pp\to\psi X$ cross section. Therefore, we have used the Λ = 0.2 GeV soft gluon fits in our predictions and, specifically, Λ = 0.2 GeV in the calculation of α_s for the first order prediction. Using Λ = 0.4 GeV increases the first order prediction by 13%.

To summarize, the normalization uncertainties that arise in the comparison of our data to the calculations are due to the statistical error (±5%) and systematic error (±8%) of our measurement, the uncertainty in the A dependence correction (±11%), the DIS normalization uncertainty (±10%) and, in the case of the first order prediction, the uncertainty in the value of Λ (±13%). Combining these errors in quadrature, we find that the leading log prediction must be scaled by a factor K = 2.41±0.42 and the first order prediction by a factor of 1.39±0.30 to equal the measured total cross section for x_F>0 and 4<M<9 GeV/c^2. The leading log prediction is clearly too small and the first order prediction is barely consistent with the measured cross section. The data can accommodate significant contributions from higher order corrections.

A theoretically predicted K-factor can be defined as the ratio of a higher order cross section to the leading log value. For the first order in the $\bar{p}N$ interaction at 125 GeV/c, $K[O(\alpha_s)]$=1.74 if Λ=0.2GeV and $K[O(\alpha_s)]$=1.98 if Λ=0.4GeV. The major contribution to $K[O(\alpha_s)]$ is the so called π^2 term which arises from gluon exchange at the $q\bar{q}$ vertex. The most singular part of this Drell-Yan vertex correction may be calculated to all orders in α_s, giving the following formula for an improved K factor[34]:

$$K(\text{vertex,all orders}) = e^{[(\alpha_s/2\pi)c_F\pi^2]}\,\{K[O(\alpha_s)]-(\alpha_s/2\pi)c_F\pi^2\},$$

where $c_F = 4/3$. Since the vertex correction dominates the first order K-factor, it has been argued[35,36] that K(vertex,all orders) may be a good approximation to the QCD prediction to all orders. For 125 GeV/c $\bar{p}N$ data K(vertex,all orders)=2.10 if Λ=0.2GeV and K(vertex,all orders)=2.58 if Λ=0.4GeV, both of which are in better agreement with the measured value of 2.41 than the first order estimate.

There may be a contribution to the dimuon cross section above M=4 GeV/c^2 from charm or beauty decays. The best evidence against a large contribution to valence-valence dominated processes such as π^-N and $\bar{p}N$ is the experimental observation[3] that the ratio π^-N/π^+N approaches 1/4 as expected for an electromagnetic process such as that of Drell-Yan instead of 1, which would be expected if the dimuons were the decay products of strongly produced $D\bar{D}$ or $B\bar{B}$ pairs. In addition, the polar decay angle distribution for the π^- is in good agreement with the Drell-Yan prediction of $1 + \cos^2\theta$ as observed here and elsewhere.[3] Since the parton structure functions are known independently of the dimuon cross section in the case of $\bar{p}N$ interactions, it is possible to compare the predictions of a reasonable charm production model to the measured cross section. Unfortunately, current experimental data on open charm production are as yet unable to distinguish between a wide class of models which include traditional light quark or gluon fusion, charm excitation, and intrinsic charm content. However, the invariant mass dependence of dimuons from charm or beauty decays will probably be very different from that predicted by the Drell-Yan model. For example, Fisher and Geist[37] have shown that for light quark and gluon fusion the dimuon mass spectrum falls much faster than that of the Drell-Yan model for pp collisions. Using our $\bar{p}$ data we have calculated separate K-factors for two mass bins, $4<M<5$GeV/c^2 and $5<M<9$GeV/c^2, and find

$K=2.35\pm0.14$ and 2.51 ± 0.25 respectively, where the errors are statistical, indicating no strong variation with mass.

VII) SCALING TESTS OF THE DRELL-YAN MODEL

In the naive quark-parton version of the Drell-Yan model, the cross sections $M^3 d^2\sigma/dMdx_F$ and $s^{3/2} d^2\sigma/dMdx_F$ should scale in terms of both variables τ and x_F. Figure 12 shows the cross section $M^3 d\sigma/dM$ with $x_F>0$ as a function of $\sqrt{\tau}$ for our antiproton data at 125 GeV/c and the data of the NA3 experiment[38] at 150 GeV/c. The two measurements agree within errors and are consistent with the shape predicted by (1).

A more detailed scaling test can be made using data obtained with an incident π^- beam. Figure 13 shows the cross section $s^{3/2} d\sigma/dM$ with $x_F>0$ plotted versus $\sqrt{\tau}$ for our pion data, that of the CIP experiment[39] at 225 GeV/c, and that of the Omega experiment[40] at 39.5 GeV/c. Figure 14 shows the cross section $s d\sigma/dx_F$ in the range $0.27<\tau<0.44$ for our data and that of the CIP experiment. In both cases the data exhibit simple scaling. Note that the differential cross section $d\sigma/dx_F$ for our data at 125 GeV/c is smaller than the CIP data at 225 GeV/c by a factor of 1.8 whereas the cross section $s d\sigma/dx_F$ agrees within 15% over the full range of x_F covered.

VIII) QUARK STRUCTURE FUNCTIONS

In this section we present the extraction of the valence quark structure functions for the $\bar{p}$ and π^- by fitting our data to (1). The statistical significance of the data is inadequate to extract quark structure functions that depend on both x and Q^2 so only the x-dependence is considered. In the case of the antiproton, an estimate of the systematic error this introduces was made by assuming a Q^2-dependence similar to the Q^2-evolved DIS structure functions of DO[29].

For antiprotons incident on a nuclear target, the individual beam and target quark structure functions in (1) may be written in terms of the valence quark and sea quark structure functions of the proton:

$$
\begin{aligned}
\bar{u}^{\bar{p}} &= u_v^p + Sea^p, \\
\bar{d}^{\bar{p}} &= d_v^p + Sea^p, \\
u^N &= (Z/A)\ u_v^p + [1 - (Z/A)]\ d_v^p + Sea^p, \\
d^N &= (Z/A)\ d_v^p + [1 - (Z/A)]\ u_v^p + Sea^p, \text{ and} \\
u^{\bar{p}} &= d^{\bar{p}} = \bar{u}^N = \bar{d}^N = \bar{s}^{\bar{p}} = s^{\bar{p}} = s^N = \bar{s}^N = Sea^p.
\end{aligned} \tag{2}
$$

Similarily, for incident pions the quark structure functions in (1) may be written in terms of valence and sea structure functions:

$$
\begin{aligned}
\bar{u}^{\pi^-} &= d^{\pi^-} = V^\pi + Sea^\pi \text{ and} \\
\bar{d}^\pi &= \bar{s}^{\pi^-} = u^{\pi^-} = Sea^\pi.
\end{aligned} \tag{3}
$$

The parameterizations used in the fits are:

$$
\begin{aligned}
u_v^p(x) &= a_p\ x^{\alpha_p}\ (1-x)^{\beta_p}, \\
d_v^p(x) &= 0.57\ u_v^p(x)\ (1-x), \text{ and}
\end{aligned} \tag{4}
$$

$$V^{\pi}(x) = a_{\pi}\, x^{\alpha_{\pi}}\, (1-x)^{\beta_{\pi}}.$$

The relationship between u_v^p and d_v^p was that observed in deep inelastic neutrino scattering data.[41] The sea distribution of the proton was taken from the DIS analysis of D0, and the sea distribution of the pion from fits to π^- and π^+ data of the NA3 collaboration.[42] Recall that sea quarks contribute to only ~13% of the total cross section for the $\bar{p}N$ data.

The fits cannot distinguish between a constant K-factor multiplying (1) and an increase of a_p and/or a_{π}. In the case of the $\bar{p}$, the K-factor can be constrained to be the value found by comparing the data to the Drell-Yan prediction using DIS structure functions, but this is not possible for the π^- produced data. Fortunately, the normalization of the valence quark structure functions can be constrained by other methods, which we will call the "number sum method" and the "momentum sum method". Independent K-factors can then be extracted from the structure function fits using (1). As before, we define the K-factor as the factor by which the Drell-Yan prediction must be increased to reproduce the experimental cross section for $4<M<9$ GeV/c² and $x_F>0$.

The number sum method (the method normally used in Drell-Yan fits to π^- data) requires the integral of the valence quark distribution functions over all values of x-Bjorken to equal the number of valence quarks in the hadron, that is,

$$\int_0^1 [(u_v^p+d_v^p)/x]\,dx = 3 \quad \text{and} \quad \int_0^1 [2V^{\pi}/x]\,dx = 2. \qquad (5)$$

The major drawback of this method is that the dominant contributions to the integrals come from very small values of x, where the fixed target experiments are not sensitive. Typical dimuon experiments produce data above $x_1 = 0.2$, while measurements of xF_3 in DIS[30,43] as shown in Figure 15 indicate that only ~1/4 of $\int_0^1 [(u_v^p+d_v^p)/x]dx$ lies above $x = 0.2$. The number sum method clearly depends heavily on the extrapolation of the fitted structure function parameterization for $x>0.2$ to very small values of x. The choice of a different functional form to parameterize the structure functions, for example, a sum of terms of the form $x^{\alpha}(1-x)^{\beta}$, could drastically alter the normalization of the calculated Drell-Yan cross section while still integrating over x to give the proper number of valence quarks.

The momentum sum method requires that the integral of the valence quark structure function distributions over all x equals the momentum fraction carried by the valence quarks in the nucleon as measured in DIS at our average value of $Q^2=M^2=25\mathrm{GeV}^2$, and a similar expression for the pion, that is,

$$\int_0^1 (u_v^p+d_v^p)\ dx = 0.34 \quad \text{and} \quad \int_0^1 2V^{\pi}\ dx = 0.34. \tag{6}$$

The first integral in (6) was calculated using the $\Lambda = 0.2$ GeV (set 1) solution of Ref. 29 for the valence quark structure functions of the nucleon. The value of the integral decreases by 3.8% if the $\Lambda = 0.4$ GeV (set 2) solution is used instead. The momentum sum method is certainly justified for the $\bar{p}$ data, but must be considered a plausible assumption for the π^- data. Because the factor of $1/x$ is lost in the integrand as compared to (5), the dominant parts of the integrals are now in the x range covered by the data and the normalization is much less sensitive to any extrapolation of the parameterization to small values of x.

Tables VII(a) and VII(b) give the results of several different fits of our $\bar{p}$ and π^- data to (1). These fits were made using all individual data events by the maximum likelihood technique. All the π^- fits were made by constraining the target quark distributions to be those of DO.[29] The $\bar{p}$ data was treated in this same way and also by fitting both the target and beam quark distributions simultaneously to the same quark structure function parameterizations. For each normalization method and target structure function constraint, the data was fitted both with α as a free parameter and with α=0.5 as expected from Regge theory arguments.[44]

A) <u>DISCUSSION OF THE $\bar{p}$ RESULTS</u>

In fits 1 through 6 of Table VII(a), the beam quark and target quark structure functions were both fit to the same parameterization. Comparison of fit 1 with α=0.5 and fit 2 with α free to vary illustrates the sensitivity of the K-factor to the parameterization when using the number sum method normalization of (5). The K-factors obtained from fits 3 and 4, which use the momentum sum method of (6), are much closer together and in reasonable agreement with the K-factor found by comparing the data to the Drell-Yan prediction using DIS structure functions. The values of the parameters α and β are insensitive within errors to the normalization method used.

For fits 7 to 10 the target structure functions were constrained to be those of DO. Fits 7 and 8 allowed the structure functions to vary as a function of Q^2 and fits 9 and 10 fixed Q^2 to our mean value of 25 GeV^2. From the values of the parameters it can be seen that the fits are insensitive to the Q^2 evolution of the structure functions of the target quarks, which partially justifies the use of Q^2-independent parameterizations.

To illustrate the fits quantitatively and make comparisons with other data, (1) was manipulated to project out beam and target structure functions from the measured cross sections. For antiprotons, the equation can be written as

$$\frac{d^2\sigma}{dx_1\,dx_2} = K\,\frac{4\pi\alpha^2}{81}\,\frac{1}{x_1{}^2 x_2{}^2}\Big\{\ \mathrm{BEAM}(x_1,Q^2)\bullet\mathrm{TARGET}(x_2,Q^2)$$

$$+\ (1-\frac{2Z}{A})\ d_v^p(x_1,Q^2)\bullet[u_v^p(x_2,Q^2)-d_v^p(x_2,Q^2)] \tag{7}$$

$$+\ \mathrm{Sea}^p(x_1,Q^2)\bullet\Big[(1-\frac{3Z}{A})u_v^p(x_2,Q^2)+(4-\frac{3Z}{A})d_v^p(x_2,Q^2)+12\ \mathrm{Sea}^p(x_2,Q^2)\Big]\Big\}$$

where

$$\mathrm{BEAM}(x_1,Q^2) = 4\ u_v^p(x_1,Q^2) + d_v^p(x_1,Q^2)\ \text{and}$$

$$\mathrm{TARGET}(x_2,Q^2) = Z/A\ u_v^p(x_2,Q^2) + (1-Z/A)\ d_v^p(x_2,Q^2) + \mathrm{Sea}^p(x_2,Q^2).$$

Here we have added an explicit K-factor in our notation. As will be demonstrated shortly, the second and third terms on the RHS of (7) contribute very little to the cross section and were calculated using the structure functions of Reference 29. The beam and target structure functions can be calculated as averages over the $Q^2=M^2=sx_1x_2$ range of the data as follows:

$$\mathrm{BEAM}(x_1)=\int\mathrm{BEAM}(x_1,Q^2)\mathrm{TARGET}(x_2,Q^2)(1/x_2^2)dx_2 \Big/ \int\mathrm{TARGET}(x_2,Q^2)(1/x_2^2)dx_2,\ \text{and} \tag{8.1}$$

$$\mathrm{TARGET}(x_2)=\int\mathrm{BEAM}(x_1,Q^2)\mathrm{TARGET}(x_2,Q^2)(1/x_1^2)dx_1 \Big/ \int\mathrm{BEAM}(x_1,Q^2)(1/x_1^2)dx_1. \tag{8.2}$$

Figure 16 shows a plot of the values of $K\bullet\mathrm{BEAM}(x_1)$ which were found from (7) and (8.1) using our measured cross sections $d^2\sigma/dx_1dx_2$ and the D0 structure functions to calculate both $\mathrm{TARGET}(x_2,Q^2)$ and the small terms on the RHS of (7). The curves in the figure are the predictions using structure functions from fits 1 and 2 in Table VII(a) and from DO. The fits with α=0.5 and α free to vary describe the data well for x_1>0.2 but give much different K-factors. Recall that the fits ignored the Q^2-dependence of the quark structure functions. The predictions of K•BEAM(x_1) using DIS structure functions with Q^2 evolution and with Q^2 fixed are almost identical and in good agreement with the data, indicating that the fits are good measurements of the $\bar{p}$ quark structure function at $Q^2=M^2=25$ GeV^2. Figure 17 again shows the values of K•BEAM(x_1) for our experiment and the values for the $\bar{p}$ data of the NA3 collaboration at 150 GeV/c.[38] There is excellent agreement between the two experiments.

Figure 18 shows the projected beam structure function and the predictions using the Duke and Owens structure functions both with and without considering the second and third terms on the RHS of (7). It is evident that these terms make only a small contribution to the predicted value.

Figure 19 shows a projection of K•TARGET(x_2) using (7) and (8.2). The DO structure functions were again used to calculate BEAM(x_1,Q^2) and the small terms on the RHS of (7). This projection is also consistent with the prediction based on DIS data although the range of x_2 is limited.

B) <u>DISCUSSION OF THE π^- RESULTS</u>

The π^- fits in Table VII(b) were all made with the target quark distributions constrained to be those of Duke and Owens. The fits using the number sum method of (5) yield K=2.43 for α=0.5 and K=2.68 for α free to vary. The K-factors obtained from the momentum sum method fits are again almost equal with K=2.55 for α=0.5 and K=2.57 for α free to vary. We believe that the momentum sum method gives a good estimate of the K-factor with the assumption that the valence quarks in the pion carry the same fraction of the hadron momentum as the valence quarks in the nucleon. Note that the K-factor values obtained are very similar to the value of K=2.41 for the $\bar{p}$ produced data.

To project out the beam and target quark structure functions for the π^- data, (1) may be rewritten as

$$\frac{d^2\sigma}{dx_1\,dx_2} = K\,\frac{4\pi\alpha^2}{81}\,\frac{1}{x_1{}^2 x_2{}^2}\,\{V^\pi(x_1,Q^2)\cdot \mathrm{TARGET}(x_2,Q^2)$$

$$+\ \mathrm{Sea}^\pi(x_1,Q^2)\Big[\ (1+\frac{3Z}{A})u_v^p(x_2,Q^2)+(4-\frac{3Z}{A})d_v^p(x_2,Q^2)+11\ \mathrm{Sea}^\pi(x_2,Q^2)\Big]\Big\}, \tag{9}$$

where $\mathrm{TARGET}(x_2,Q^2) = \frac{4Z}{A}\ u_v^p(x_2,Q^2)+4(1-Z/A)d_v^p(x_2,Q^2)+5\ \mathrm{Sea}^p(x_2,Q^2)$.

Figure 20 shows the values of $K\cdot V^\pi(x_1)$ which were projected by using in (9) the measured cross sections for $d^2\sigma/dx_1dx_2$, the results of Duke and Owens for the nucleon quark structure functions, and $\mathrm{Sea}^\pi(x)=0.292(1-x)^{8\cdot 2}$ as measured by the NA3 collaboration[42]. The Q^2 averaging was handled as in the $\bar{p}$ case by using (8.1) and (8.2). The curve in the figure represents the predictions of both fit 11 with α=0.5 and fit 12 with α free to vary. Although the predictions for $x_1>0.2$ are identical, the K-factors differ (2.43 compared to 2.68), which again indicates the sensitivity of the K-factors obtained to the low x behavior of the parameterization when using the number sum method of normalization.

Figure 21 shows the projection of the beam structure function using the parameters of fit 12 and the same projection neglecting the second term on the RHS of (9). The effect of the second term is seen to be small, indicating that our results are insensitive to the sea quark distribution in the pion.

Figure 22 shows the target structure function projection obtained from (9) and the prediction of D0 using DIS data. There is good agreement over the complete range of x_2 covered. Figure 23 shows the values of the beam structure function $K \bullet V^{\pi}(x_1)$ for our experiment at 125 GeV/c, the NA3 experiment at 150 GeV/c[42], the CIP experiment at 225 GeV/c[45], and the Goliath experiment at 150 GeV/c.[46] The CIP data was multiplied by the ratio of $A^{1.12}/A^{1.0}$ so that the assumed A-dependence is consistent with the other experiments. There is good agreement between all the data for values of x_1 approaching unity.

C) EFFECT OF THE FIRST ORDER CORRECTION

In Table V we presented calculated values of $K[O(\alpha_s)]$ for the $\bar{p}W$ reaction as a function of x_F and M. Similar results were also obtained for the π^- reaction. It can be seen that the first order correction has little variation over the kinematic range accessible to fixed target experiments and will have a negligible effect on the variation with x of the quark structure functions obtained from the present data.

IX) ANGULAR DISTRIBUTIONS

The angular distributions as functions of cos θ and ϕ for the $\bar{p}$ and π^- data are shown in Figures 24(a) and 24(b). Here θ and ϕ are the polar and azimuthal angles of the positive muon with respect to the beam direction in the dimuon rest frame. Superimposed on the cosθ distributions is the simple Drell-Yan model prediction of $1 + \cos^2\theta$. The data is consistent with the prediction except near cosθ = -1 where there are two experimental problems. First, the statistical accuracy of the data (especially the $\bar{p}$ data) is limited as $|\cos\theta| \to 1$ because the acceptance of the spectrometer falls to very low values (see Figure 8). Second, the background due to accidental coincidences between high momentum negative muons in the beam halo and low momentum muons due to hadron decay occurs near cosθ = -1 and gives rise to large fluctuations in the like-sign event background subtraction.

From Table II(a), it can be seen that the multidimensional fit with the parameter λ (in $1+\lambda\cos^2\theta$) free to vary gave $\lambda = 1.1 \pm 0.3$ for the π^- data and $\lambda = 0.3 \pm 0.4$ for the $\bar{p}$ data. Due to the limited acceptance and large background near cosθ = -1, we do not consider the $\bar{p}$ result to be in disagreement with the Drell-Yan model. In fact, for cosθ > -0.5 where there are no accidental background problems, both the $\bar{p}$ and π^- data closely follow the $1 + \cos^2\theta$ prediction. The QCD corrections to the angular distributions[47] are too small to be meaningfully tested by this experiment. The cross sections presented here were therefore calculated assuming $\lambda = 1$, and the only significant consequence of allowing λ to vary is to lower the absolute $\bar{p}$ cross section by 11%. The shapes of the differential cross sections are unaffected.

X) COMPARISON OF THE TRANSVERSE MOMENTUM DISTRIBUTIONS WITH QCD

Many authors[9,48,49] have argued that there are contributions to the dimuon's transverse momentum from the following sources: 1) the intrinsic transverse momentum of the quarks inside the hadron; 2) the hard scattering first order annihilation and Compton graphs [see Figures 1(c) and 1(d)] which are important for values of p_T near or in excess of the invariant mass; and 3) the emission of soft gluons for smaller values of p_T. Perturbative QCD cannot predict the contribution from the intrinsic transverse momentum of the quarks, so it must be extracted from data. In this paper, the contributions of the first order annihilation and Compton graphs were calculated from Kubar et al.[7] and the soft gluon emission predictions followed the treatment of Chiapetta and Greco[9], who applied the leading order and next to leading order calculations of Kodaira and Trentadue[49] to compare with previously published dimuon data. The soft gluon emission contribution to the cross section may be written ,following Ref. 9, as

$$\frac{d^3\sigma}{dM dx_F dp_T^2} = \frac{8\pi\alpha^2}{9M^3} \frac{(1-\tau)}{[x_F^2 (1-\tau)^2 + 4\tau]^{1/2}} \int b \; J_0(b\; p_T) \; \exp[S(b,M)] \; db$$
$$\bullet \sum_{q=u,d,s} e_q^2 \, [\bar{q}^B(x_1, Q^2) \bullet q^T(x_2, Q^2) + q^B(x_1, Q^2) \bullet \bar{q}^T(x_2, Q^2)], \qquad (10)$$

where

$$S(b,M) = -(2c_F/\pi) \int_{1/b}^{M} (dq_T/q_T) \; \{\ln(M^2/q_T^2) \; \alpha(q_T) \; [1+\kappa \; \alpha(q_T)/2\pi]$$
$$+ 2\ln(e^{\gamma_E}/2) \; \alpha(1/b) - (3/2) \; \alpha(q_T)\} \qquad (11)$$

with $\kappa = 3(67/18-\pi^2/6)-N_F(10/18)$, $\gamma_E = 0.5772$ (Euler's constant), $N_F = 4$ (the number of active quark flavors), $c_F = 4/3$, and

$$\alpha(q)/\pi = [12/(33-2N_F)]\ [1/\ln(q^2/\Lambda^2)] - 72\ [(153-19N_F)/(33-2N_F)^3]\ \{\ln[\ln(q^2/\Lambda^2)]/\ln^2(q^2/\Lambda^2)\}. \quad (12)$$

Equation (11) is only valid in the perturbative region where $b \ll 1/\Lambda$ and non-perturbative effects are parameterized by a regularization of $\alpha(q)$, which is accomplished by the substitution of $q^2+q_0^2$ for q^2 in (12). The value of q_0 used in this analysis was 1.0 GeV. The intrinsic transverse momentum was introduced by inserting an additional factor of $\exp(-b^2\langle p_T^2\rangle_{Int}/4)$ into the integrand of (10).

The QCD calculations were made using the DIS structure functions of DO[29] for the nucleon and the structure functions of Owens and Reya[50] for the π^-. Some double counting occurred by directly summing the soft gluon and annihilation contributions, but since the latter is small the results would not be significantly altered by a more complete treatment.

Figures 25(a) - 25(d) show the differential cross sections $d\sigma/dp_T^2$ with $4<M<9$ GeV/c^2 and $x_F>0$ for our $\bar{p}$ and π^- data. We find average p_T^2 values of 1.09 ± 0.04 (GeV/c)^2 for the $\bar{p}$ data and 1.23 ± 0.03 (GeV/c)^2 for the π^- data. The soft gluon emission and intrinsic quark transverse momentum contributions to $d\sigma/dp_T^2$ for Λ = 0.2GeV and $\langle p_T^2\rangle_{Int}$ = 0.3, 0.4, 0.5, 0.6, and 0.7(GeV/c)^2 are shown in Figures 25(a) and 25(b). The predictions for Λ = 0.4GeV and $\langle p_T^2\rangle_{Int}$ = 0.5(GeV/c)^2 are shown in Figures 25(c) and 25(d). In all cases the predictions were normalized to the integrated cross section, so only shape comparisons of theory to data are meaningful. Note that smaller values of $\langle p_T^2\rangle_{Int}$ are required in order to fit the data as Λ increases. Without invoking the first order annihilation and Compton diagrams, the p_T^2 dependence of the data is described well out to 5 (GeV/c)^2.

Comparing the $\langle p_T^2 \rangle$ of our total data sample with $4<M<9\mathrm{GeV}/c^2$ and $x_F>0$ to QCD predictions with $\Lambda=0.2\mathrm{GeV}$ which include contributions from both soft-gluon and hard processes gives $\langle p_T^2 \rangle_{Int}=0.4(\mathrm{GeV}/c)^2$ for the $\bar{p}$ data and $0.3(\mathrm{GeV}/c)^2$ for the π^- data. Slightly negative $\langle p_T^2 \rangle_{Int}$ values are actually required for predictions with $\Lambda = 0.4\mathrm{GeV}$.

The QCD predictions of $\langle p_T^2 \rangle$ as functions of both M and x_F are shown with the data in Figures 26 and 27. In order to limit computer time, the predictions versus M were made at the average x_F of the data and the predictions versus x_F were calculated at the average M^2. The figures show that the hard contribution is much smaller than the soft gluon contribution in this region. The rise in $\langle p_T^2 \rangle$ with increasing values of M observed in other data and predicted at higher energies[9] is not pronounced at 125 GeV/c. The predictions agree fairly well with the data except in the highest mass bins of the pion sample.

XI) SUMMARY AND CONCLUSIONS

We have studied the production of muon pairs with invariant mass between 4 and 9 GeV/c^2 in $\bar{p}N$ and $\pi^- N$ interactions at an incident momentum of 125 GeV/c using a tungsten target. A special tertiary beam enriched to contain 18% antiprotons allowed us to study the antiproton induced reaction with higher statistics and smaller systematic errors than was possible in previous experiments. Differential cross sections as functions of the dimuon invariant mass, Feynman-x, transverse momentum, and the decay angles of the dimuon were obtained. The total cross sections, p_T distributions, and invariant mass distributions for both the $\bar{p}$ and π^- produced data are remarkably similar. However, the x_F distributions are different reflecting the differences in the quark structure functions of the two beam particles.

The data have been compared to the QCD improved Drell-Yan model and to calculations including higher order QCD corrections. The $\bar{p}$ data is particularly valuable because dimuon production is dominated by the valence-valence interaction and the structure functions that must be used have been measured in deep inelastic scattering. Most of the features of the data are consistent with simple Drell-Yan model calculations except that these must be multiplied by K-factors to reproduce the absolute values of the measured cross sections. For the $\bar{p}$ data the value of K obtained was 2.41 ± 0.42 and for the π^- data the best value of K was 2.57, but relied on constraining the normalization of the pion valence quark distribution by the "momentum sum method". Various scaling distributions used to compare our results with other data, and the dimuon decay angle distributions are also consistent with a simple Drell-Yan model. The net effect of higher order QCD calculations is to leave the various distributions substantially the same but to require progressively lower values of the K-factors needed to reproduce the data as the calculations are made more sophisticated.

We have extracted structure functions for the valence quarks in the $\bar{p}$ and π^- which are valid for $Q^2=M^2=25$ GeV^2 and for $x > 0.2$. The results are in good agreement with dimuon data at other energies and with the nucleon quark structure functions obtained from DIS data.

The transverse momentum distributions have been compared to QCD calculations including soft gluon emission and the hard scattering first order annihilation and Compton scattering graphs. From the comparisons using $\Lambda = 0.2$ GeV we obtained average values of the squares of the intrinsic transverse momenta of the quarks inside the respective hadrons of $0.4(\mathrm{GeV/c})^2$ for the $\bar{p}$ and $0.3(\mathrm{GeV/c})^2$ for the π^-. For both the $\bar{p}$ and π^- data, the model gives a good description of the differential cross section as a function of p_T^2 and the dependence of $\langle p_T^2 \rangle$ on M and x_F. The p_T^2 dependence of the data is described well out to $5(\mathrm{GeV/c})^2$ by the soft gluon and intrinsic p_T^2 contributions without invoking the first order annihilation and Compton diagrams.

This work was performed at Fermi National Accelerator Laboratory and supported by the U.S. Department of Energy, the North Atlantic Treaty Organization Scientific Affairs Division, the International Programs and High Energy Physics Divisions of the National Science Foundation, the Natural Sciences and Engineering Research Council of Canada, the Quebec Department of Education, and the Hellenic Science and Technology Agency.

Authors Footnotes

a. Present address: University of Colorado, Boulder, Colorado.

b. Present address: Prairie View A&M University, Prairie View, Texas.

c. Permanent address: Tata Institute, Bombay, India.

d. Present address: Fermilab, Batavia, Illinois.

e. Present address: Cornell University, Ithaca, New York.

f. Present address: University of Chicago, Chicago, Illinois.

g. Present address: Shell Oil, Houston, Texas.

References

1. S. D. Drell and T. M. Yan, Phys. Rev. Lett. 25 (1970) 316.
2. I. R. Kenyon, Rep. Prog. Phys. 45 (1982) 1261.
3. E. Berger et al., Proceedings of the Drell-Yan Workshop at Fermilab (1982).
4. E. Anassontzis et al., Phys. Rev. Lett. 54 (1985) 2572.
5. H. Politzer, Nucl. Phys. B129 (1977) 301.
6. W. Lindsay et al., Phys. Lett. 117B (1982) 105.
7. J. Kubar et al., Nucl. Phys. B175 (1980) 251.
8. P. K. Malhotra, Proceedings of the Drell-Yan Workshop at Fermilab (1982) 217; B. Cox and P. K. Mulhotra, Phys. Rev. D29 (1984) 63.
9. P. Chiappetta and M. Greco, Nucl. Phys. B221 (1983) 269.
10. E. Anassontzis et al., Nucl. Instr. and Meth. A242 (1986) 215.
11. H. Areti et al., Nucl. Instr. and Meth. 212 (1983) 135.
12. J. Branson et al., Phys. Rev. Lett. 38 (1977) 1334 and references therin.
13. C. Richard-Serre, CERN Report 71-18 (1971).
14. C. Serre, CERN Report 67-5 (1967).
15. P. M. Joseph, Nucl. Instr. and Meth. 75 (1969) 13.
16. G. Koizumi, Fermilab TM-786 (1978).
17. W. Schappert, Ph.D. Thesis, McGill University, Montreal (1984).
18. A. Van Ginneken, Fermilab FN-272 (1975).
19. L. Lyons, Prog. Part. and Nucl. Phys. 7 (1981) 169.
20. For example see R. Roy and B. Nigam, Nuclear Physics , Wiley, N. Y., N. Y. for a discussion of the Fermi Gas model.
21. E. Moniz et al., Phys. Rev. Lett. 26 (1971) 445.

22. A. Bodek and J. Ritchie, Phys. Rev. D23 (1980) 1070.

23. W. Eadie et al., Statistical Methods in Experimental Physics , North Holland, Amsterdam (1971).

24. K. Gottfreid and J. D. Jackson, Nuovo Cimento 33 (1964) 309.

25. A. S. Carroll et al., Phys. Lett. 80B (1979) 319.

26. G. Farrar, Phys. Lett. 56B (1975) 185.

27. P. Bordalo et al., Phys. Lett. 193B (1987) 368.

28. S. Brodsky and G. Farrar, Phys. Rev. D11 (1975) 1309 and S. Brodsky and G. Farrar, Phys. Rev. Lett. 31 (1973) 1153.

29. D. Duke and J. Owens, Phys. Rev. D30 (1984) 49.

30. R. E. Blair et al., "Proceedings of Novel Results in Particle Physics", Nashville (1982) 250.

31. A. R. Clark et al., Phys. Rev. Lett. 51 (1983) 1826.

32. W. Krasny, Proceedings of the EPS International Conference on High Energy Physics, Bari, Italy (1985).

33. H. Abramowicz et al., Z. Phys. C12 (1982) 289.

34. W. J. Sterling, Proceedings of the Drell-Yan Workshop at Fermilab (1982) 131.

35. G. Parisi, Phys. Lett. 90B (1980) 295.

36. G. Curci and M. Greco, Phys. Lett. 92B (1980) 175.

37. H. G. Fischer and W. M. Geist, Z. Phys. C19 (1983) 159.

38. J. Badier et al., Phys. Lett. 96B (1980) 422.

39. C. Newman, Ph.D. Thesis, University of Chicago, Chicago (1979).

40. M. J. Corden et al., Phys. Lett. 96B (1980) 411.

41. F. Eisele, Proc. of the 21st Int. Conf. on High Energy Phys., Paris, J. Physique 43, Supp. C-3 (1982).

42. J. Badier et al., Z. Phys. C18 (1983) 281.

43. J. G. H. de Groot et al., Z. Phys. C1 (1979) 143.

44. G. Farrar, Nucl. Phys. B77 (1974) 429.

45. G. E. Hogan et al.,Phys. Rev. Lett. 42 (1979) 948.

46. R. Barate et al., Phys. Rev. Lett. 43 (1979) 1541.

47. John C. Collins, Phys. Rev. Lett. 42 (1979) 291.

48. J. C. Collins et al., Nucl. Phys. B250 (1985) 199.

49. J. Kodaira and L. Trentadue, Phys. Lett. 112B (1982) 66.

50. J. F. Owens, Phys. Rev. D30 (1984) 943.

Table I -- Data From Tungsten Targets

For the tungsten targets used in E537, the table gives the number absorption lengths, the integrated incident beam, the number of recorded events with $4<M<9 GeV/c^2$, and the reinteraction correction for the (a) $\bar{p}$ and (b) π^- beam components. Note that the second target listed was actually two equal segments separated sufficiently in z so that data from the upstream target could be isolated and used in the ψ reinteraction measurement (see figure 6).

Target Length (cm)	No. of Absorption Lengths	Integrated Beam ($x10^{-11}$)	Events $4<M<9 GeV/c^2$	Reinteraction Correction Factor
		(a) $\bar{p}$		
4.087	0.416	0.1536	14	0.984±.009
2x4.905	0.998	0.7792	106	0.966±.019
14.710	1.50	1.415	267	0.954±.022
Total	--	2.348	387	--
		(b) π^-		
4.087	0.343	0.7060	54	0.987±.007
2x4.905	0.823	2.014	367	0.971±.016
14.710	1.234	3.232	680	0.960±.022
Total	--	5.952	1101	--

Table II -- Kinematic Distribution Parameters

The fits to the data assuming that the $\cos(\theta)$ distribution behaves as (a) $1 + \lambda\cos^2(\theta)$ with λ free and (b) $1 + \cos^2(\theta)$. The acceptance, A, for each of the fits, and the gradient of the acceptance at the minimum of the negative log-likelihood function are also given.

Antiproton	(a) λ Free						
Parameter	Value	Error	Correlation				Grad(A)
α_M	1.331	0.069					1.498E-3
x_{FO}	0.0	Fixed					
σ_x	0.608	0.020	0.021				1.542E-1
p_{TO}	1.107	0.028	0.022	0.034			-5.025E-3
λ	0.279	0.357	-0.074	-0.115	-0.217		-4.230E-2
A	0.237	0.022					
Pion							
α_M	1.116	0.036					-1.853E-2
x_{FO}	-0.032	0.080	-0.018				3.121E-1
σ_x	1.034	0.075	0.065	-0.929			7.571E-3
p_{TO}	1.158	0.018	0.023	0.019	-0.003		-3.114E-3
λ	1.130	0.285	-0.107	-0.120	0.058	-0.184	-2.647E-2
A	0.224	0.011					

Antiproton	(b) λ Fixed to 1					
Parameter	Value	Error	Correlation			Grad(A)
α_M	1.322	0.069				2.349E-3
x_{FO}	0.0	Fixed				
σ_x	0.604	0.019	0.014			1.433E-1
p_{TO}	1.097	0.027	0.003	0.013		2.897E-3
A	0.212	0.004				
Pion						
α_M	1.118	0.037				-2.150E-3
x_{FO}	-0.027	0.078	-0.031			3.130E-2
σ_x	1.032	0.074	0.072	-0.930		6.908E-3
p_{TO}	1.160	0.017	0.003	-0.004	0.008	-4.192E-3
A	0.227	0.003				

Table III - Differential Cross Sections

Double differential dimuon cross sections in (M, x_F), (M, p_T^2) and (x_F, p_T^2) for the $\bar{p}N$ and π^-N data at 125 GeV/c. The entries were extracted from data from tungsten targets using an assumed dependence on the atomic mass of the target of A^1. The cross sections are in units of nb/nucleon/variable-unit. Mass is in units of GeV/c^2 and p_T^2 is in units of (GeV/c)^2. The statistical uncertainty in each value is listed immediately below the cross section.

Table III - $\bar{p}$

x_F\Mass	4.0 - 4.5	4.5 - 5.0	5.0 - 5.5	5.5 - 6.0	6.0 - 6.5	6.5 - 7.0	7.0 - 7.5	7.5 - 8.0	8.0 - 8.5	8.5 - 9.0
-.1 - .0	0.331×10^{0} 0.792×10^{-1}	0.194×10^{0} 0.594×10^{-1}	0.917×10^{-1} 0.379×10^{-1}	0.593×10^{-1} 0.301×10^{-1}	0.000×10^{0} 0.169×10^{-1}	0.000×10^{0} 0.157×10^{-1}	0.000×10^{0} 0.145×10^{-1}	0.000×10^{0} 0.978×10^{-2}	0.000×10^{0} 0.143×10^{-1}	0.000×10^{0} 0.122×10^{-1}
.0 - .1	0.271×10^{0} 0.527×10^{-1}	0.145×10^{0} 0.394×10^{-1}	0.655×10^{-1} 0.270×10^{-1}	0.373×10^{-1} 0.189×10^{-1}	0.102×10^{-1} 0.103×10^{-1}	0.102×10^{-1} 0.103×10^{-1}	0.976×10^{-2} 0.995×10^{-2}	0.000×10^{0} 0.949×10^{-2}	0.000×10^{0} 0.154×10^{-1}	0.000×10^{0} 0.872×10^{-2}
.1 - .2	0.237×10^{0} 0.400×10^{-1}	0.779×10^{-1} 0.226×10^{-1}	0.887×10^{-1} 0.250×10^{-1}	0.628×10^{-1} 0.226×10^{-1}	0.650×10^{-2} 0.652×10^{-2}	0.192×10^{-1} 0.138×10^{-1}	0.000×10^{0} 0.674×10^{-2}	0.000×10^{0} 0.813×10^{-2}	0.000×10^{0} 0.934×10^{-2}	0.000×10^{0} 0.156×10^{-1}
.2 - .3	0.234×10^{0} 0.337×10^{-1}	0.110×10^{0} 0.232×10^{-1}	0.837×10^{-1} 0.220×10^{-1}	0.160×10^{-1} 0.935×10^{-2}	0.178×10^{-1} 0.104×10^{-1}	0.000×10^{0} 0.551×10^{-2}	0.778×10^{-2} 0.793×10^{-2}	0.000×10^{0} 0.616×10^{-2}	0.000×10^{0} 0.860×10^{-2}	0.000×10^{0} 0.427×10^{-2}
.3 - .4	0.127×10^{0} 0.241×10^{-1}	0.907×10^{-1} 0.192×10^{-1}	0.343×10^{-1} 0.122×10^{-1}	0.328×10^{-1} 0.126×10^{-1}	0.512×10^{-2} 0.516×10^{-2}	0.121×10^{-1} 0.880×10^{-2}	0.000×10^{0} 0.503×10^{-2}	0.103×10^{-1} 0.111×10^{-1}	0.873×10^{-2} 0.976×10^{-2}	0.000×10^{0} 0.384×10^{-2}
.4 - .5	0.983×10^{-1} 0.199×10^{-1}	0.323×10^{-1} 0.108×10^{-1}	0.273×10^{-1} 0.983×10^{-2}	0.121×10^{-1} 0.708×10^{-2}	0.341×10^{-2} 0.344×10^{-2}	0.390×10^{-2} 0.396×10^{-2}	0.000×10^{0} 0.567×10^{-2}	0.000×10^{0} 0.423×10^{-2}	0.000×10^{0} 0.119×10^{-1}	0.000×10^{0} 0.214×10^{-2}
.5 - .6	0.363×10^{-1} 0.135×10^{-1}	0.689×10^{-2} 0.691×10^{-2}	0.132×10^{-1} 0.602×10^{-2}	0.129×10^{-1} 0.767×10^{-2}	0.831×10^{-2} 0.609×10^{-2}	0.000×10^{0} 0.335×10^{-2}	0.678×10^{-2} 0.555×10^{-2}	0.000×10^{0} 0.688×10^{-2}	0.000×10^{0} 0.804×10^{-2}	0.000×10^{0} 0.831×10^{-2}
.6 - .7	0.271×10^{-1} 0.104×10^{-1}	0.341×10^{-2} 0.342×10^{-2}	0.420×10^{-2} 0.425×10^{-2}	0.545×10^{-2} 0.396×10^{-2}	0.000×10^{0} 0.427×10^{-2}	0.000×10^{0} 0.759×10^{-2}	0.000×10^{0} 0.889×10^{-2}	0.000×10^{0} 0.252×10^{-2}	0.000×10^{0} 0.168×10^{-2}	0.000×10^{0} 0.504×10^{-2}
.7 - .8	0.466×10^{-2} 0.471×10^{-2}	0.000×10^{0} 0.464×10^{-2}	0.240×10^{-2} 0.246×10^{-2}	0.000×10^{0} 0.163×10^{-2}	0.000×10^{0} 0.232×10^{-1}	0.000×10^{0} 0.207×10^{-2}	0.000×10^{0} 0.935×10^{-2}	0.000×10^{0} 0.224×10^{-2}	0.000×10^{0} 0.000×10^{0}	0.000×10^{0} 0.168×10^{-2}
.8 - .9	0.567×10^{-2} 0.597×10^{-2}	0.000×10^{0} 0.248×10^{-1}	0.000×10^{0} 0.267×10^{-2}	0.000×10^{0} 0.528×10^{-2}	0.000×10^{0} 0.393×10^{-2}	0.000×10^{0} 0.452×10^{-2}	0.000×10^{0} 0.168×10^{-2}	0.000×10^{0} 0.000×10^{0}	0.000×10^{0} 0.000×10^{0}	0.000×10^{0} 0.000×10^{0}
.9 - 1.0	0.000×10^{0} 0.155×10^{-1}	0.000×10^{0} 0.904×10^{-2}	0.000×10^{0} 0.368×10^{-2}	0.000×10^{0} 0.136×10^{-3}	0.000×10^{0} 0.000×10^{0}	0.000×10^{0} 0.168×10^{-2}	0.000×10^{0} 0.000×10^{0}	0.000×10^{0} 0.168×10^{-2}	0.000×10^{0} 0.000×10^{0}	0.000×10^{0} 0.168×10^{-2}

Table III - $\bar{p}$

p_T^2\Mass	4.0 - 4.5	4.5 - 5.0	5.0 - 5.5	5.5 - 6.0	6.0 - 6.5	6.5 - 7.0	7.0 - 7.5	7.5 - 8.0	8.0 - 8.5	8.5 - 9.0
.0 - .5	0.729×10^{-1} 0.959×10^{-2}	0.382×10^{-1} 0.683×10^{-2}	0.222×10^{-1} 0.517×10^{-2}	0.177×10^{-1} 0.483×10^{-2}	0.139×10^{-2} 0.139×10^{-2}	0.289×10^{-2} 0.206×10^{-2}	0.000×10^{0} $.139\times10^{-2}$	0.000×10^{0} 0.113×10^{-2}	0.000×10^{0} 0.138×10^{-2}	0.000×10^{0} 0.114×10^{-2}
.5 - 1.0	0.513×10^{-1} 0.793×10^{-2}	0.255×10^{-1} 0.540×10^{-2}	0.216×10^{-1} 0.536×10^{-2}	0.376×10^{-2} 0.219×10^{-2}	0.433×10^{-2} 0.220×10^{-2}	0.216×10^{-2} 0.155×10^{-2}	0.366×10^{-2} 0.269×10^{-2}	0.000×10^{0} 0.209×10^{-2}	0.171×10^{-2} 0.183×10^{-2}	0.000×10^{0} 0.184×10^{-2}
1.0 - 1.5	0.318×10^{-1} 0.597×10^{-2}	0.874×10^{-2} 0.311×10^{-2}	0.898×10^{-2} 0.322×10^{-2}	0.226×10^{-2} 0.161×10^{-2}	0.000×10^{0} 0.142×10^{-2}	0.000×10^{0} 0.124×10^{-2}	0.174×10^{-2} 0.129×10^{-2}	0.240×10^{-2} 0.263×10^{-2}	0.000×10^{0} 0.200×10^{-2}	0.000×10^{0} 0.939×10^{-3}
1.5 - 2.0	0.172×10^{-1} 0.438×10^{-2}	0.904×10^{-2} 0.323×10^{-2}	0.387×10^{-2} 0.196×10^{-2}	0.471×10^{-2} 0.240×10^{-2}	0.000×10^{0} 0.107×10^{-2}	0.000×10^{0} 0.180×10^{-2}	0.000×10^{0} 0.199×10^{-2}	0.000×10^{0} 0.131×10^{-2}	0.000×10^{0} 0.376×10^{-2}	0.000×10^{0} 0.594×10^{-3}
2.0 - 2.5	0.732×10^{-2} 0.279×10^{-2}	0.204×10^{-2} 0.145×10^{-2}	0.314×10^{-2} 0.183×10^{-2}	0.000×10^{0} 0.114×10^{-2}	0.314×10^{-2} 0.189×10^{-2}	0.134×10^{-2} 0.138×10^{-2}	0.000×10^{0} 0.272×10^{-2}	0.000×10^{0} 0.141×10^{-2}	0.000×10^{0} 0.200×10^{-2}	0.000×10^{0} 0.194×10^{-2}
2.5 - 3.0	0.105×10^{-1} 0.323×10^{-2}	0.992×10^{-3} 0.995×10^{-3}	0.220×10^{-2} 0.158×10^{-2}	0.265×10^{-2} 0.158×10^{-2}	0.000×10^{0} 0.100×10^{-2}	0.117×10^{-2} 0.122×10^{-2}	0.000×10^{0} 0.157×10^{-2}	0.000×10^{0} 0.172×10^{-2}	0.000×10^{0} 0.168×10^{-2}	0.000×10^{0} 0.100×10^{-2}
3.0 - 3.5	0.844×10^{-2} 0.326×10^{-2}	0.484×10^{-2} 0.221×10^{-2}	0.130×10^{-2} 0.132×10^{-2}	0.187×10^{-2} 0.192×10^{-2}	0.000×10^{0} 0.158×10^{-2}	0.000×10^{0} 0.201×10^{-2}	0.000×10^{0} 0.583×10^{-3}	0.000×10^{0} 0.299×10^{-2}	0.000×10^{0} 0.300×10^{-2}	0.000×10^{0} 0.165×10^{-2}
3.5 - 4.0	0.330×10^{-2} 0.193×10^{-2}	0.177×10^{-2} 0.126×10^{-2}	0.116×10^{-2} 0.118×10^{-2}	0.000×10^{0} 0.852×10^{-3}	0.000×10^{0} 0.122×10^{-2}	0.000×10^{0} 0.115×10^{-2}	0.000×10^{0} 0.132×10^{-2}	0.000×10^{0} 0.660×10^{-3}	0.000×10^{0} 0.336×10^{-3}	0.000×10^{0} 0.000×10^{0}
4.0 - 4.5	0.104×10^{-2} 0.105×10^{-2}	0.125×10^{-2} 0.126×10^{-2}	0.000×10^{0} 0.715×10^{-3}	0.805×10^{-3} 0.829×10^{-3}	0.580×10^{-3} 0.621×10^{-3}	0.000×10^{0} 0.222×10^{-2}	0.000×10^{0} 0.628×10^{-3}	0.000×10^{0} 0.163×10^{-2}	0.000×10^{0} 0.165×10^{-2}	0.000×10^{0} 0.000×10^{0}
4.5 - 5.0	0.717×10^{-3} 0.722×10^{-3}	0.000×10^{0} 0.886×10^{-3}	0.669×10^{-3} 0.686×10^{-3}	0.788×10^{-3} 0.821×10^{-3}	0.000×10^{0} 0.200×10^{-2}	0.000×10^{0} 0.133×10^{-2}	0.000×10^{0} 0.267×10^{-2}	0.000×10^{0} 0.187×10^{-3}	0.000×10^{0} 0.336×10^{-3}	0.000×10^{0} 0.000×10^{0}
5.0 - 5.5	0.764×10^{-3} 0.771×10^{-3}	0.000×10^{0} 0.717×10^{-3}	0.000×10^{0} 0.102×10^{-2}	0.000×10^{0} 0.201×10^{-2}	0.000×10^{0} 0.105×10^{-2}	0.000×10^{0} 0.430×10^{-2}	0.000×10^{0} 0.198×10^{-2}	0.000×10^{0} 0.336×10^{-3}	0.000×10^{0} 0.000×10^{0}	0.000×10^{0} 0.664×10^{-3}
5.5 - 6.0	0.207×10^{-2} 0.152×10^{-2}	0.000×10^{0} 0.116×10^{-2}	0.000×10^{0} 0.105×10^{-2}	0.000×10^{0} 0.121×10^{-2}	0.000×10^{0} 0.190×10^{-3}	0.000×10^{0} 0.161×10^{-2}	0.000×10^{0} 0.991×10^{-3}	0.000×10^{0} 0.336×10^{-3}	0.000×10^{0} 0.000×10^{0}	0.000×10^{0} 0.000×10^{0}
6.0 - 6.5	0.262×10^{-2} 0.197×10^{-2}	0.000×10^{0} 0.781×10^{-3}	0.000×10^{0} 0.142×10^{-2}	0.000×10^{0} 0.628×10^{-3}	0.000×10^{0} 0.480×10^{-3}	0.000×10^{0} 0.141×10^{-2}	0.000×10^{0} 0.318×10^{-3}	0.000×10^{0} 0.336×10^{-3}	0.000×10^{0} 0.986×10^{-3}	0.000×10^{0} 0.000×10^{0}
6.5 - 7.0	0.000×10^{0} 0.781×10^{-3}	0.000×10^{0} 0.279×10^{-2}	0.000×10^{0} 0.124×10^{-2}	0.000×10^{0} 0.194×10^{-2}	0.000×10^{0} 0.805×10^{-3}	0.000×10^{0} 0.586×10^{-3}	0.000×10^{0} 0.599×10^{-3}	0.000×10^{0} 0.000×10^{0}	0.000×10^{0} 0.000×10^{0}	0.000×10^{0} 0.000×10^{0}
7.0 - 7.5	0.000×10^{0} 0.771×10^{-3}	0.000×10^{0} 0.684×10^{-3}	0.000×10^{0} 0.911×10^{-3}	0.000×10^{0} 0.333×10^{-2}	0.000×10^{0} 0.131×10^{-2}	0.000×10^{0} 0.132×10^{-2}	0.000×10^{0} 0.248×10^{-3}	0.000×10^{0} 0.000×10^{0}	0.000×10^{0} 0.000×10^{0}	0.000×10^{0} 0.000×10^{0}

Table III - $\bar{p}$

$p_T^2 \backslash x_F$	-.10 - .00	.00 - .10	.10 - .20	.20 - .30	.30 - .40	.40 - .50	.50 - .60	.60 - .70	.70 - .80	.80 - .90	.90 - 1.0
.0 - .5	0.222×10^{0} 0.648×10^{-1}	0.210×10^{0} 0.476×10^{-1}	0.152×10^{0} 0.327×10^{-1}	0.210×10^{0} 0.343×10^{-1}	0.973×10^{-1} 0.222×10^{-1}	0.756×10^{-1} 0.176×10^{-1}	0.216×10^{-1} 0.102×10^{-1}	0.131×10^{-1} 0.770×10^{-2}	0.394×10^{-2} 0.399×10^{-2}	0.000×10^{0} 0.581×10^{-2}	0.000×10^{0} 0.478×10^{-2}
.5 - 1.0	0.134×10^{0} 0.480×10^{-1}	0.148×10^{0} 0.401×10^{-1}	0.133×10^{0} 0.318×10^{-1}	0.109×10^{0} 0.242×10^{-1}	0.949×10^{-1} 0.201×10^{-1}	0.283×10^{-1} 0.101×10^{-1}	0.320×10^{-1} 0.129×10^{-1}	0.134×10^{-1} 0.685×10^{-2}	0.000×10^{0} 0.367×10^{-2}	0.925×10^{-2} 0.101×10^{-1}	0.000×10^{0} 0.527×10^{-2}
1.0 - 1.5	0.124×10^{0} 0.449×10^{-1}	0.718×10^{-1} 0.274×10^{-1}	0.769×10^{-1} 0.225×10^{-1}	0.568×10^{-1} 0.166×10^{-1}	0.395×10^{-1} 0.126×10^{-1}	0.286×10^{-1} 0.114×10^{-1}	0.678×10^{-2} 0.483×10^{-2}	0.000×10^{0} 0.400×10^{-2}	0.336×10^{-2} 0.347×10^{-2}	0.000×10^{0} 0.354×10^{-2}	0.000×10^{0} 0.508×10^{-2}
1.5 - 2.0	0.381×10^{-1} 0.272×10^{-1}	0.436×10^{-1} 0.220×10^{-1}	0.320×10^{-1} 0.144×10^{-1}	0.274×10^{-1} 0.113×10^{-1}	0.286×10^{-1} 0.118×10^{-1}	0.205×10^{-1} 0.794×10^{-2}	0.986×10^{-2} 0.580×10^{-2}	0.447×10^{-2} 0.455×10^{-2}	0.000×10^{0} 0.708×10^{-2}	0.000×10^{0} 0.354×10^{-2}	0.000×10^{0} 0.171×10^{-2}
2.0 - 2.5	0.366×10^{-1} 0.262×10^{-1}	0.251×10^{-1} 0.146×10^{-1}	0.231×10^{-1} 0.116×10^{-1}	0.142×10^{-1} 0.826×10^{-2}	0.876×10^{-2} 0.623×10^{-2}	0.724×10^{-2} 0.517×10^{-2}	0.440×10^{-2} 0.445×10^{-2}	0.349×10^{-2} 0.357×10^{-2}	0.000×10^{0} 0.403×10^{-2}	0.000×10^{0} 0.155×10^{-1}	0.000×10^{0} 0.168×10^{-2}
2.5 - 3.0	0.488×10^{-1} 0.289×10^{-1}	0.252×10^{-1} 0.148×10^{-1}	0.135×10^{-1} 0.964×10^{-2}	0.252×10^{-1} 0.105×10^{-1}	0.972×10^{-2} 0.569×10^{-2}	0.129×10^{-1} 0.768×10^{-2}	0.000×10^{0} 0.286×10^{-2}	0.200×10^{-2} 0.205×10^{-2}	0.000×10^{0} 0.354×10^{-2}	0.000×10^{0} 0.683×10^{-2}	0.000×10^{0} 0.000×10^{0}
3.0 - 3.5	0.000×10^{0} 0.206×10^{-1}	0.329×10^{-1} 0.194×10^{-1}	0.150×10^{-1} 0.107×10^{-1}	0.927×10^{-2} 0.662×10^{-2}	0.271×10^{-1} 0.115×10^{-1}	0.391×10^{-2} 0.396×10^{-2}	0.000×10^{0} 0.416×10^{-2}	0.000×10^{0} 0.545×10^{-2}	0.000×10^{0} 0.124×10^{-1}	0.000×10^{0} 0.302×10^{-2}	0.000×10^{0} 0.000×10^{0}
3.5 - 4.0	0.234×10^{-1} 0.170×10^{-1}	0.000×10^{0} 0.115×10^{-1}	0.000×10^{0} 0.643×10^{-2}	0.106×10^{-1} 0.624×10^{-2}	0.370×10^{-2} 0.375×10^{-2}	0.000×10^{0} 0.362×10^{-2}	0.922×10^{-2} 0.704×10^{-2}	0.000×10^{0} 0.176×10^{-2}	0.000×10^{0} 0.370×10^{-2}	0.000×10^{0} 0.400×10^{-2}	0.000×10^{0} 0.168×10^{-2}
4.0 - 4.5	0.000×10^{0} 0.230×10^{-1}	0.000×10^{0} 0.848×10^{-2}	0.124×10^{-1} 0.906×10^{-2}	0.417×10^{-2} 0.422×10^{-2}	0.371×10^{-2} 0.377×10^{-2}	0.000×10^{0} 0.371×10^{-2}	0.000×10^{0} 0.438×10^{-2}	0.000×10^{0} 0.305×10^{-2}	0.000×10^{0} 0.586×10^{-2}	0.000×10^{0} 0.168×10^{-2}	0.000×10^{0} 0.168×10^{-2}
4.5 - 5.0	0.971×10^{-2} 0.997×10^{-2}	0.000×10^{0} 0.745×10^{-2}	0.971×10^{-2} 0.706×10^{-2}	0.000×10^{0} 0.328×10^{-2}	0.000×10^{0} 0.292×10^{-2}	0.000×10^{0} 0.202×10^{-2}	0.000×10^{0} 0.337×10^{-2}	0.578×10^{-2} 0.708×10^{-2}	0.000×10^{0} 0.319×10^{-2}	0.000×10^{0} 0.168×10^{-2}	0.000×10^{0} 0.168×10^{-2}
5.0 - 5.5	0.000×10^{0} 0.155×10^{-1}	0.000×10^{0} 0.752×10^{-2}	0.000×10^{0} 0.359×10^{-2}	0.593×10^{-2} 0.611×10^{-2}	0.000×10^{0} 0.282×10^{-2}	0.000×10^{0} 0.304×10^{-2}	0.000×10^{0} 0.336×10^{-2}	0.000×10^{0} 0.100×10^{-1}	0.000×10^{0} 0.294×10^{-2}	0.000×10^{0} 0.000×10^{0}	0.000×10^{0} 0.000×10^{0}
5.5 - 6.0	0.166×10^{-1} 0.180×10^{-1}	0.000×10^{0} 0.770×10^{-2}	0.586×10^{-2} 0.608×10^{-2}	0.000×10^{0} 0.438×10^{-2}	0.000×10^{0} 0.714×10^{-2}	0.257×10^{-2} 0.275×10^{-2}	0.000×10^{0} 0.501×10^{-2}	0.000×10^{0} 0.974×10^{-3}	0.000×10^{0} 0.168×10^{-2}	0.000×10^{0} 0.000×10^{0}	0.000×10^{0} 0.000×10^{0}
6.0 - 6.5	0.000×10^{0} 0.161×10^{-1}	0.000×10^{0} 0.171×10^{-1}	0.489×10^{-2} 0.505×10^{-2}	0.331×10^{-2} 0.346×10^{-2}	0.000×10^{0} 0.360×10^{-2}	0.000×10^{0} 0.542×10^{-2}	0.000×10^{0} 0.487×10^{-2}	0.000×10^{0} 0.104×10^{-2}	0.000×10^{0} 0.000×10^{0}	0.000×10^{0} 0.000×10^{0}	0.000×10^{0} 0.168×10^{-2}
6.5 - 7.0	0.000×10^{0} 0.972×10^{-2}	0.000×10^{0} 0.717×10^{-2}	0.000×10^{0} 0.138×10^{-1}	0.000×10^{0} 0.340×10^{-2}	0.000×10^{0} 0.242×10^{-2}	0.000×10^{0} 0.657×10^{-2}	0.000×10^{0} 0.336×10^{-2}	0.000×10^{0} 0.145×10^{-2}	0.000×10^{0} 0.319×10^{-2}	0.000×10^{0} 0.000×10^{0}	0.000×10^{0} 0.000×10^{0}
7.0 - 7.5	0.000×10^{0} 0.148×10^{-1}	0.000×10^{0} 0.198×10^{-1}	0.302×10^{-2} 0.320×10^{-2}	0.000×10^{0} 0.109×10^{-1}	0.000×10^{0} 0.325×10^{-2}	0.000×10^{0} 0.127×10^{-2}	0.000×10^{0} 0.502×10^{-2}	0.000×10^{0} 0.478×10^{-2}	0.000×10^{0} 0.168×10^{-2}	0.000×10^{0} 0.168×10^{-2}	0.000×10^{0} 0.000×10^{0}

Table III - π^-

x_F\Mass	4.0 - 4.5	4.5 - 5.0	5.0 - 5.5	5.5 - 6.0	6.0 - 6.5	6.5 - 7.0	7.0 - 7.5	7.5 - 8.0	8.0 - 8.5	8.5 - 9.0
-.1 - .0	0.173×10^{0} 0.352×10^{-1}	0.952×10^{-1} 0.254×10^{-1}	0.158×10^{-1} 0.922×10^{-2}	0.185×10^{-1} 0.945×10^{-2}	0.110×10^{-1} 0.794×10^{-2}	0.000×10^{0} 0.520×10^{-2}	0.873×10^{-2} 0.641×10^{-2}	0.510×10^{-2} 0.527×10^{-2}	0.000×10^{0} 0.679×10^{-2}	0.000×10^{0} 0.178×10^{-1}
.0 - .1	0.146×10^{0} 0.234×10^{-1}	0.638×10^{-1} 0.153×10^{-1}	0.424×10^{-1} 0.130×10^{-1}	0.242×10^{-1} 0.100×10^{-1}	0.100×10^{-1} 0.590×10^{-2}	0.129×10^{-1} 0.768×10^{-2}	0.000×10^{0} 0.308×10^{-2}	0.000×10^{0} 0.418×10^{-2}	0.303×10^{-2} 0.312×10^{-2}	0.000×10^{0} 0.414×10^{-1}
.1 - .2	0.165×10^{0} 0.207×10^{-1}	0.657×10^{-1} 0.124×10^{-1}	0.592×10^{-1} 0.126×10^{-1}	0.226×10^{-1} 0.811×10^{-2}	0.235×10^{-1} 0.854×10^{-2}	0.786×10^{-2} 0.564×10^{-2}	0.967×10^{-2} 0.576×10^{-2}	0.262×10^{-2} 0.266×10^{-2}	0.375×10^{-2} 0.388×10^{-2}	0.208×10^{-2} 0.217×10^{-2}
.2 - .3	0.169×10^{0} 0.178×10^{-1}	0.882×10^{-1} 0.133×10^{-1}	0.422×10^{-1} 0.980×10^{-2}	0.162×10^{-1} 0.582×10^{-2}	0.143×10^{-1} 0.550×10^{-2}	0.113×10^{-1} 0.520×10^{-2}	0.769×10^{-2} 0.456×10^{-2}	0.482×10^{-2} 0.350×10^{-2}	0.260×10^{-2} 0.266×10^{-2}	0.000×10^{0} 0.328×10^{-2}
.3 - .4	0.138×10^{0} 0.150×10^{-1}	0.529×10^{-1} 0.872×10^{-2}	0.327×10^{-1} 0.743×10^{-2}	0.234×10^{-1} 0.615×10^{-2}	0.170×10^{-1} 0.580×10^{-2}	0.374×10^{-2} 0.266×10^{-2}	0.816×10^{-2} 0.419×10^{-2}	0.730×10^{-2} 0.439×10^{-2}	0.000×10^{0} 0.224×10^{-2}	0.202×10^{-2} 0.208×10^{-2}
.4 - .5	0.104×10^{0} 0.132×10^{-1}	0.707×10^{-1} 0.102×10^{-1}	0.374×10^{-1} 0.736×10^{-2}	0.239×10^{-1} 0.610×10^{-2}	0.129×10^{-1} 0.439×10^{-2}	0.638×10^{-2} 0.324×10^{-2}	0.514×10^{-2} 0.304×10^{-2}	0.000×10^{0} 0.169×10^{-2}	0.000×10^{0} 0.148×10^{-2}	0.000×10^{0} 0.212×10^{-2}
.5 - .6	0.941×10^{-1} 0.130×10^{-1}	0.471×10^{-1} 0.860×10^{-2}	0.267×10^{-1} 0.610×10^{-2}	0.167×10^{-1} 0.474×10^{-2}	0.105×10^{-1} 0.381×10^{-2}	0.886×10^{-2} 0.345×10^{-2}	0.113×10^{-1} 0.491×10^{-2}	0.469×10^{-2} 0.282×10^{-2}	0.000×10^{0} 0.191×10^{-2}	0.000×10^{0} 0.959×10^{-3}
.6 - .7	0.703×10^{-1} 0.129×10^{-1}	0.413×10^{-1} 0.878×10^{-2}	0.227×10^{-1} 0.600×10^{-2}	0.156×10^{-1} 0.469×10^{-2}	0.110×10^{-1} 0.449×10^{-2}	0.429×10^{-2} 0.219×10^{-2}	0.000×10^{0} 0.118×10^{-2}	0.511×10^{-2} 0.313×10^{-2}	0.000×10^{0} 0.141×10^{-2}	0.000×10^{0} 0.237×10^{-2}
.7 - .8	0.536×10^{-1} 0.138×10^{-1}	0.237×10^{-1} 0.768×10^{-2}	0.153×10^{-1} 0.591×10^{-2}	0.484×10^{-2} 0.283×10^{-2}	0.486×10^{-2} 0.286×10^{-2}	0.101×10^{-1} 0.436×10^{-2}	0.144×10^{-2} 0.146×10^{-2}	0.184×10^{-2} 0.190×10^{-2}	0.000×10^{0} 0.470×10^{-2}	0.177×10^{-2} 0.194×10^{-2}
.8 - .9	0.200×10^{-1} 0.118×10^{-1}	0.153×10^{-1} 0.784×10^{-2}	0.542×10^{-2} 0.389×10^{-2}	0.524×10^{-2} 0.379×10^{-2}	0.000×10^{0} 0.359×10^{-2}	0.145×10^{-2} 0.147×10^{-2}	0.000×10^{0} 0.176×10^{-2}	0.204×10^{-2} 0.219×10^{-2}	0.321×10^{-2} 0.371×10^{-2}	0.000×10^{0} 0.842×10^{-2}
.9 - 1.0	0.000×10^{0} 0.130×10^{-1}	0.000×10^{0} 0.125×10^{-1}	0.443×10^{-2} 0.468×10^{-2}	0.000×10^{0} 0.487×10^{-2}	0.000×10^{0} 0.308×10^{-2}	0.309×10^{-2} 0.363×10^{-2}	0.000×10^{0} 0.706×10^{-2}	0.000×10^{0} 0.259×10^{-2}	0.000×10^{0} 0.111×10^{-2}	0.000×10^{0} 0.161×10^{-3}

Table III - π^-

p_T^2\Mass	4.0 - 4.5	4.5 - 5.0	5.0 - 5.5	5.5 - 6.0	6.0 - 6.5	6.5 - 7.0	7.0 - 7.5	7.5 - 8.0	8.0 - 8.5	8.5 - 9.0
.0 - .5	0.625×10^{-1} 0.527×10^{-2}	0.351×10^{-1} 0.382×10^{-2}	0.214×10^{-1} 0.300×10^{-2}	0.671×10^{-2} 0.164×10^{-2}	0.675×10^{-2} 0.176×10^{-2}	0.338×10^{-2} 0.121×10^{-2}	0.286×10^{-2} 0.119×10^{-2}	0.300×10^{-2} 0.127×10^{-2}	0.130×10^{-2} 0.776×10^{-3}	0.486×10^{-3} 0.496×10^{-3}
.5 - 1.0	0.436×10^{-1} 0.440×10^{-2}	0.205×10^{-1} 0.287×10^{-2}	0.144×10^{-1} 0.250×10^{-2}	0.756×10^{-2} 0.177×10^{-2}	0.432×10^{-2} 0.132×10^{-2}	0.376×10^{-2} 0.122×10^{-2}	0.123×10^{-2} 0.727×10^{-3}	0.991×10^{-3} 0.714×10^{-3}	0.000×10^{0} 0.560×10^{-3}	0.000×10^{0} 0.785×10^{-3}
1.0 - 1.5	0.317×10^{-1} 0.379×10^{-2}	0.133×10^{-1} 0.230×10^{-2}	0.523×10^{-2} 0.141×10^{-2}	0.465×10^{-2} 0.131×10^{-2}	0.425×10^{-2} 0.138×10^{-2}	0.295×10^{-2} 0.136×10^{-2}	0.179×10^{-2} 0.928×10^{-3}	0.890×10^{-3} 0.647×10^{-3}	0.000×10^{0} 0.716×10^{-3}	0.508×10^{-3} 0.527×10^{-3}
1.5 - 2.0	0.203×10^{-1} 0.299×10^{-2}	0.856×10^{-2} 0.178×10^{-2}	0.417×10^{-2} 0.127×10^{-2}	0.467×10^{-2} 0.128×10^{-2}	0.198×10^{-2} 0.827×10^{-3}	0.159×10^{-2} 0.734×10^{-3}	0.740×10^{-3} 0.534×10^{-3}	0.747×10^{-3} 0.548×10^{-3}	0.396×10^{-3} 0.409×10^{-3}	0.000×10^{0} 0.202×10^{-3}
2.0 - 2.5	0.126×10^{-1} 0.236×10^{-2}	0.489×10^{-2} 0.138×10^{-2}	0.330×10^{-2} 0.118×10^{-2}	0.518×10^{-2} 0.156×10^{-2}	0.132×10^{-2} 0.777×10^{-3}	0.338×10^{-3} 0.341×10^{-3}	0.727×10^{-3} 0.529×10^{-3}	0.000×10^{0} 0.396×10^{-3}	0.000×10^{0} 0.446×10^{-3}	0.362×10^{-3} 0.384×10^{-3}
2.5 - 3.0	0.595×10^{-2} 0.156×10^{-2}	0.368×10^{-2} 0.113×10^{-2}	0.247×10^{-2} 0.102×10^{-2}	0.786×10^{-3} 0.562×10^{-3}	0.430×10^{-3} 0.434×10^{-3}	0.498×10^{-3} 0.509×10^{-3}	0.605×10^{-3} 0.445×10^{-3}	0.549×10^{-3} 0.576×10^{-3}	0.000×10^{0} 0.332×10^{-3}	0.000×10^{0} 0.104×10^{-2}
3.0 - 3.5	0.356×10^{-2} 0.133×10^{-2}	0.199×10^{-2} 0.106×10^{-2}	0.195×10^{-2} 0.816×10^{-3}	0.176×10^{-2} 0.815×10^{-3}	0.000×10^{0} 0.278×10^{-3}	0.988×10^{-3} 0.602×10^{-3}	0.000×10^{0} 0.536×10^{-3}	0.216×10^{-3} 0.225×10^{-3}	0.000×10^{0} 0.718×10^{-3}	0.000×10^{0} 0.432×10^{-3}
3.5 - 4.0	0.328×10^{-2} 0.118×10^{-2}	0.166×10^{-2} 0.894×10^{-3}	0.113×10^{-2} 0.669×10^{-3}	0.000×10^{0} 0.382×10^{-3}	0.152×10^{-2} 0.941×10^{-3}	0.000×10^{0} 0.640×10^{-3}	0.000×10^{0} 0.509×10^{-3}	0.000×10^{0} 0.420×10^{-3}	0.000×10^{0} 0.377×10^{-3}	0.000×10^{0} 0.174×10^{-2}
4.0 - 4.5	0.335×10^{-2} 0.121×10^{-2}	0.123×10^{-2} 0.631×10^{-3}	0.874×10^{-3} 0.516×10^{-3}	0.000×10^{0} 0.428×10^{-3}	0.390×10^{-3} 0.400×10^{-3}	0.337×10^{-3} 0.348×10^{-3}	0.636×10^{-3} 0.697×10^{-3}	0.000×10^{0} 0.426×10^{-3}	0.000×10^{0} 0.165×10^{-3}	0.000×10^{0} 0.377×10^{-3}
4.5 - 5.0	0.234×10^{-2} 0.985×10^{-3}	0.214×10^{-2} 0.100×10^{-2}	0.405×10^{-3} 0.410×10^{-3}	0.000×10^{0} 0.269×10^{-3}	0.278×10^{-3} 0.286×10^{-3}	0.000×10^{0} 0.215×10^{-3}	0.000×10^{0} 0.423×10^{-3}	0.000×10^{0} 0.480×10^{-3}	0.000×10^{0} 0.316×10^{-3}	0.000×10^{0} 0.126×10^{-3}
5.0 - 5.5	0.620×10^{-3} 0.444×10^{-3}	0.315×10^{-3} 0.318×10^{-3}	0.108×10^{-2} 0.660×10^{-3}	0.000×10^{0} 0.310×10^{-3}	0.000×10^{0} 0.253×10^{-3}	0.000×10^{0} 0.322×10^{-3}	0.000×10^{0} 0.253×10^{-3}	0.000×10^{0} 0.488×10^{-3}	0.000×10^{0} 0.377×10^{-3}	0.000×10^{0} 0.539×10^{-3}
5.5 - 6.0	0.100×10^{-2} 0.727×10^{-3}	0.113×10^{-2} 0.690×10^{-3}	0.721×10^{-3} 0.536×10^{-3}	0.000×10^{0} 0.342×10^{-3}	0.779×10^{-3} 0.618×10^{-3}	0.000×10^{0} 0.281×10^{-3}	0.000×10^{0} 0.387×10^{-3}	0.000×10^{0} 0.742×10^{-3}	0.000×10^{0} 0.628×10^{-3}	0.000×10^{0} 0.252×10^{-3}
6.0 - 6.5	0.129×10^{-2} 0.680×10^{-3}	0.702×10^{-3} 0.514×10^{-3}	0.000×10^{0} 0.285×10^{-3}	0.000×10^{0} 0.294×10^{-3}	0.000×10^{0} 0.921×10^{-3}	0.265×10^{-3} 0.307×10^{-3}	0.000×10^{0} 0.153×10^{-3}	0.000×10^{0} 0.457×10^{-3}	0.000×10^{0} 0.230×10^{-3}	0.000×10^{0} 0.000×10^{0}
6.5 - 7.0	0.249×10^{-3} 0.253×10^{-3}	0.200×10^{-3} 0.204×10^{-3}	0.000×10^{0} 0.468×10^{-3}	0.000×10^{0} 0.621×10^{-3}	0.000×10^{0} 0.579×10^{-3}	0.000×10^{0} 0.988×10^{-3}	0.000×10^{0} 0.739×10^{-3}	0.000×10^{0} 0.499×10^{-3}	0.000×10^{0} 0.000×10^{0}	0.000×10^{0} 0.000×10^{0}
7.0 - 7.5	0.000×10^{0} 0.287×10^{-3}	0.000×10^{0} 0.416×10^{-3}	0.000×10^{0} 0.261×10^{-3}	0.000×10^{0} 0.282×10^{-3}	0.000×10^{0} 0.440×10^{-3}	0.000×10^{0} 0.319×10^{-3}	0.000×10^{0} 0.144×10^{-3}	0.000×10^{0} 0.378×10^{-3}	0.000×10^{0} 0.249×10^{-3}	0.000×10^{0} 0.126×10^{-3}

Table III - π^-

$p_T^2 \backslash x_F$	-.1 - .0	.0 - .1	.1 - .2	.2 - .3	.3 - .4	.4 - .5	.5 - .6	.6 - .7	.7 - .8	.8 - .9	.9 - 1.0
.0 - .5	0.122×10^{0} 0.289×10^{-1}	0.134×10^{0} 0.230×10^{-1}	0.113×10^{0} 0.175×10^{-1}	0.120×10^{0} 0.156×10^{-1}	0.794×10^{-1} 0.114×10^{-1}	0.860×10^{-1} 0.118×10^{-1}	0.607×10^{-1} 0.101×10^{-1}	0.661×10^{-1} 0.116×10^{-1}	0.481×10^{-1} 0.113×10^{-1}	0.212×10^{-1} 0.970×10^{-2}	0.103×10^{-1} 0.765×10^{-2}
.5 - 1.0	0.623×10^{-1} 0.192×10^{-1}	0.787×10^{-1} 0.176×10^{-1}	0.756×10^{-1} 0.148×10^{-1}	0.776×10^{-1} 0.127×10^{-1}	0.703×10^{-1} 0.110×10^{-1}	0.617×10^{-1} 0.984×10^{-2}	0.490×10^{-1} 0.863×10^{-2}	0.297×10^{-1} 0.736×10^{-2}	0.258×10^{-1} 0.801×10^{-2}	0.153×10^{-1} 0.790×10^{-2}	0.000×10^{0} 0.673×10^{-2}
1.0 - 1.5	0.507×10^{-1} 0.174×10^{-1}	0.242×10^{-1} 0.926×10^{-2}	0.489×10^{-1} 0.114×10^{-1}	0.474×10^{-1} 0.102×10^{-1}	0.570×10^{-1} 0.976×10^{-2}	0.431×10^{-1} 0.807×10^{-2}	0.376×10^{-1} 0.789×10^{-2}	0.216×10^{-1} 0.637×10^{-2}	0.126×10^{-1} 0.578×10^{-2}	0.789×10^{-2} 0.570×10^{-2}	0.731×10^{-2} 0.772×10^{-2}
1.5 - 2.0	0.195×10^{-1} 0.114×10^{-1}	0.212×10^{-1} 0.880×10^{-2}	0.361×10^{-1} 0.956×10^{-2}	0.307×10^{-1} 0.739×10^{-2}	0.210×10^{-1} 0.572×10^{-2}	0.190×10^{-1} 0.535×10^{-2}	0.275×10^{-1} 0.668×10^{-2}	0.303×10^{-1} 0.709×10^{-2}	0.171×10^{-1} 0.630×10^{-2}	0.725×10^{-2} 0.528×10^{-2}	0.000×10^{0} 0.266×10^{-1}
2.0 - 2.5	0.127×10^{-1} 0.914×10^{-2}	0.146×10^{-1} 0.745×10^{-2}	0.289×10^{-1} 0.861×10^{-2}	0.283×10^{-1} 0.752×10^{-2}	0.182×10^{-1} 0.559×10^{-2}	0.189×10^{-1} 0.574×10^{-2}	0.133×10^{-1} 0.456×10^{-2}	0.106×10^{-1} 0.444×10^{-2}	0.219×10^{-2} 0.221×10^{-2}	0.312×10^{-2} 0.319×10^{-2}	0.000×10^{0} 0.561×10^{-2}
2.5 - 3.0	0.163×10^{-1} 0.974×10^{-2}	0.108×10^{-1} 0.638×10^{-2}	0.128×10^{-1} 0.535×10^{-2}	0.206×10^{-1} 0.641×10^{-2}	0.133×10^{-1} 0.455×10^{-2}	0.808×10^{-2} 0.335×10^{-2}	0.471×10^{-2} 0.275×10^{-2}	0.000×10^{0} 0.183×10^{-2}	0.238×10^{-2} 0.241×10^{-2}	0.000×10^{0} 0.420×10^{-2}	0.000×10^{0} 0.244×10^{-1}
3.0 - 3.5	0.000×10^{0} 0.598×10^{-2}	0.336×10^{-2} 0.339×10^{-2}	0.148×10^{-1} 0.579×10^{-2}	0.856×10^{-2} 0.436×10^{-2}	0.433×10^{-2} 0.252×10^{-2}	0.667×10^{-2} 0.358×10^{-2}	0.808×10^{-2} 0.339×10^{-2}	0.317×10^{-2} 0.319×10^{-2}	0.255×10^{-2} 0.260×10^{-2}	0.000×10^{0} 0.437×10^{-2}	0.000×10^{0} 0.900×10^{-2}
3.5 - 4.0	0.000×10^{0} 0.593×10^{-2}	0.369×10^{-2} 0.374×10^{-2}	0.104×10^{-1} 0.480×10^{-2}	0.656×10^{-2} 0.335×10^{-2}	0.604×10^{-2} 0.308×10^{-2}	0.327×10^{-2} 0.234×10^{-2}	0.458×10^{-2} 0.270×10^{-2}	0.171×10^{-2} 0.173×10^{-2}	0.000×10^{0} 0.338×10^{-2}	0.000×10^{0} 0.471×10^{-2}	-0.784×10^{-2} 0.111×10^{-1}
4.0 - 4.5	0.496×10^{-2} 0.507×10^{-2}	0.155×10^{-1} 0.957×10^{-2}	0.241×10^{-2} 0.243×10^{-2}	0.152×10^{-2} 0.153×10^{-2}	0.326×10^{-2} 0.191×10^{-2}	0.427×10^{-2} 0.252×10^{-2}	0.379×10^{-2} 0.226×10^{-2}	0.616×10^{-2} 0.378×10^{-2}	0.221×10^{-2} 0.228×10^{-2}	0.000×10^{0} 0.202×10^{-2}	0.000×10^{0} 0.531×10^{-2}
4.5 - 5.0	0.835×10^{-2} 0.882×10^{-2}	0.000×10^{0} 0.436×10^{-2}	0.361×10^{-2} 0.261×10^{-2}	0.411×10^{-2} 0.297×10^{-2}	0.437×10^{-2} 0.260×10^{-2}	0.316×10^{-2} 0.187×10^{-2}	0.478×10^{-2} 0.288×10^{-2}	0.000×10^{0} 0.186×10^{-2}	0.000×10^{0} 0.249×10^{-2}	0.000×10^{0} 0.110×10^{-1}	0.000×10^{0} 0.469×10^{-2}
5.0 - 5.5	0.125×10^{-1} 0.100×10^{-1}	0.000×10^{0} 0.300×10^{-2}	0.218×10^{-2} 0.222×10^{-2}	0.192×10^{-2} 0.196×10^{-2}	0.000×10^{0} 0.112×10^{-2}	0.297×10^{-2} 0.177×10^{-2}	0.879×10^{-3} 0.891×10^{-3}	0.000×10^{0} 0.201×10^{-2}	0.000×10^{0} 0.485×10^{-2}	0.000×10^{0} 0.314×10^{-2}	0.000×10^{0} 0.688×10^{-2}
5.5 - 6.0	0.000×10^{0} 0.517×10^{-2}	0.000×10^{0} 0.218×10^{-2}	0.665×10^{-2} 0.503×10^{-2}	0.756×10^{-2} 0.369×10^{-2}	0.000×10^{0} 0.215×10^{-2}	0.173×10^{-2} 0.178×10^{-2}	0.148×10^{-2} 0.153×10^{-2}	0.000×10^{0} 0.153×10^{-2}	0.000×10^{0} 0.732×10^{-2}	0.000×10^{0} 0.113×10^{-1}	0.000×10^{0} 0.156×10^{-2}
6.0 - 6.5	0.374×10^{-2} 0.400×10^{-2}	0.393×10^{-2} 0.421×10^{-2}	0.179×10^{-2} 0.185×10^{-2}	0.125×10^{-2} 0.128×10^{-2}	0.196×10^{-2} 0.142×10^{-2}	0.000×10^{0} 0.115×10^{-2}	0.183×10^{-2} 0.194×10^{-2}	0.000×10^{0} 0.153×10^{-2}	0.189×10^{-2} 0.207×10^{-2}	0.000×10^{0} 0.672×10^{-2}	0.000×10^{0} 0.279×10^{-2}
6.5 - 7.0	0.310×10^{-2} 0.335×10^{-2}	0.000×10^{0} 0.188×10^{-2}	0.000×10^{0} 0.254×10^{-2}	0.000×10^{0} 0.122×10^{-2}	0.125×10^{-2} 0.129×10^{-2}	0.880×10^{-3} 0.905×10^{-3}	0.000×10^{0} 0.203×10^{-2}	0.000×10^{0} 0.121×10^{-2}	0.000×10^{0} 0.245×10^{-2}	0.000×10^{0} 0.473×10^{-2}	0.000×10^{0} 0.320×10^{-2}
7.0 - 7.5	0.000×10^{0} 0.169×10^{-1}	0.000×10^{0} 0.900×10^{-2}	0.000×10^{0} 0.225×10^{-2}	0.000×10^{0} 0.207×10^{-2}	0.000×10^{0} 0.107×10^{-2}	0.000×10^{0} 0.806×10^{-3}	0.000×10^{0} 0.494×10^{-3}	0.000×10^{0} 0.137×10^{-1}	0.000×10^{0} 0.102×10^{-2}	0.000×10^{0} 0.535×10^{-2}	0.000×10^{0} 0.186×10^{-2}

Table IV -- Systematic Errors

A summary of the contributions to the systematic error in the measured cross section (see text). If the components are uncorrelated and the errors add in quadrature, the overall systematic error is 5 percent. If the components are completely correlated and the errors add linearly, the overall systematic error is 13 percent. Since the errors are almost completely uncorrelated, the overall error of 8% quoted in the text is conservative.

Source	Error (percent)
Counter and Trigger Efficiency	0.4
Trigger Processor Efficiency	1.0
Reconstruction Efficiency	4.0
Resonance Contamination Correction	1.2
Reinteraction Correction	2.0
Effective Length	1.7
Acceptance	1.2
Beam Normalization	1.5

Table V -- First Order QCD Corrections

The ratio of the first order to LLA cross sections for muon pair production in $\bar{p}W$ collisions as a function of mass and x_F. The entries were calculated from formulae in Reference 5 using the DIS structure functions of Duke and Owens.[29]

M \ x_F	0.0	0.1	0.2	0.3	0.4	0.5	0.6	0.7	0.8	0.9
4.0	1.725	1.727	1.727	1.726	1.722	1.716	1.707	1.695	1.679	1.654
4.5	1.734	1.735	1.736	1.735	1.733	1.729	1.722	1.714	1.703	1.687
5.0	1.744	1.746	1.747	1.747	1.746	1.743	1.740	1.735	1.728	1.720
5.5	1.757	1.759	1.760	1.760	1.760	1.759	1.758	1.756	1.754	1.754
6.0	1.771	1.773	1.774	1.775	1.776	1.777	1.777	1.778	1.781	1.788
6.5	1.787	1.789	1.791	1.792	1.794	1.796	1.798	1.802	1.808	1.822
7.0	1.805	1.807	1.809	1.811	1.813	1.816	1.820	1.826	1.836	1.857
7.5	1.825	1.827	1.829	1.831	1.834	1.839	1.844	1.852	1.866	1.893
8.0	1.847	1.849	1.851	1.854	1.858	1.863	1.870	1.881	1.897	1.930
8.5	1.872	1.874	1.876	1.879	1.884	1.890	1.899	1.911	1.931	1.970
9.0	1.899	1.901	1.903	1.907	1.912	1.920	1.930	1.945	1.968	2.013

Table VI -- Normalization of DIS Experiments

The relative normalizations of several high statistics DIS experiments using various beams and targets. These were found by comparing appropriate forms of $\int F_2(x)dx$ where Q^2 overlaps in references 29, 30, 31, and 32. The approximate fractional systematic error of each experiment is given in the last column.

Exp.	Beam	Target	EMC(μH_2)/Exp.	Exp. Sys. Error
EMC	μ	H_2	1	.03
EMC	μ	Fe	1.03	.03
EMC	μ	D_2	1.05	.03
CDHS	ν	Fe	0.96	.06
CCFRR	ν	Fe	0.94	.06
BFP	μ	Fe	0.98	.03
SLAC	e	H_2	0.92	.03

Table VII -- Structure Function Parameters

Results of fitting the $\bar{p}$ and π^- valence quark structure functions to the form $ax^\alpha(1-x)^\beta$ under various assumptions concerning the normalization and target structure function as described in the text. Brackets, <>, indicate that a parameter was fixed in the fit.

Fit	Target Str. Fn.	Norm Method	α	β	a	K
			(a) $\bar{p}$			
1	Free	Num. Sum	<0.5>	3.570±0.213		4.37
2	Free	Num. Sum	0.678±0.211	3.711±0.274		2.37
3	Free	Mom. Sum	<0.5>	3.574±0.213		3.01
4	Free	Mom. Sum	0.685±0.253	3.717±0.294		2.60
5	Free	DIS	<0.5>	3.575±0.213		<2.41>
6	Free	DIS	0.677±0.027	3.710±0.300		<2.41>
7	DIS($Q^2=M^2$)	DIS	<0.5>	3.421±0.195		<2.41>
8	DIS($Q^2=M^2$)	DIS	0.701±0.558	3.622±0.608		<2.41>
9	DIS($Q^2=25$)	DIS	<0.5>	3.456±0.196		<2.41>
10	DIS($Q^2=25$)	DIS	0.640±0.558	3.580±0.611		<2.41>
			(b) π^-			
11	DIS($Q^2=M^2$)	Num. Sum	<0.5>	1.291±0.077	1.0	2.43
12	DIS($Q^2=M^2$)	Num. Sum	0.442±0.207	1.248±0.175	1.0	2.68
13	DIS($Q^2=M^2$)	Mom. Sum	<0.5>	1.289±0.078	0.9481	2.55
14	DIS($Q^2=M^2$)	Mom. Sum	0.476±0.248	1.272±0.191	0.9814	2.57

Figure Captions

Fig. 1 Feynman diagrams for a) simple Drell-Yan, b) the vertex term, c) the annihilation terms, and d) the Compton terms.

Fig. 2 General layout of the spectrometer used by E-537 to measure high mass dimuon production. The coordinate system used is indicated where the y direction is vertical.

Fig. 3 Reconstructed dimuon vertex positions for the 1.5 absorption length tungsten target. The cuts used in the analysis are indicated.

Fig. 4 Uncorrected dimuon mass spectrum produced by $\bar{p}$ and π^- incident on a tungsten target at 125 GeV/c. The background level is shown by like-sign pairs. The ψ resonance is seen at 3.1 GeV/c^2.

Fig. 5 The energy loss for muons in the various materials used in the spectrometer is shown as functions of the kinetic energy of the muon.

Fig. 6 Relative cross sections for ψ production by π^- as a function of tungsten target thickness. The increase with target thickness is due to reinteraction.

Fig. 7 The efficiency for finding both tracks in a high mass dimuon event as functions of mass and x_F.

Fig. 8 Acceptance of the E-537 spectrometer as a function of the muon pair kinematic variables (a) M, (b) x_F, (c) p_T^2, (d) $\cos\theta$, and (e) ϕ.

Fig. 9 The points show the (a) mass, (b) x_F, and (c) p_T^2 distributions for the $\bar{p}$ produced and π^- produced data. In the case of the mass and p_T^2 distributions, the vertical scale is broken and the $\bar{p}$ and π^- data offset by one decade to avoid excessive overlap. The curves are the predictions of the maximum liklihood fits (Table II(b)).

Fig. 10 The points show the (a) x_F and (b) mass distributions of the $\bar{p}$ produced data. The solid line shows the shape of the cross section predicted by the Drell-Yan model (LLA) using DIS structure functions[29] for both the $\bar{p}$ and nucleon. The curve has been multiplied by a factor of 2.41 to reproduce the measured total cross section for $4.0<M<9.0$ GeV/c^2 with $x_F>0$. The other curves show the components of the predicted cross section as indicated.

Fig. 11 The x_F distribution of the $\bar{p}$ produced data compared to the first order QCD and Drell-Yan model (LLA) predictions. The curves have been multiplied by a factor 1.39, so that the first order QCD prediction reproduces the measured total cross section for $4.0<M<9.0$ GeV/c^2 with $x_F>0$.

Fig. 12 $M^3 d\sigma/dM$ as a function of $\sqrt{\tau}$ for the $\bar{p}$ produced data in this experiment and for the data of Ref. 38 at 150 GeV/c. The solid curve is the prediction of the Drell-Yan model (LLA) integrated over $x_F>0$.

Fig. 13 Our measurement of the scaling cross section $s^{3/2}d\sigma/dM$ with $x_F>0$ for the production of muon pairs in π^-N interactions is shown together with data obtained by the CIP[39] and Omega[40] collaborations as a function of $\sqrt{\tau}$.

Fig. 14 Our measurement of the cross section $sd\sigma/dx_F$ for $0.27<\sqrt{\tau}<0.44$ compared to data obtained by the CIP collaboration in the same region of $\sqrt{\tau}$.

Fig. 15 xF_3 and $\int_x^1 xF_3\,dx/x$ measured by the CCFRR collaboration[30] at $Q^2 = 3$ $(GeV)^2$. Only ~1/4 of $\int_0^1 xF_3\,dx/x = \int_0^1 (u_v+d_v)/x\,dx$ lies above $x = 0.2$.

Fig. 16 The points are the projection of the beam structure function $[K\bullet BEAM(x_1) = K\bullet(4\ u_v^p(x_1) + d_v^p(x_1))]$ for the $\bar{p}$ data. The dot-dashed line shows the prediction of Fit 7 in Table 7, with α fixed to 0.5. The dashed line shows the curve corresponding to Fit 8 with α free. The dot-blank line and the dotted line show the value of the deep inelastic structure functions[29] with $Q^2=M^2$ and with $Q^2=25(GeV)^2$, respectively.

Fig. 17 Our projected $\bar{p}$ valence quark structure function $(K\bullet BEAM(x_1))$ is compared with data obtained by the NA3 collaboration.[38]

Fig. 18 The data points are the projected $\bar{p}$ beam structure function ($K \bullet BEAM(x_1)$). The solid curve is the prediction of the Drell-Yan model (7) using DIS structure functions.[29] The dashed curve is the prediction if one ignores the second and third terms on the RHS of (7), in which case the cross section can be written exactly as the product of a function of x_1 and a function of x_2.

Fig. 19 The points are the projection of the target structure function [$K \bullet TARGET(x_2) = K \bullet (Z/A\ u_v^p(x_2) + (1 - Z/A)\ d_v^p(x_2) + Sea^p(x_2))$] for the $\bar{p}$ data. The curve is the prediction of the Drell-Yan model using DIS structure functions.[29]

Fig. 20 The points are the projection of the beam structure function ($K \bullet V^{\pi}(x_1)$) for the π^- data. The curve shows the pion valence quark structure function fit using the parameters of either Fit 11 of Table 7 with α fixed to 0.5 or Fit 12 with α free.

Fig. 21 The points are the projection of the beam structure function, $K \bullet V^{\pi}(x_1)$, for the π^- data. The dashed curve is the prediction of (9) using Fit 11 of Table 7. The solid curve is the same prediction if one ignores the second term on the RHS of (9), in which case the cross section can be written exactly as the product of a function of x_1 and a function of x_2.

Fig. 22 The points are the projection of the target structure function ($K \bullet TARGET(x_2)$) for the π^- data. The curve is the prediction of the Drell-Yan model using DIS structure functions.[29]

Fig. 23 Our projected pion valence quark structure function $(K\bullet V^{\pi}(x_1))$ compared with data from the NA3[42], CIP[45], and Goliath[46] experiments. There is good agreement among the four experiments.

Fig. 24 The angular distributions for the $\bar{p}$ and π^- data in (a) $\cos\theta$ and (b) ϕ. The curves show the $1 + \cos^2\theta$ prediction of the Drell-Yan model. Fluctuations from this prediction near $\cos\theta = -1$ may be caused by the remaining background and the like-sign subtraction as discussed in the text.

Fig. 25 $d\sigma/dp_T^2$ for the $\bar{p}$ and π^- data. The curves are the predictions of the soft gluon model including an intrinsic p_T^2. Figures (a) and (b) show the predictions of the model for $\Lambda = 0.2$GeV and $\langle p_T^2\rangle_{Int} = 0.3$, 0.4, 0.5, 0.6, and 0.7$(\mathrm{GeV}/c)^2$. Figures (c) and (d) show the predictions for $\Lambda = 0.2$ and 0.4GeV using $\langle p_T^2\rangle_{Int} = 0.5(\mathrm{GeV}/c)^2$.

Fig. 26 $\langle p_T^2\rangle$ versus M for $\bar{p}$ and π^- data. The curves are the total and component QCD predictions as indicated, calculated at the average x_F of the data.

Fig. 27 $\langle p_T^2\rangle$ versus x_F for $\bar{p}$ and π^- data. The curves are the total and component QCD predictions as indicated, calculated at the average M^2 of the data.

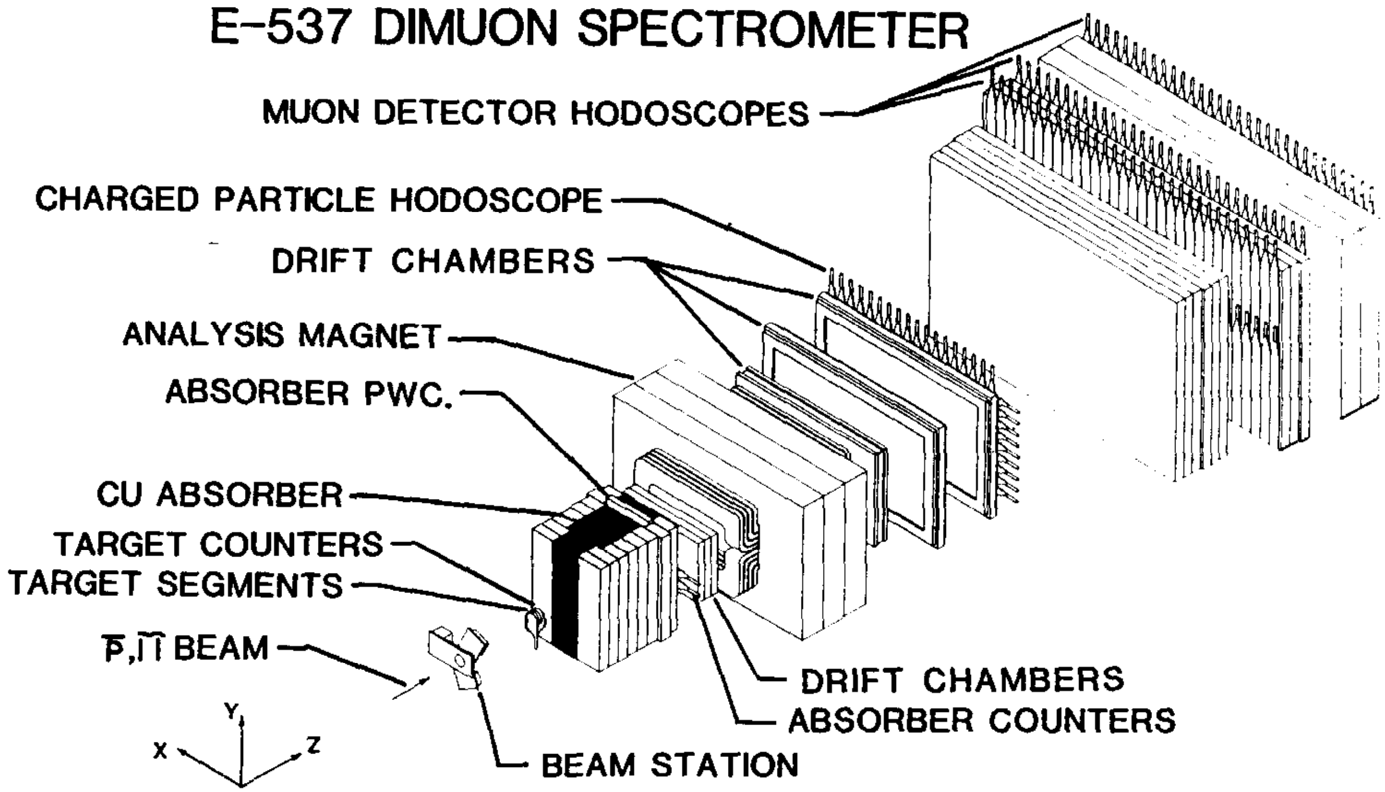
E-537 DIMUON SPECTROMETER
MUON DETECTOR HODOSCOPES
CHARGED PARTICLE HODOSCOPE
DRIFT CHAMBERS
ANALYSIS MAGNET
ABSORBER PWC.
CU ABSORBER
TARGET COUNTERS
TARGET SEGMENTS
$\bar{p},\pi$ BEAM
DRIFT CHAMBERS
ABSORBER COUNTERS
BEAM STATION
Y
X
Z

Fig. 2

Fig. 3

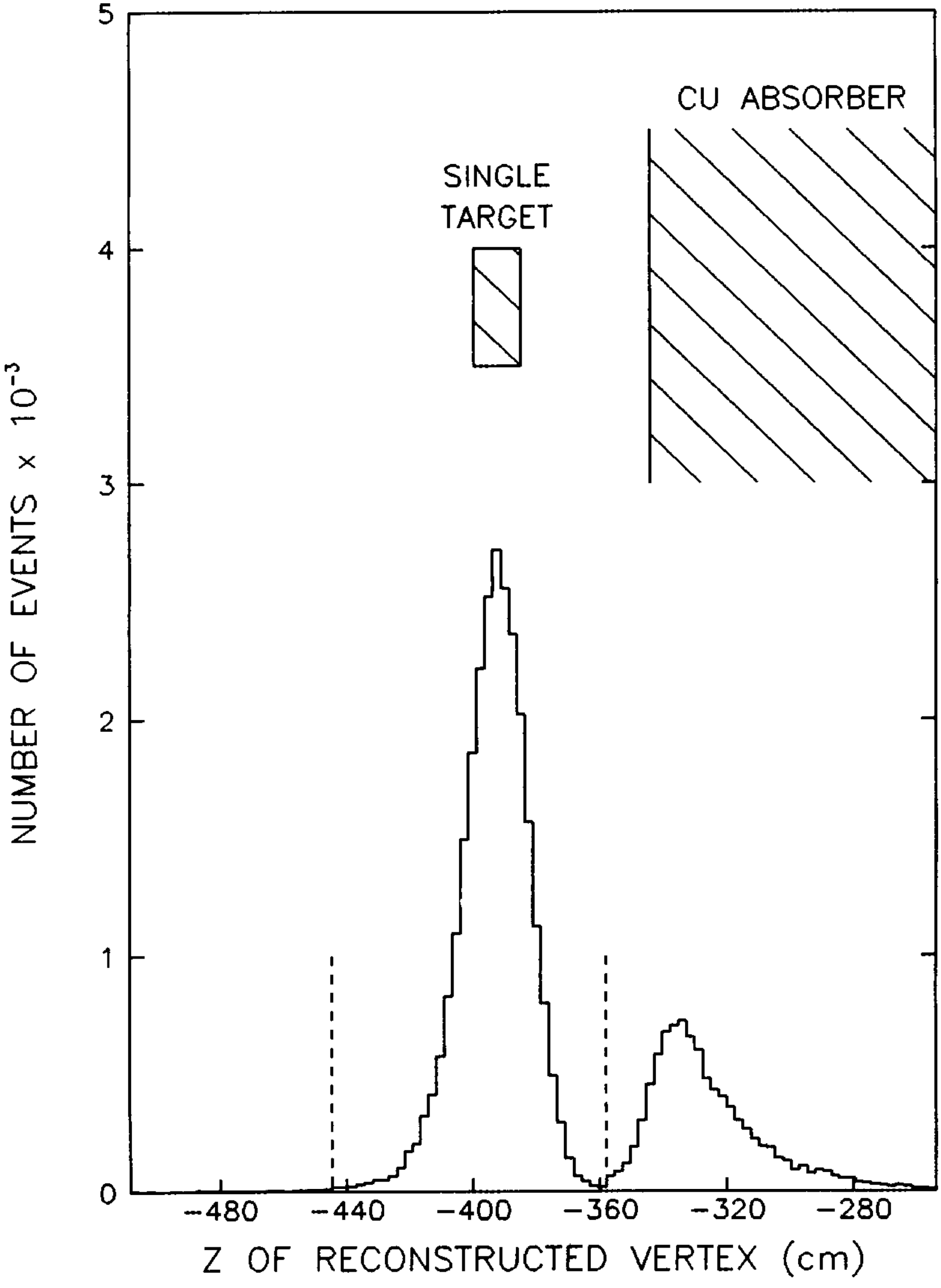
CU ABSORBER
SINGLE
TARGET
NUMBER OF EVENTS × 10^{-3}
0
1
2
3
4
5
−480
−440
−400
−360
−320
−280
Z OF RECONSTRUCTED VERTEX (cm)

Fig. 4

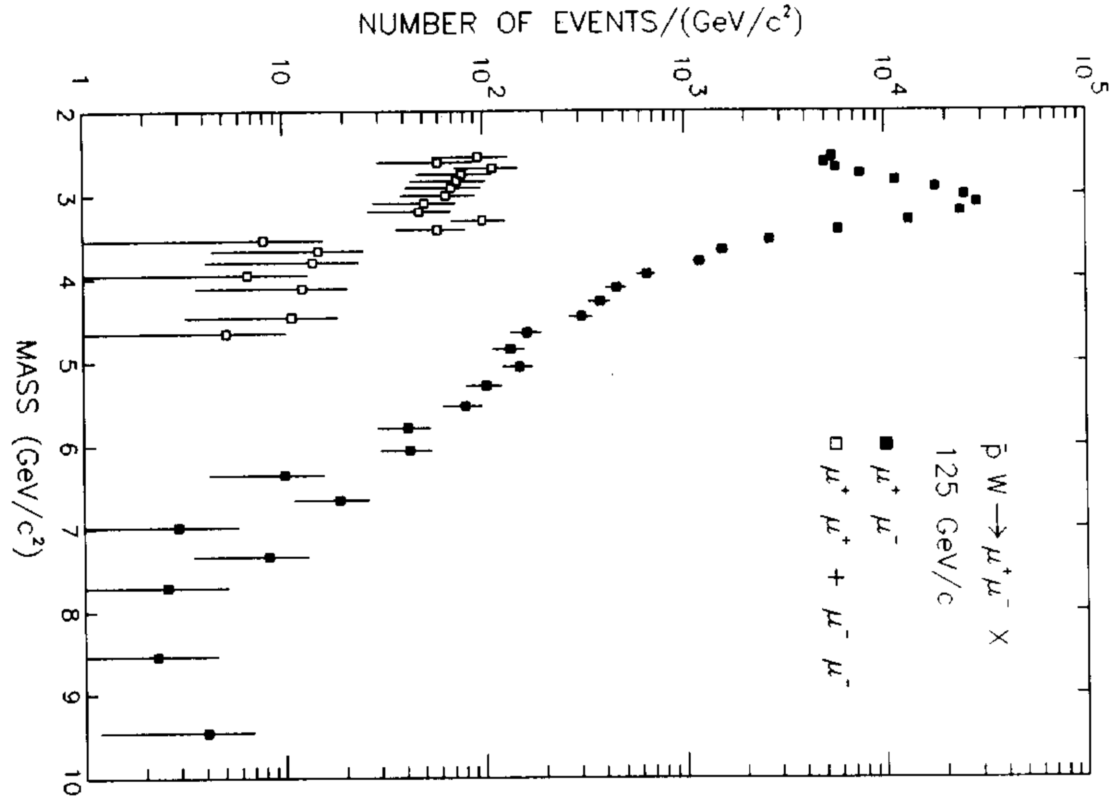
NUMBER OF EVENTS/(GeV/c^2)
MASS (GeV/c^2)
$\bar{p}W \rightarrow \mu^+\mu^- X$
125 GeV/c
$\mu^+ \mu^-$
$\mu^+ \mu^+ + \mu^- \mu^-$

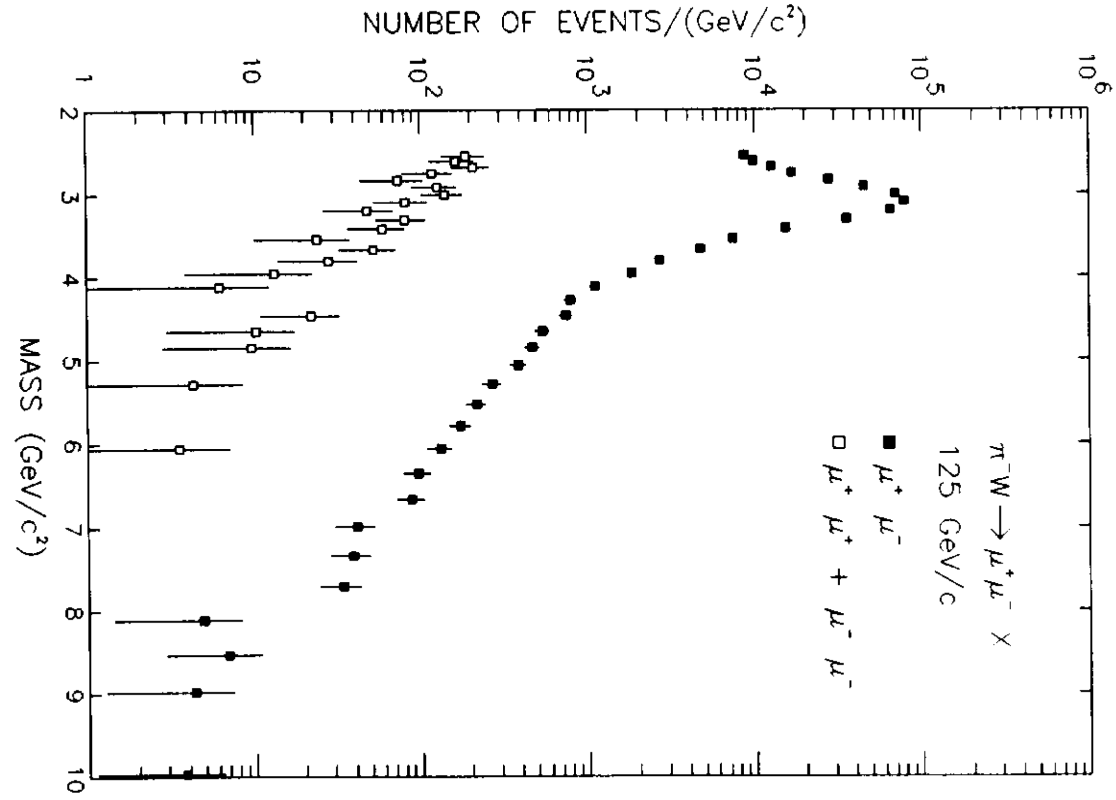
NUMBER OF EVENTS/(GeV/c^2)
MASS (GeV/c^2)
$\pi^- W \rightarrow \mu^+\mu^- X$
125 GeV/c
$\mu^+ \mu^-$
$\mu^+ \mu^+ + \mu^- \mu^-$

Fig. 5

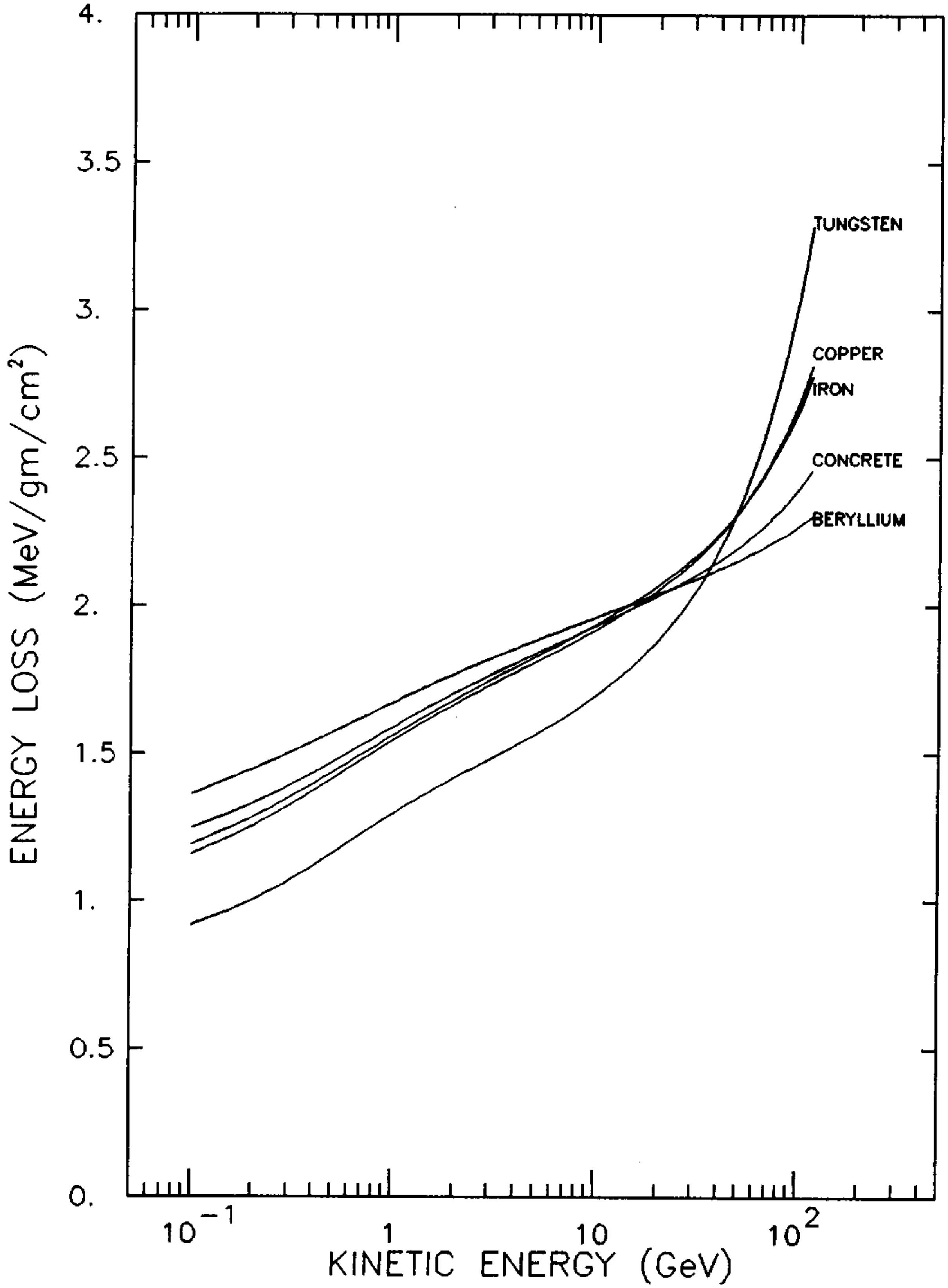
TUNGSTEN
COPPER
IRON
CONCRETE
BERYLLIUM
ENERGY LOSS (MeV/gm/cm²)
KINETIC ENERGY (GeV)
4.
3.5
3.
2.5
2.
1.5
1.
0.5
0.
10⁻¹
1
10
10²

Fig. 6

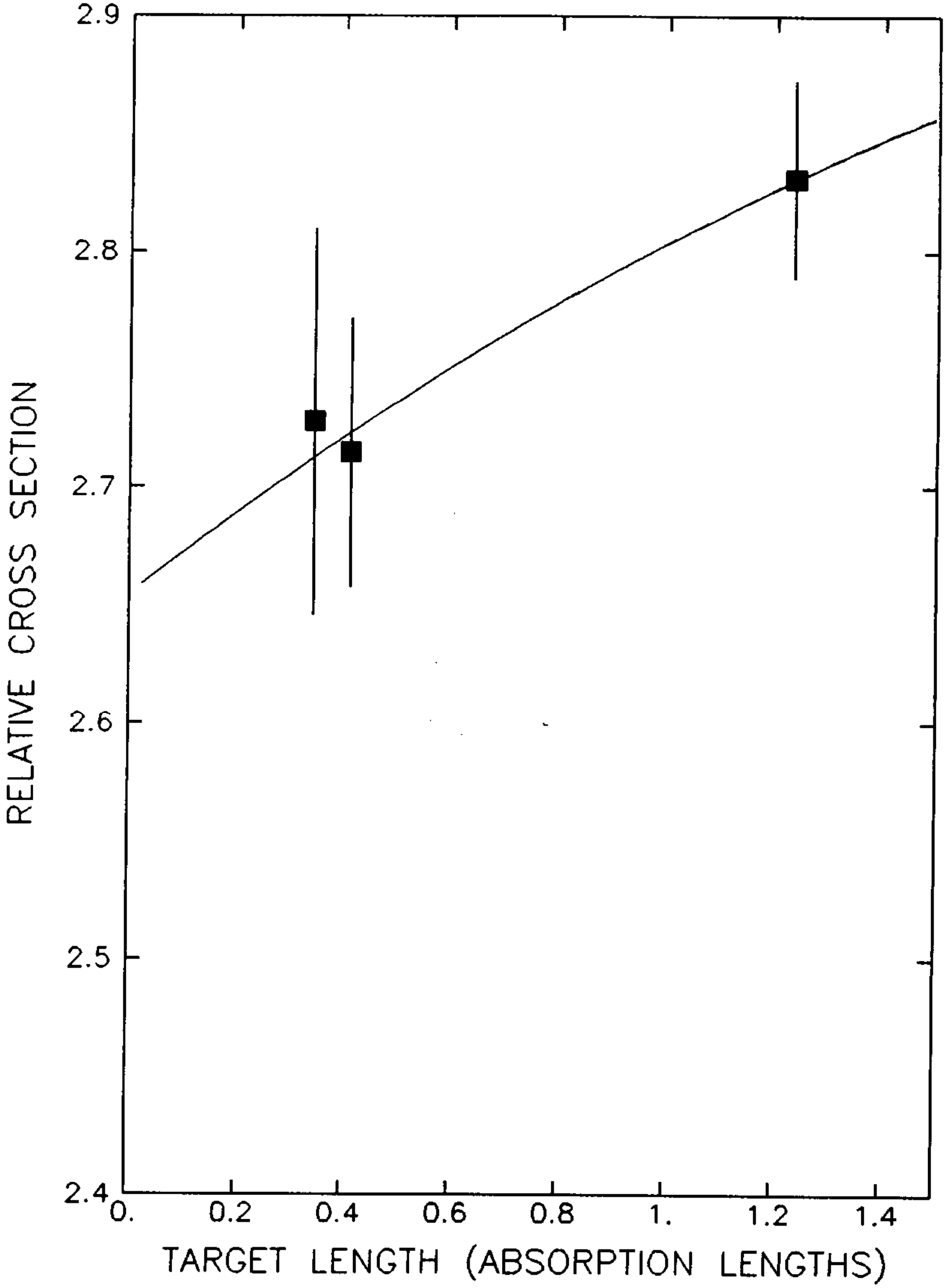

2.9
2.8
2.7
2.6
2.5
2.4
0.
0.2
0.4
0.6
0.8
1.
1.2
1.4
RELATIVE CROSS SECTION
TARGET LENGTH (ABSORPTION LENGTHS)

Fig. 7

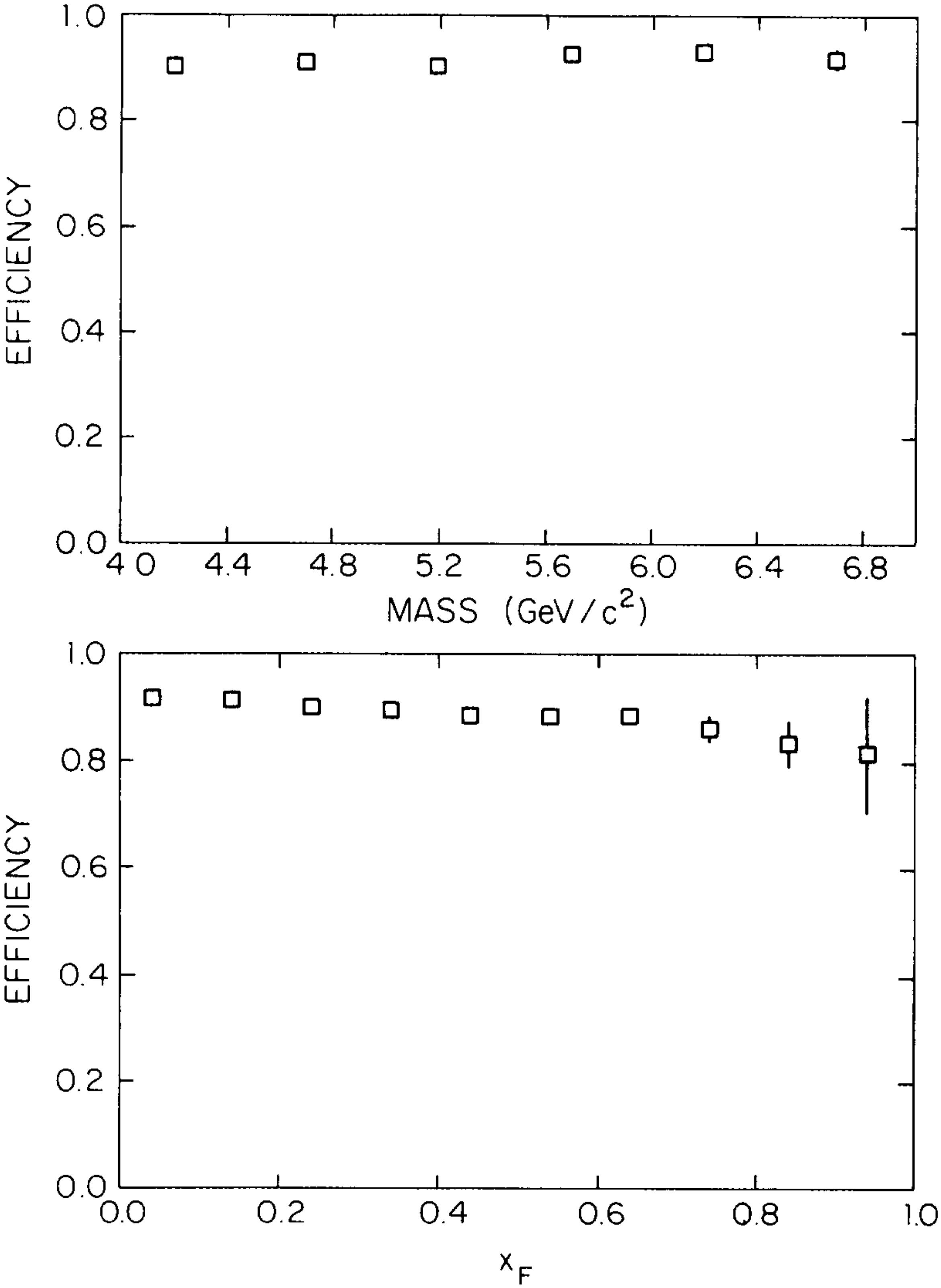
EFFICIENCY
1.0
0.8
0.6
0.4
0.2
0.0
4.0
4.4
4.8
5.2
5.6
6.0
6.4
6.8
MASS (GeV/c^2)
EFFICIENCY
0.0
0.2
0.4
0.6
0.8
1.0
x_F

Fig. 8

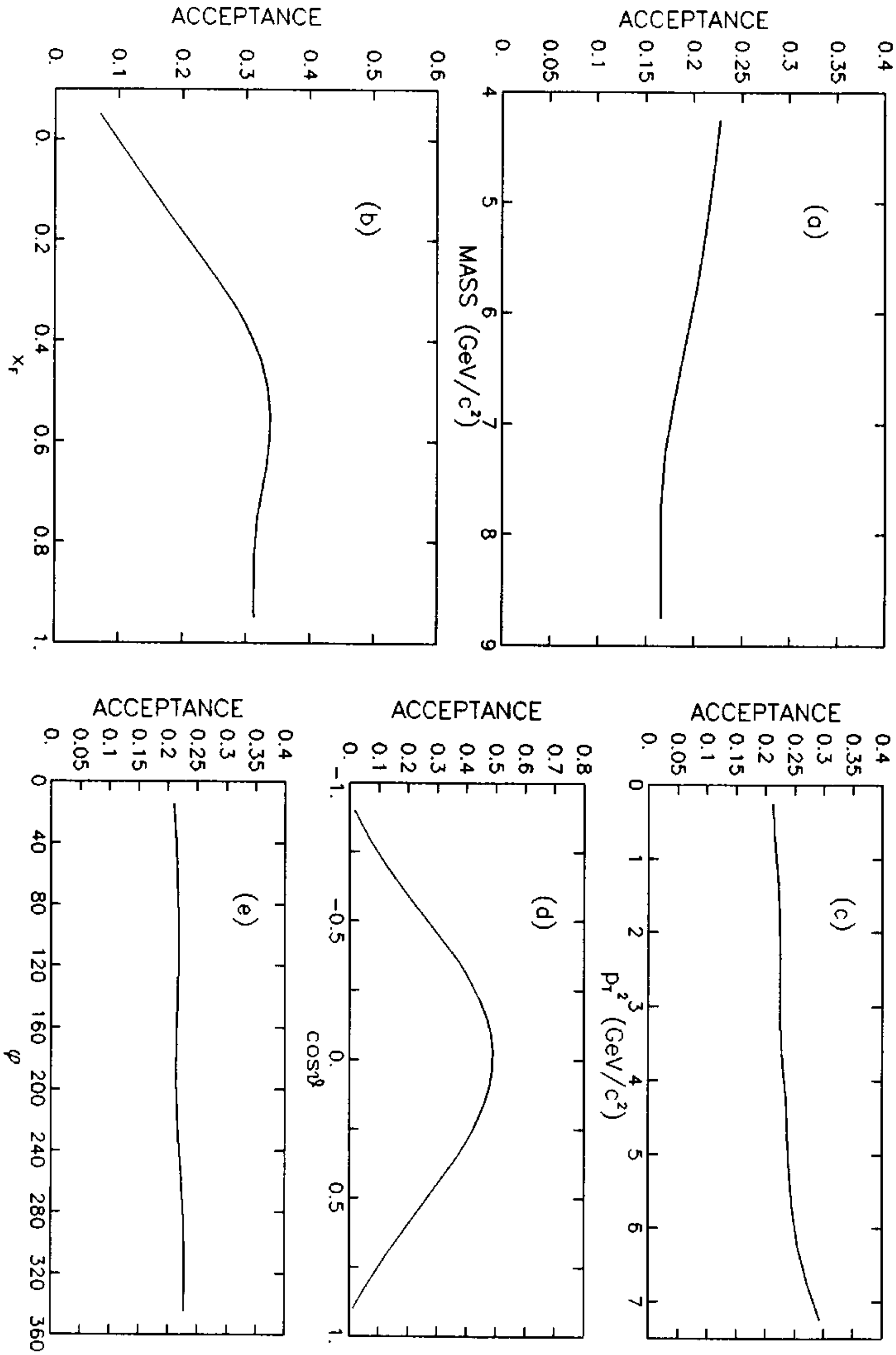

Fig. 9a

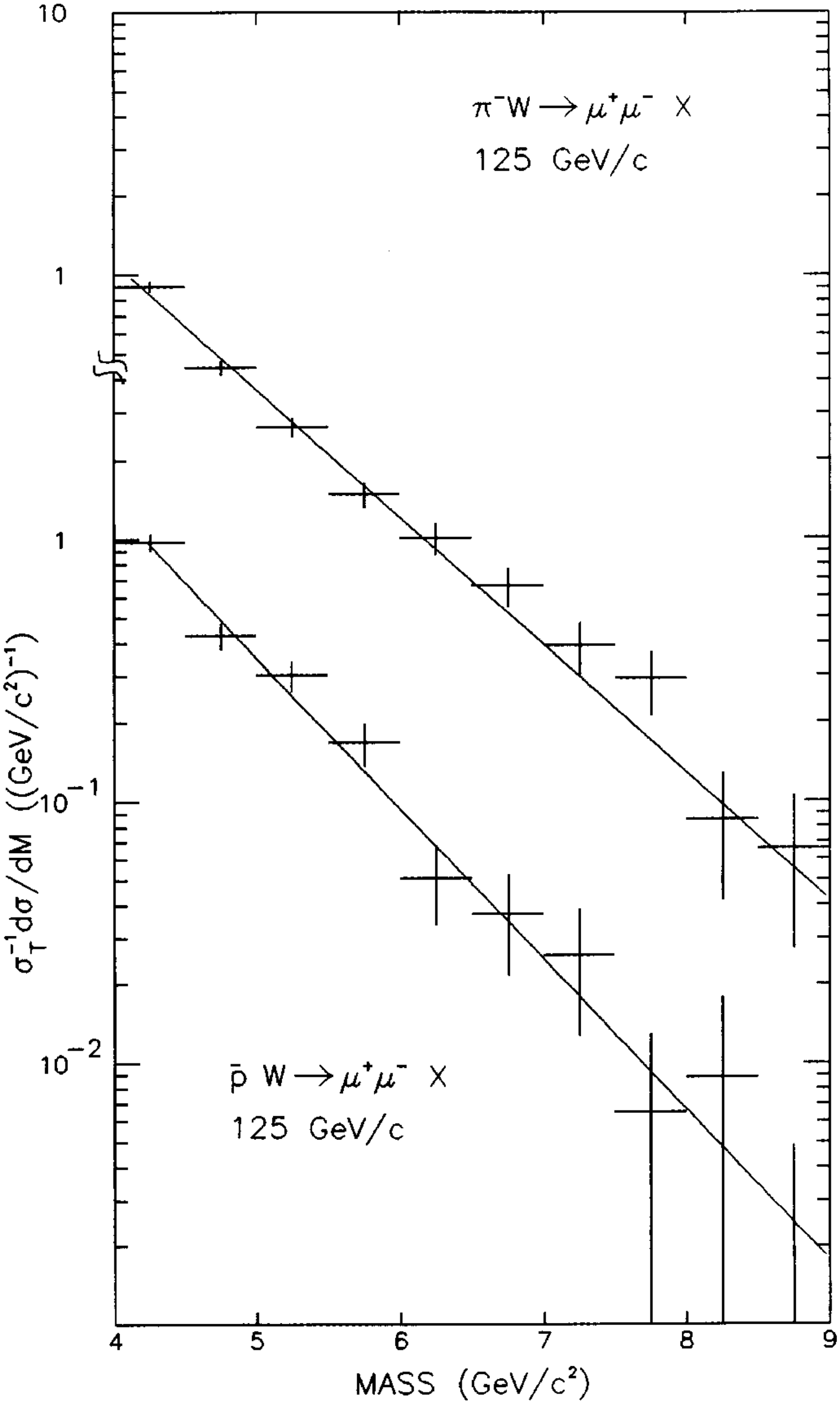

$\pi^- W \rightarrow \mu^+ \mu^- X$
125 GeV/c
$\bar{p}\ W \rightarrow \mu^+ \mu^- X$
125 GeV/c
$\sigma_T^{-1} d\sigma/dM$ $((GeV/c^2)^{-1})$
MASS (GeV/c^2)
10
1
1
10^{-1}
10^{-2}
4
5
6
7
8
9

Fig. 9b

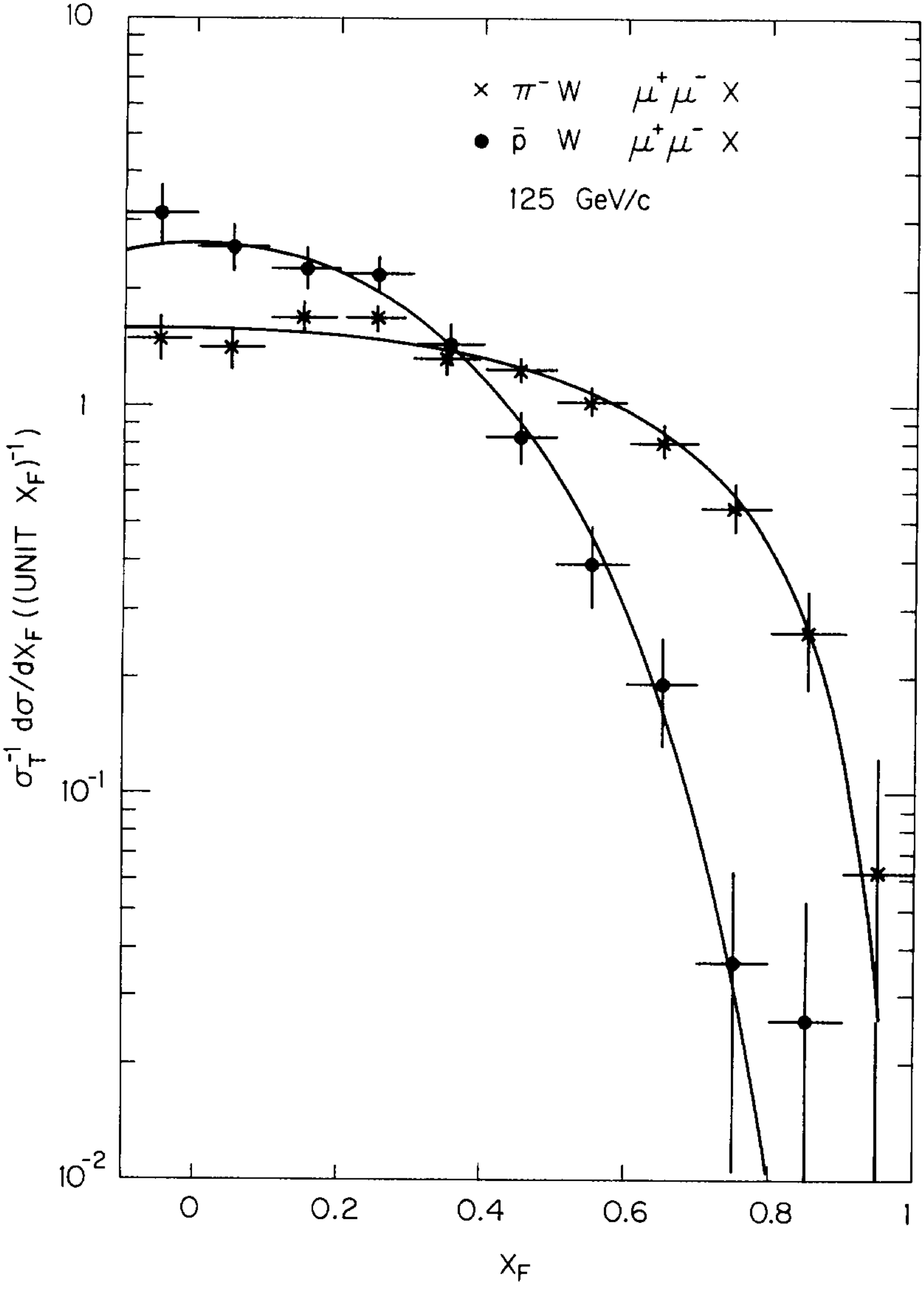
× $\pi^- W \quad \mu^+\mu^- X$
● $\bar{p} \quad W \quad \mu^+\mu^- X$
125 GeV/c
$\sigma_T^{-1}\, d\sigma/dX_F\ ((\mathrm{UNIT}\ X_F)^{-1})$
X_F
10
1
10^{-1}
10^{-2}
0
0.2
0.4
0.6
0.8
1

Fig. 9c

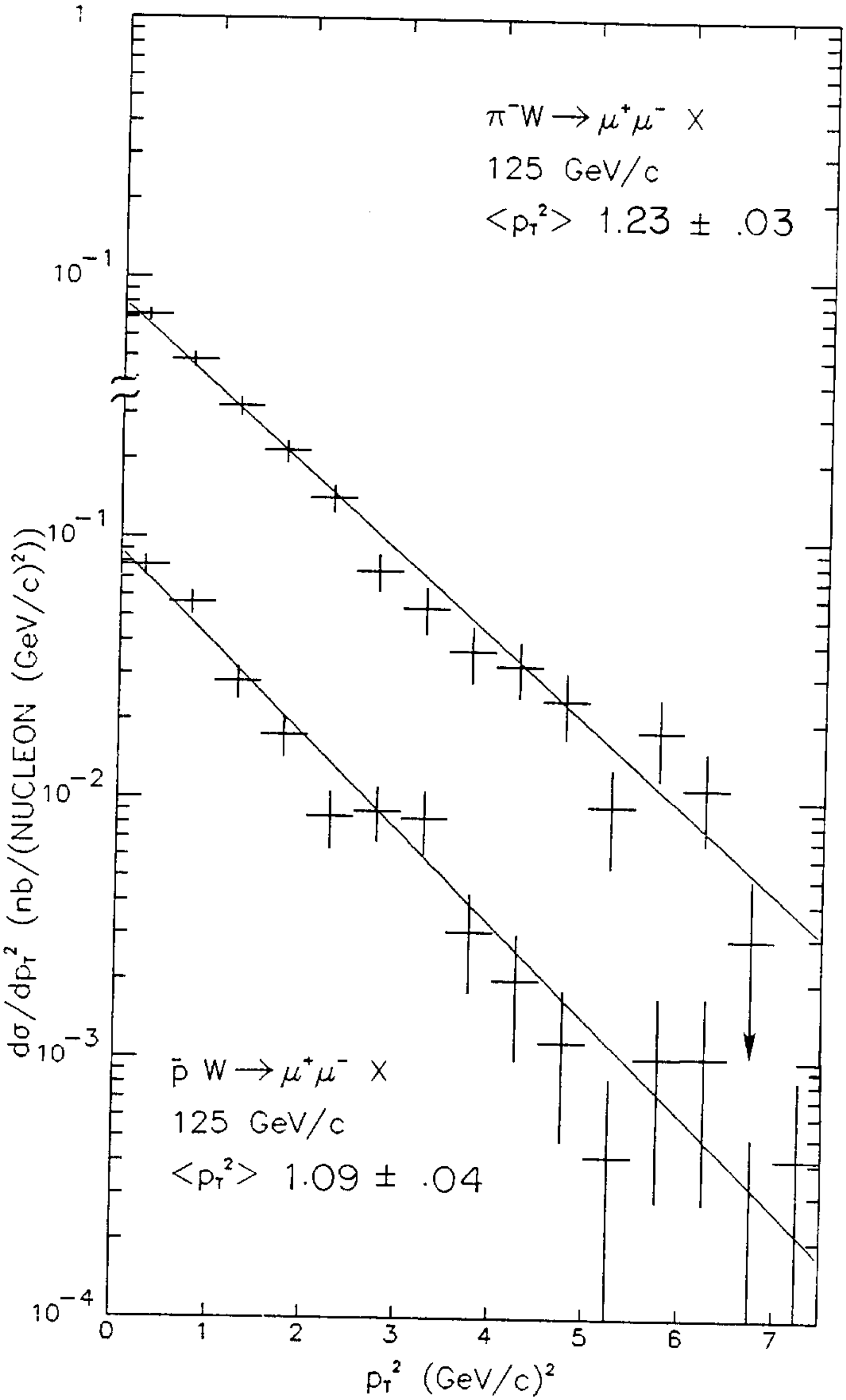

$\pi^- W \to \mu^+\mu^- X$
125 GeV/c
$\langle p_T^2 \rangle$ 1.23 ± .03
$\bar{p}\, W \to \mu^+\mu^- X$
125 GeV/c
$\langle p_T^2 \rangle$ 1.09 ± .04
$d\sigma/dp_T^2$ (nb/(NUCLEON (GeV/c)^2))
p_T^2 (GeV/c)^2
1
10^{-1}
10^{-1}
10^{-2}
10^{-3}
10^{-4}
0
1
2
3
4
5
6
7

Fig. 10a

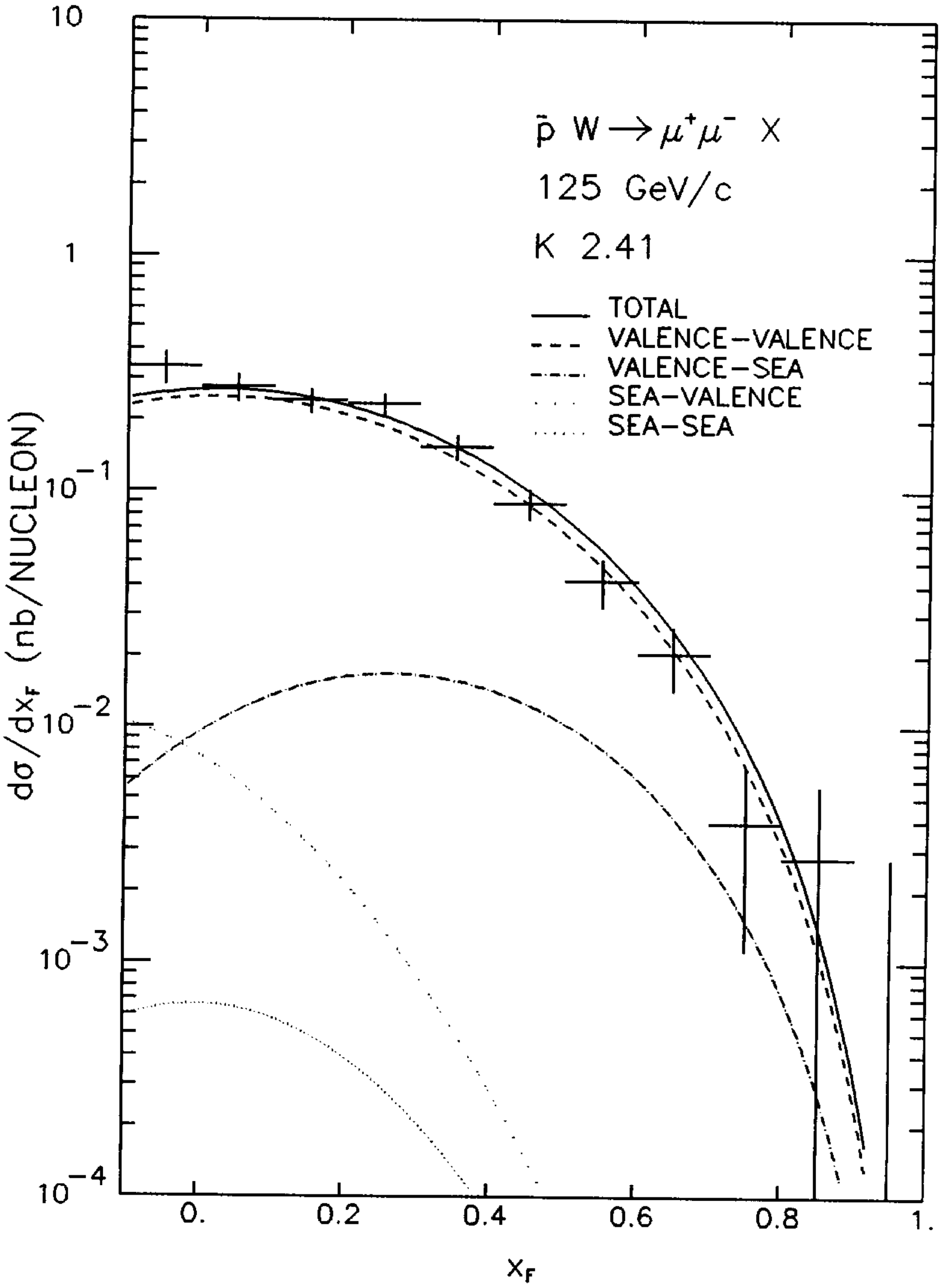

$\bar{p}\ W \rightarrow \mu^+\mu^-\ X$
125 GeV/c
K 2.41
TOTAL
VALENCE-VALENCE
VALENCE-SEA
SEA-VALENCE
SEA-SEA
10
1
10^{-1}
10^{-2}
10^{-3}
10^{-4}
$d\sigma/dx_F$ (nb/NUCLEON)
0.
0.2
0.4
0.6
0.8
1.
x_F

Fig. 10b

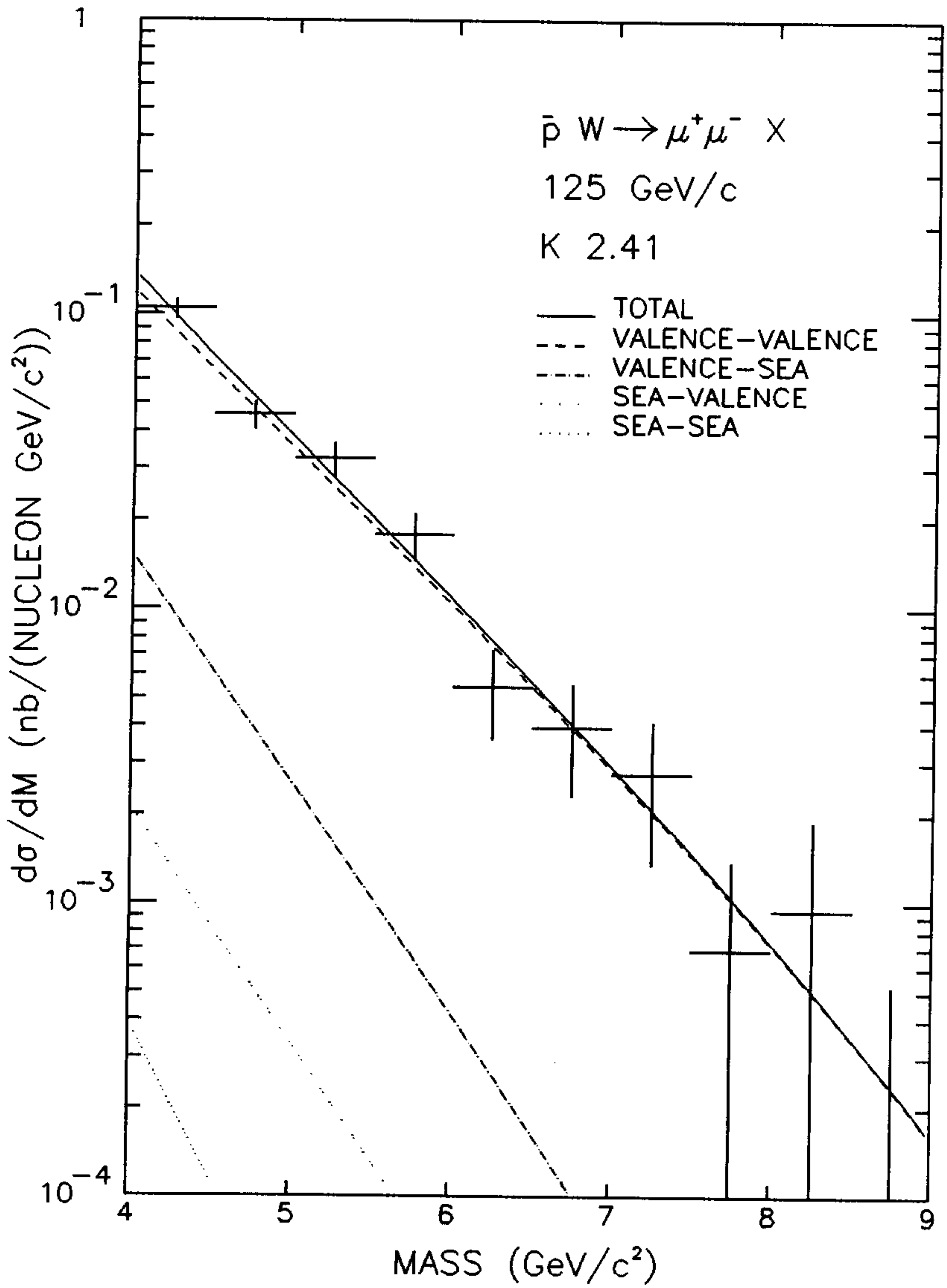

$\bar{p}\,W \rightarrow \mu^+\mu^-\ X$
125 GeV/c
K 2.41
TOTAL
VALENCE-VALENCE
VALENCE-SEA
SEA-VALENCE
SEA-SEA
$d\sigma/dM$ (nb/(NUCLEON GeV/c^2))
MASS (GeV/c^2)
1
10^{-1}
10^{-2}
10^{-3}
10^{-4}
4
5
6
7
8
9

Fig. 11

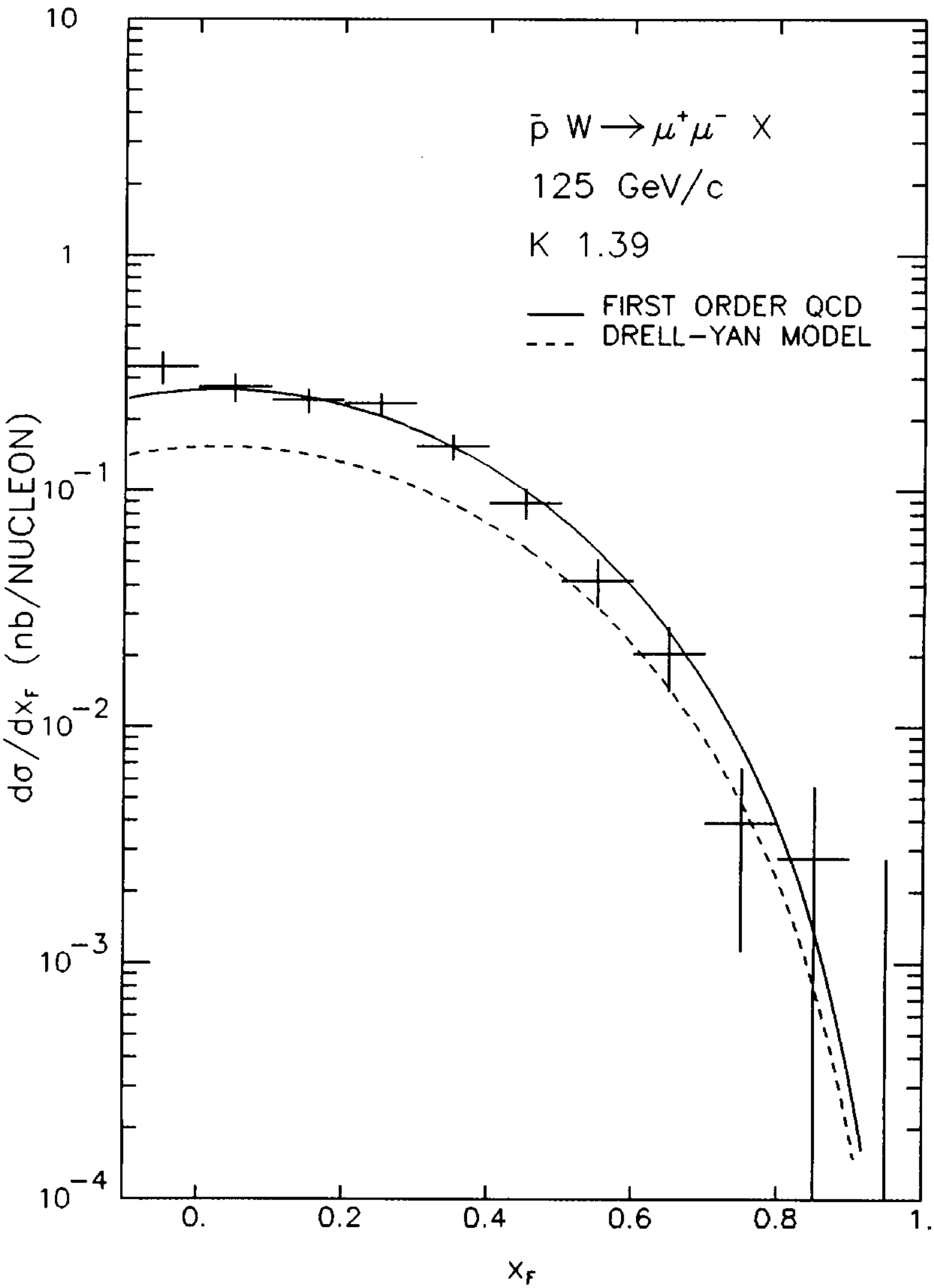

$\bar{p}\ W \rightarrow \mu^+\mu^-\ X$
125 GeV/c
K 1.39
FIRST ORDER QCD
DRELL-YAN MODEL
$d\sigma/dx_F$ (nb/NUCLEON)
x_F
10
1
10^{-1}
10^{-2}
10^{-3}
10^{-4}
0.
0.2
0.4
0.6
0.8
1.

Fig. 12

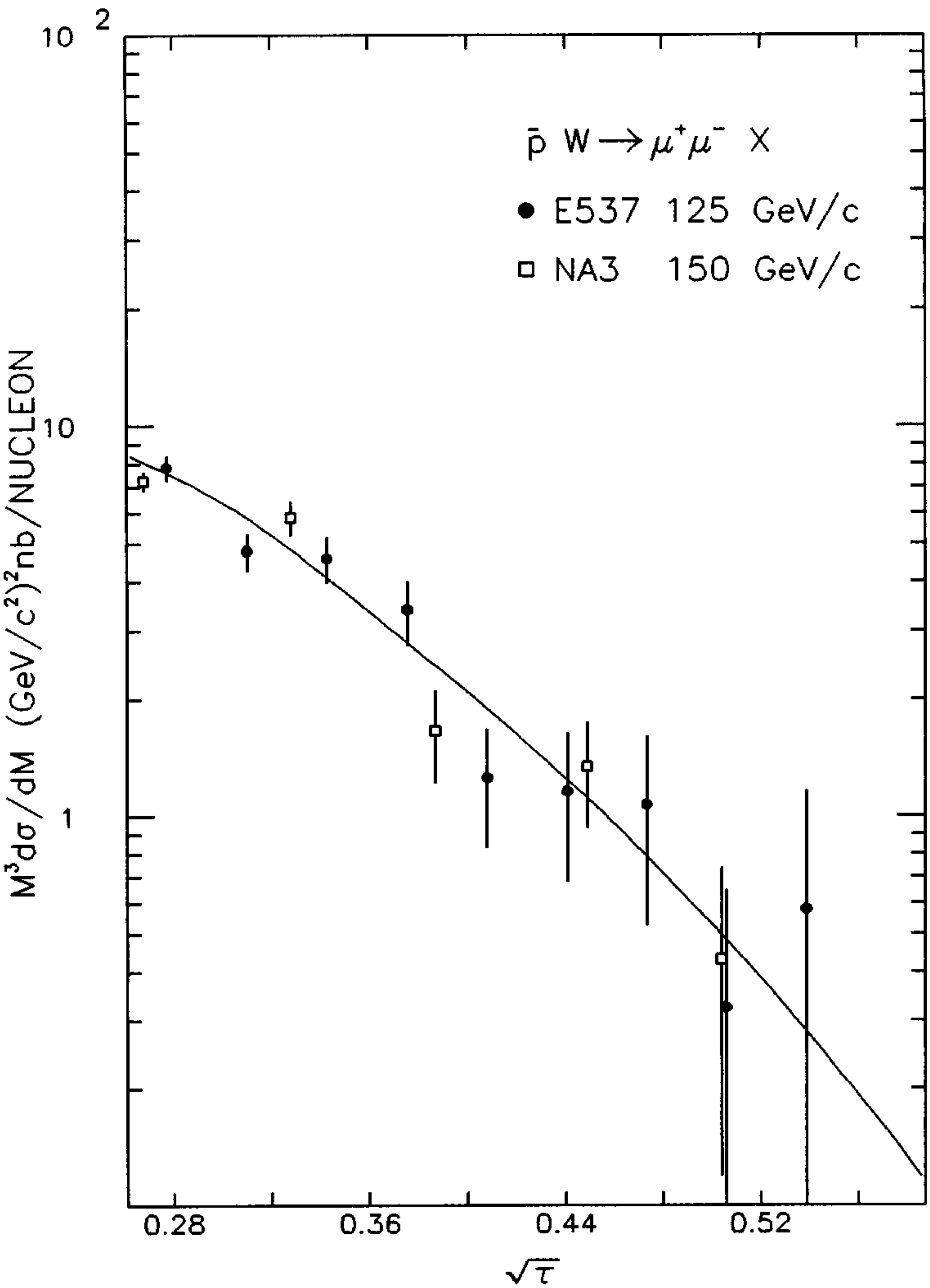

$\bar{p}$ W $\longrightarrow \mu^+\mu^-$ X
E537 125 GeV/c
NA3 150 GeV/c
$M^3 d\sigma/dM$ $(GeV/c^2)^2$nb/NUCLEON
10^2
10
1
0.28
0.36
0.44
0.52
$\sqrt{\tau}$

Fig. 13

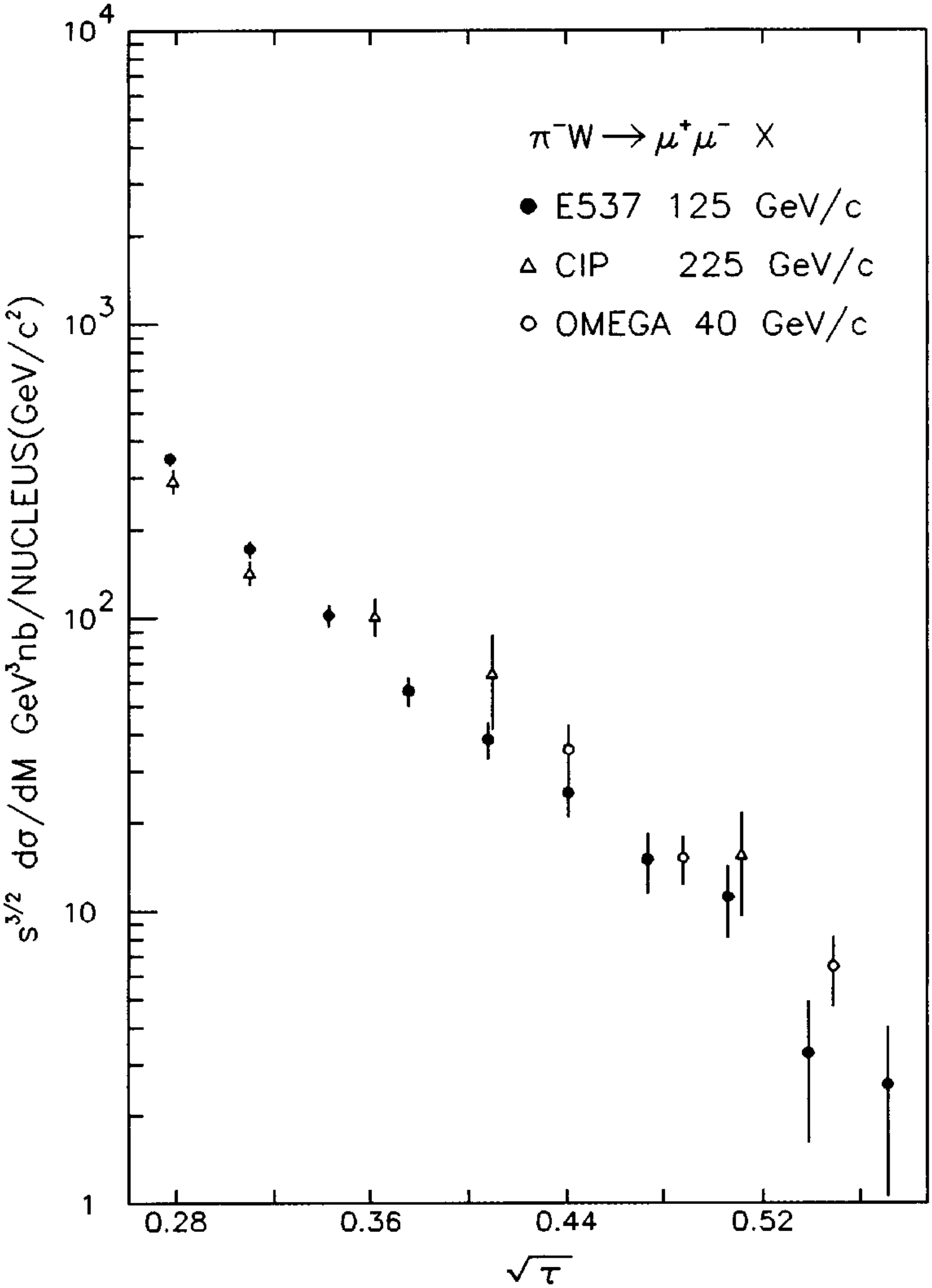
$\pi^- W \rightarrow \mu^+\mu^- X$
E537 125 GeV/c
CIP 225 GeV/c
OMEGA 40 GeV/c
$s^{3/2}$ dσ/dM GeV³nb/NUCLEUS(GeV/c²)
10^4
10^3
10^2
10
1
0.28
0.36
0.44
0.52
$\sqrt{\tau}$

Fig. 14

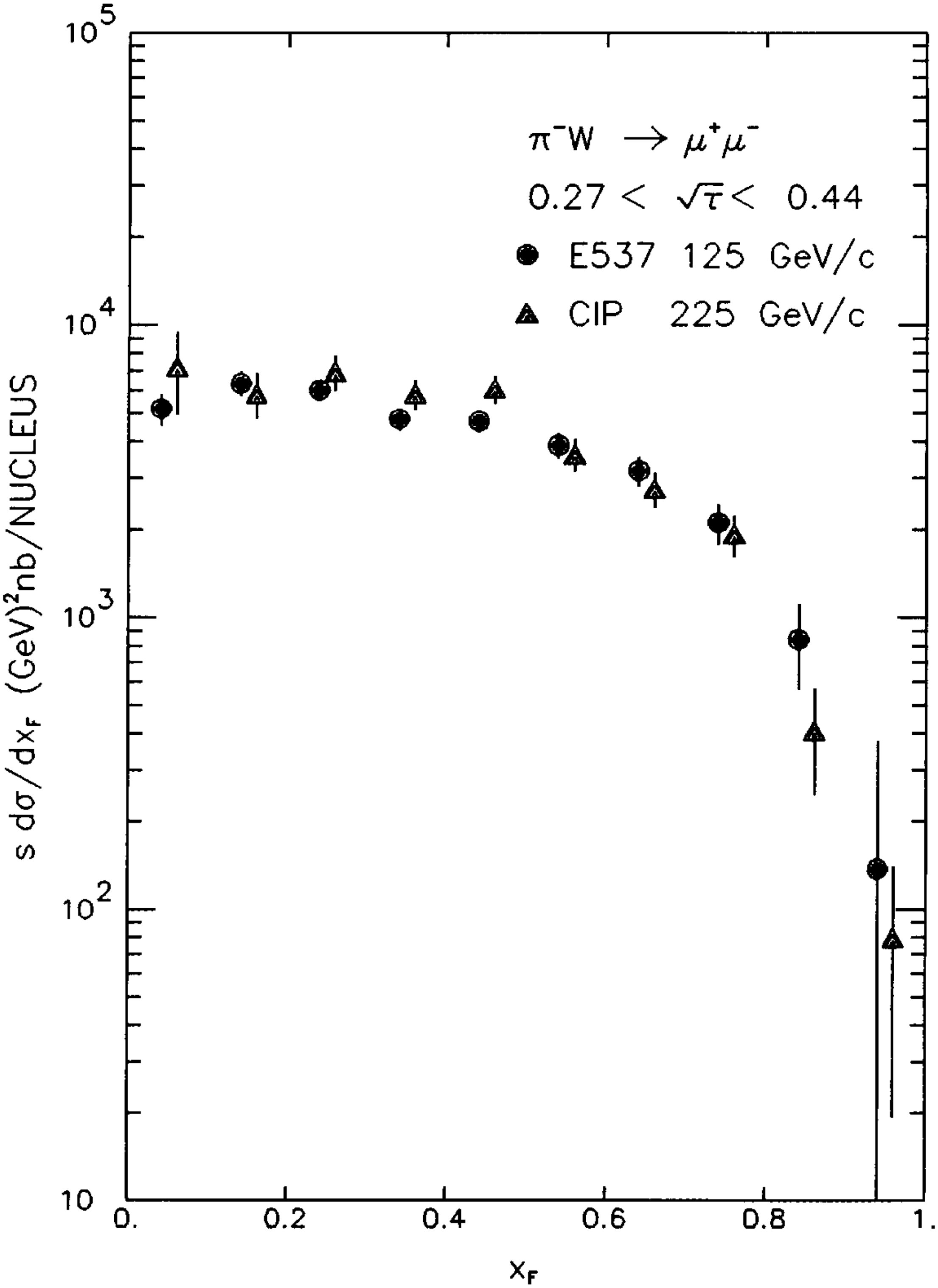

$\pi^- W \rightarrow \mu^+\mu^-$
$0.27 < \sqrt{\tau} < 0.44$
E537 125 GeV/c
CIP 225 GeV/c
10^5
10^4
10^3
10^2
10
0.
0.2
0.4
0.6
0.8
1.
x_F
$s\, d\sigma/dx_F$ $(GeV)^2$nb/NUCLEUS

Fig. 15

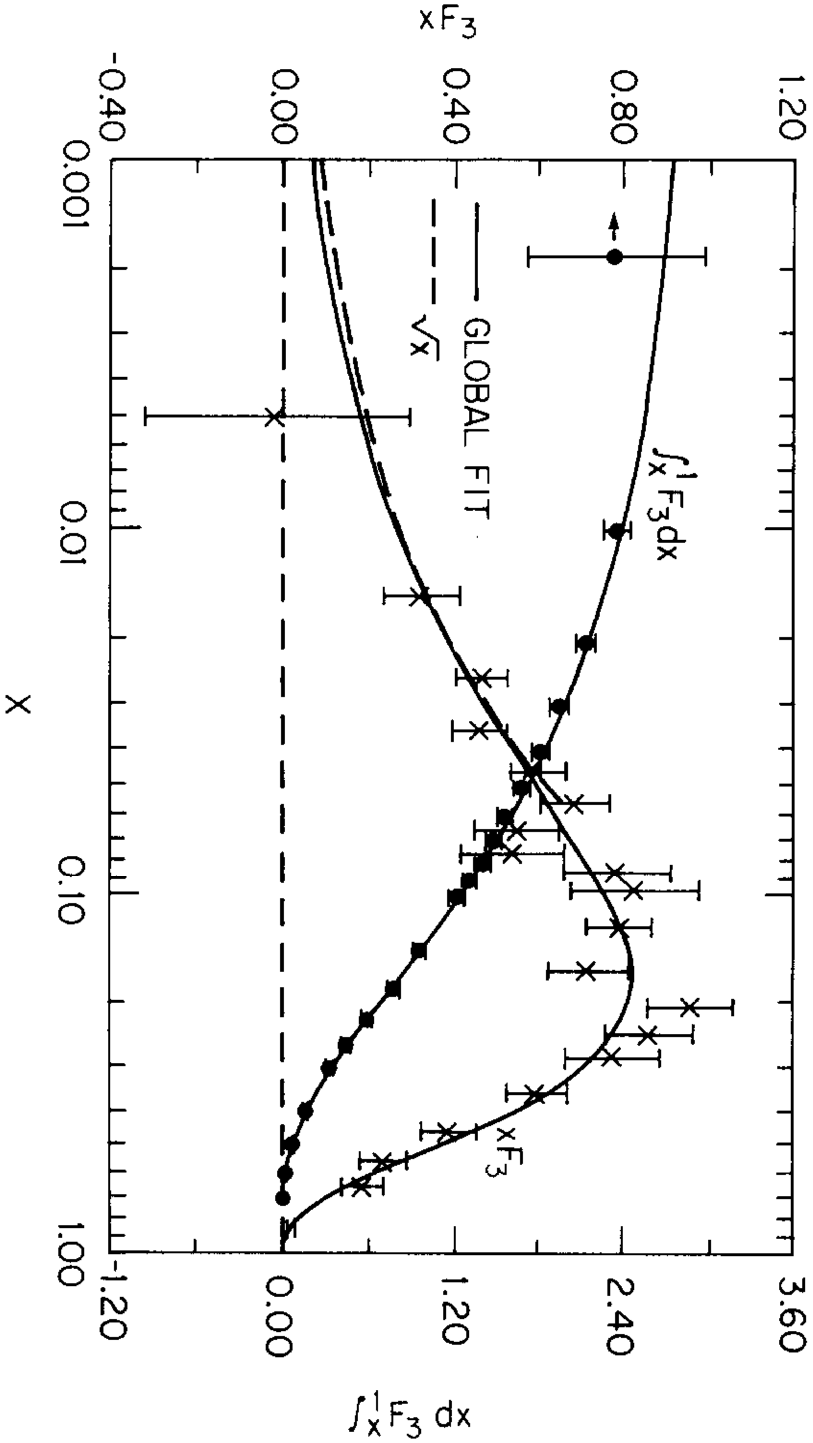

xF_3
-0.40
0.00
0.40
0.80
1.20
0.001
0.01
0.10
1.00
X
GLOBAL FIT
$\sqrt{x}$
$\int_x^1 F_3 dx$
xF_3
-1.20
0.00
1.20
2.40
3.60
$\int_x^1 F_3\, dx$

Fig. 16

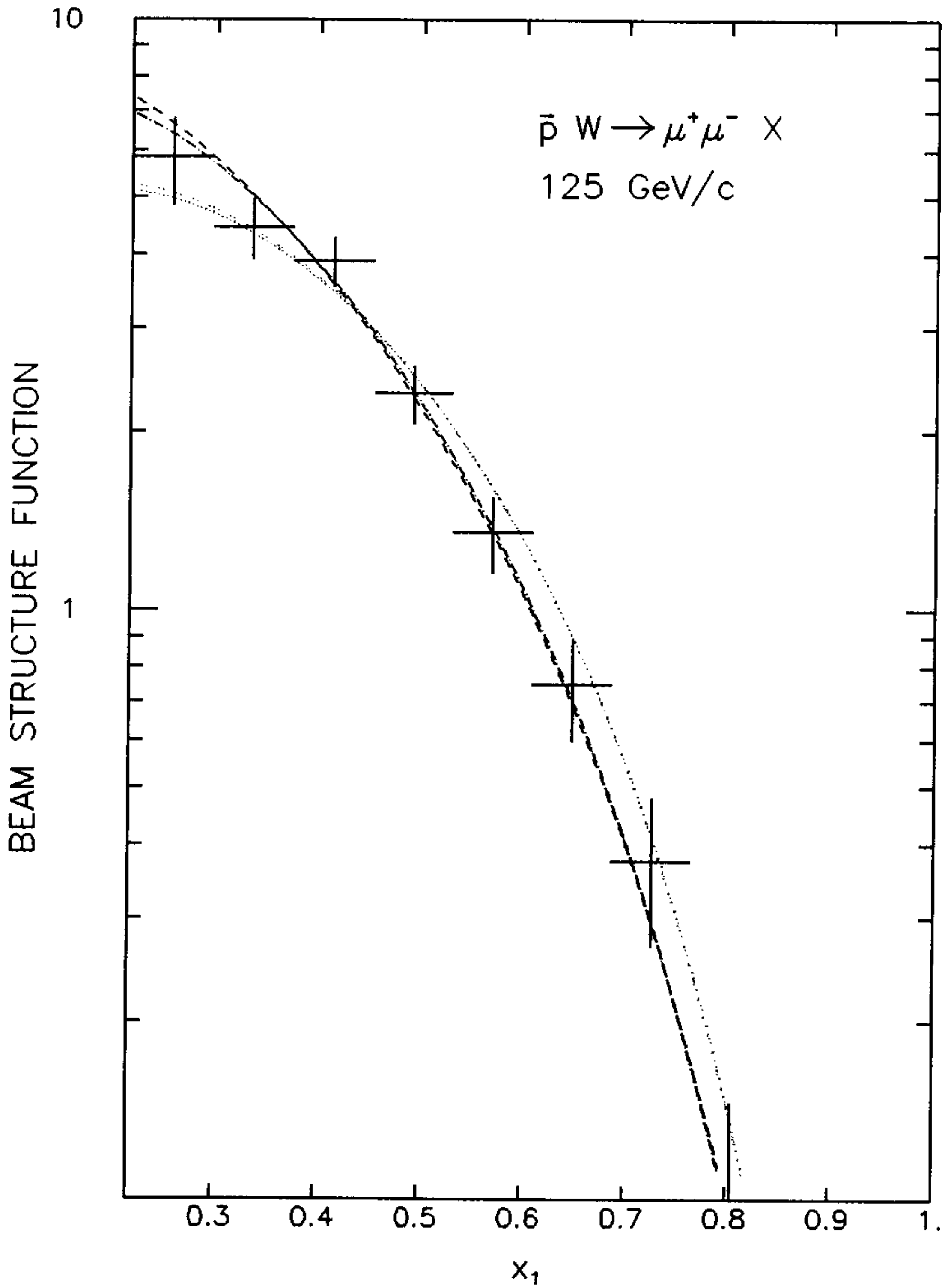

$\bar{p}\ W \rightarrow \mu^+\mu^-\ X$
125 GeV/c
10
1
BEAM STRUCTURE FUNCTION
0.3
0.4
0.5
0.6
0.7
0.8
0.9
1.
x_1

Fig. 17

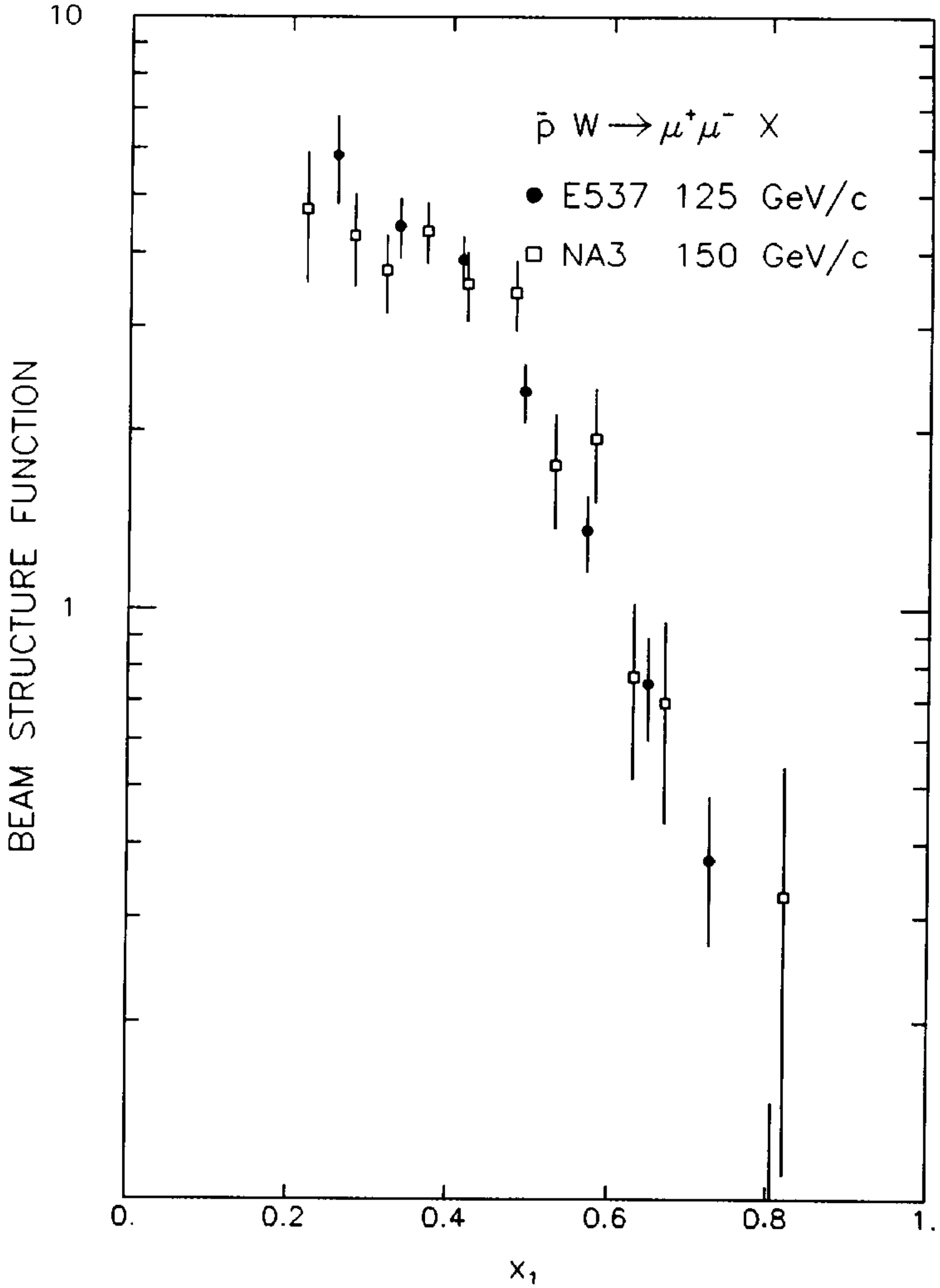

$\bar{p}\ W \longrightarrow \mu^+\mu^-\ X$
● E537 125 GeV/c
□ NA3 150 GeV/c
BEAM STRUCTURE FUNCTION
10
1
0.
0.2
0.4
0.6
0.8
1.
x_1

Fig. 18

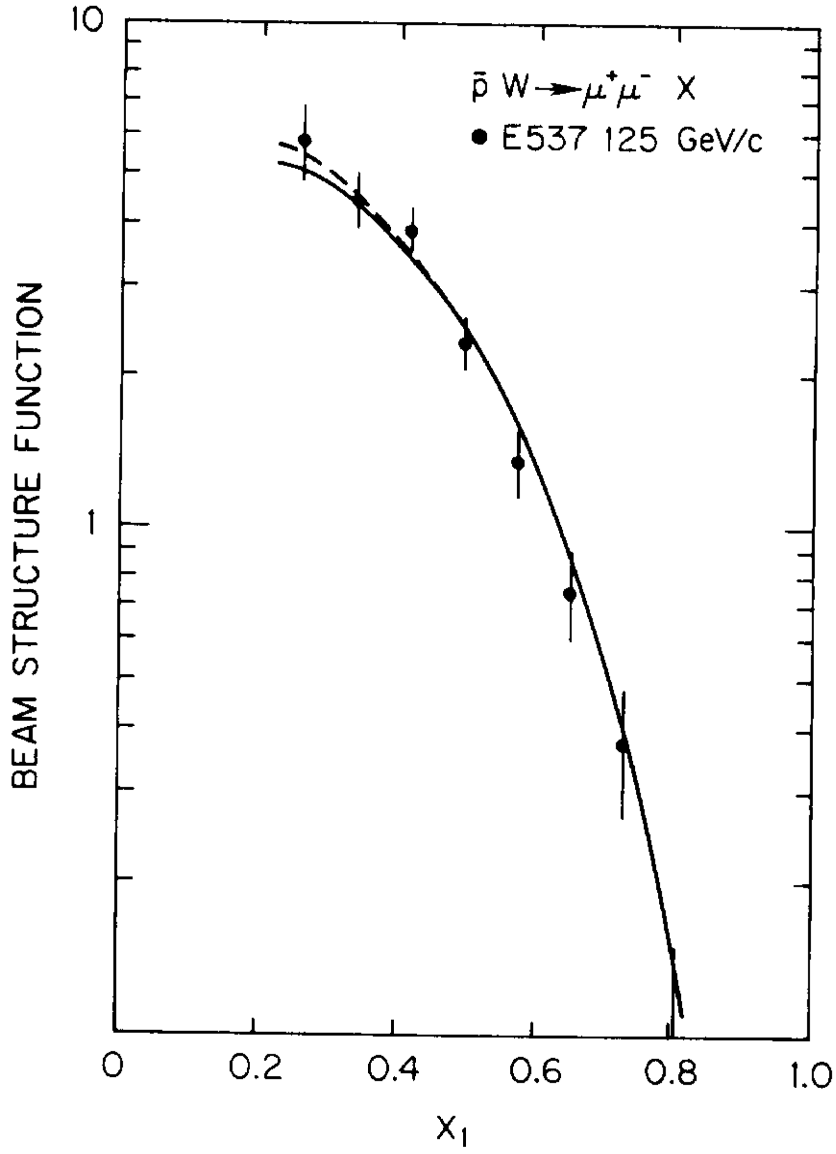

$\bar{p}\,W \to \mu^+\mu^-\;X$
● E537 125 GeV/c
BEAM STRUCTURE FUNCTION
10
1
0
0.2
0.4
0.6
0.8
1.0
X_1

Fig. 19

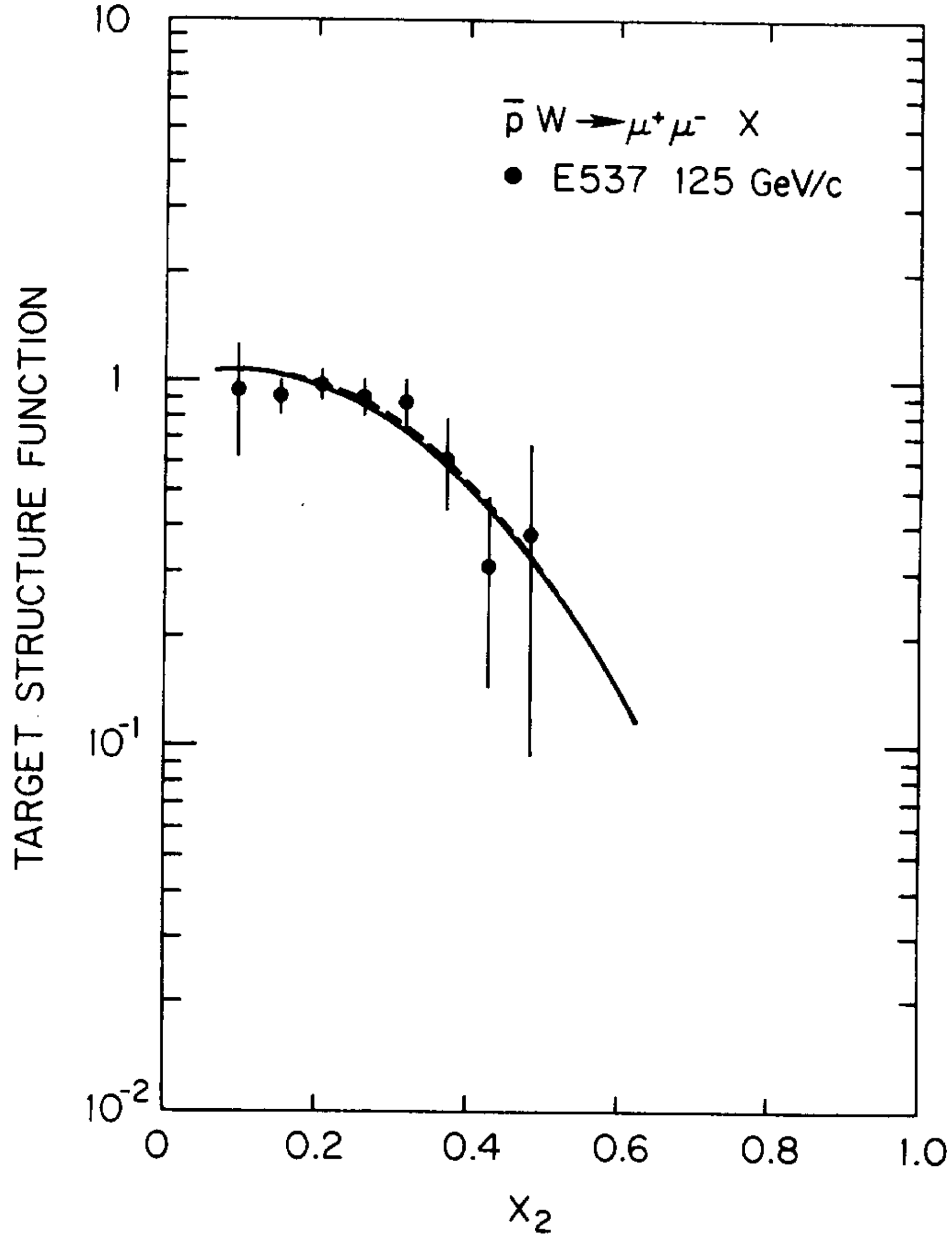

10
1
10^{-1}
10^{-2}
0
0.2
0.4
0.6
0.8
1.0
TARGET STRUCTURE FUNCTION
x_2
$\bar{p}W \to \mu^+\mu^- X$
● E537 125 GeV/c

Fig. 20

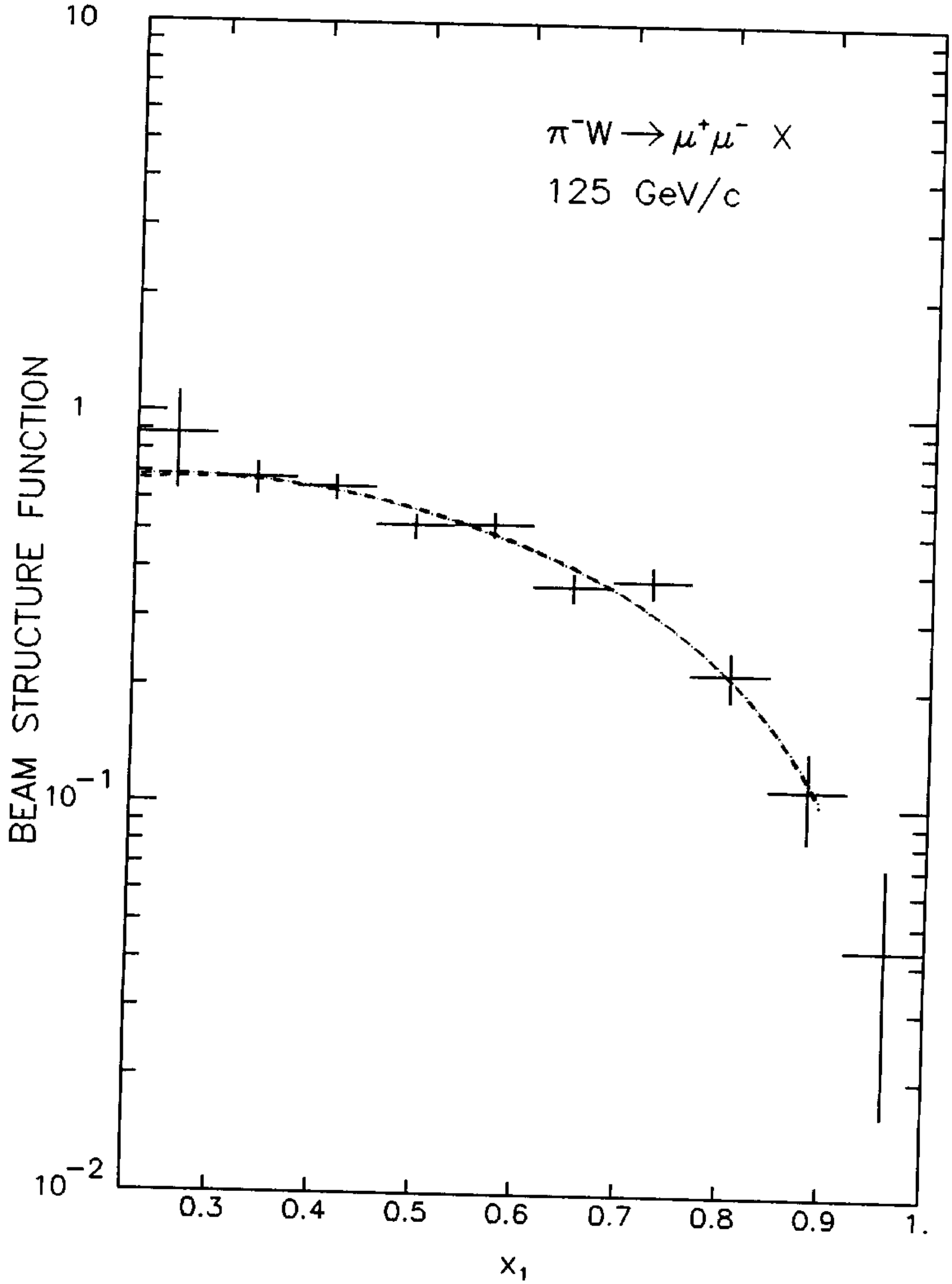

$\pi^- W \rightarrow \mu^+\mu^- X$
125 GeV/c
BEAM STRUCTURE FUNCTION
10
1
10^{-1}
10^{-2}
0.3
0.4
0.5
0.6
0.7
0.8
0.9
1.
x_1

Fig. 21

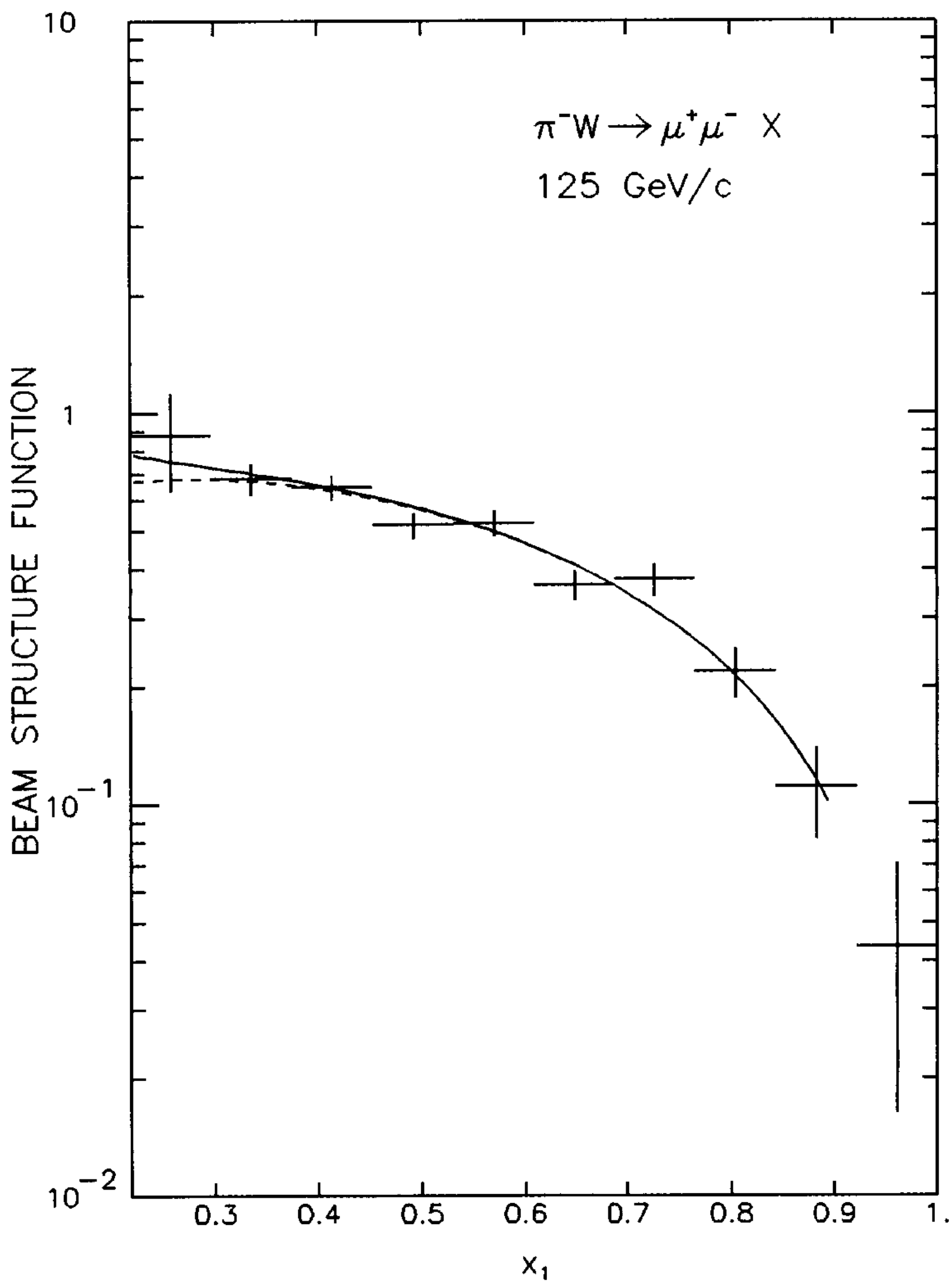

10
1
10^{-1}
10^{-2}
BEAM STRUCTURE FUNCTION
$\pi^- W \rightarrow \mu^+ \mu^- X$
125 GeV/c
0.3
0.4
0.5
0.6
0.7
0.8
0.9
1.
x_1

Fig. 22

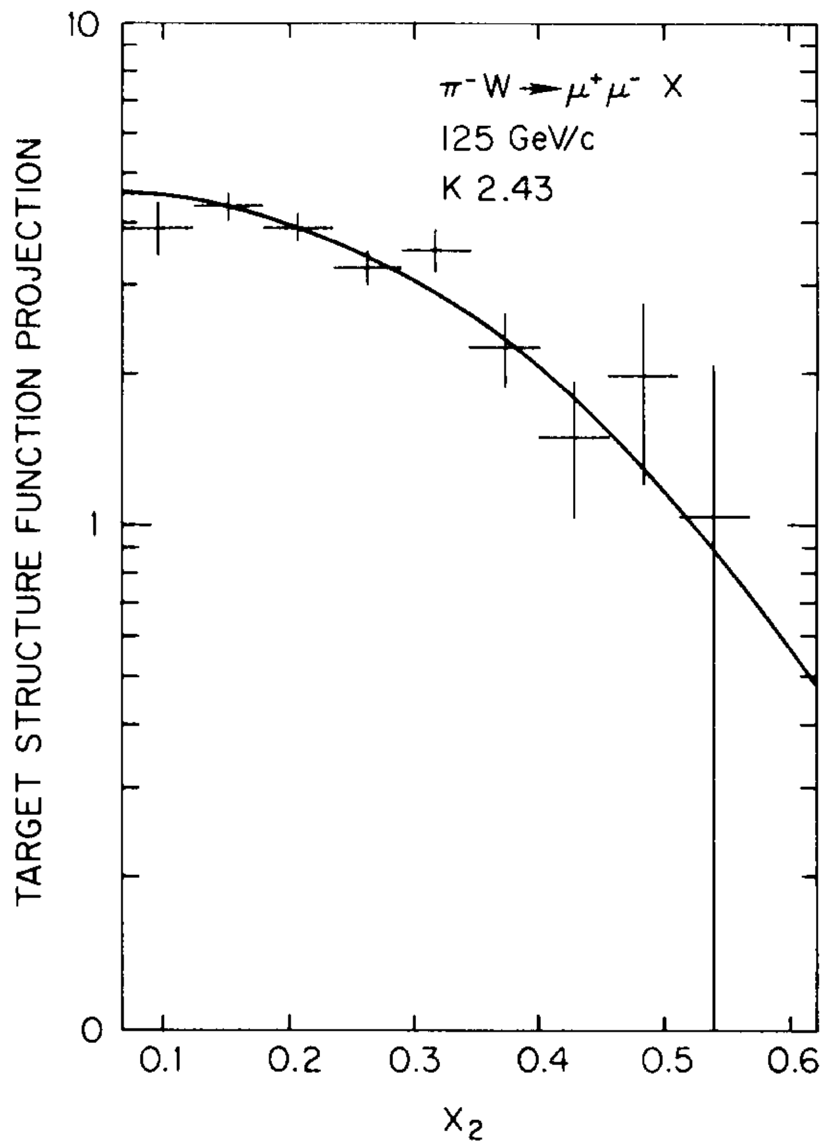
$\pi^- W \rightarrow \mu^+ \mu^- X$
125 GeV/c
K 2.43
TARGET STRUCTURE FUNCTION PROJECTION
10
1
0
0.1
0.2
0.3
0.4
0.5
0.6
X_2

Fig. 23

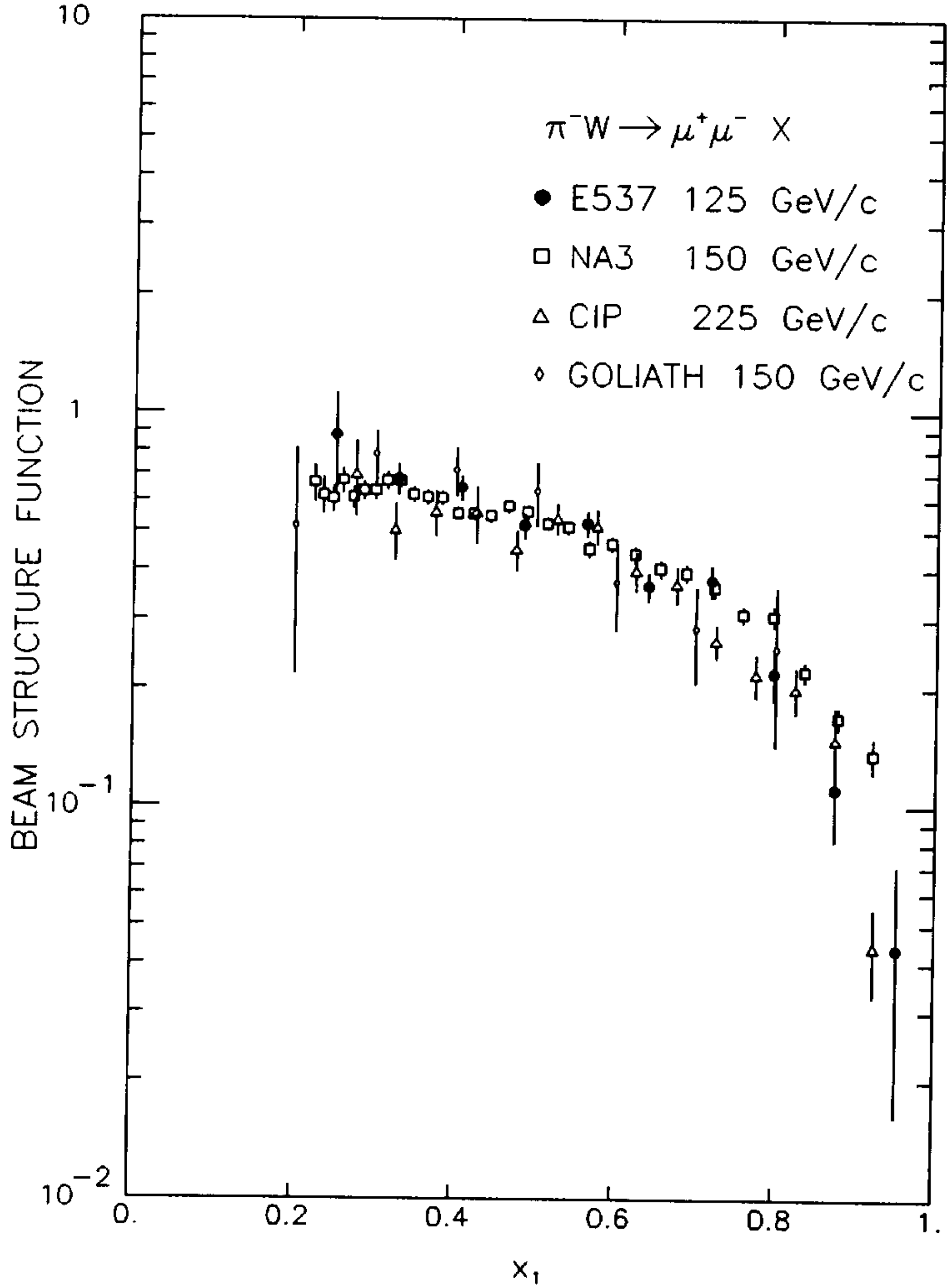

$\pi^- W \to \mu^+ \mu^- X$
● E537 125 GeV/c
□ NA3 150 GeV/c
△ CIP 225 GeV/c
◇ GOLIATH 150 GeV/c
BEAM STRUCTURE FUNCTION
10
1
10^{-1}
10^{-2}
0.
0.2
0.4
0.6
0.8
1.
x_1

Fig. 24a

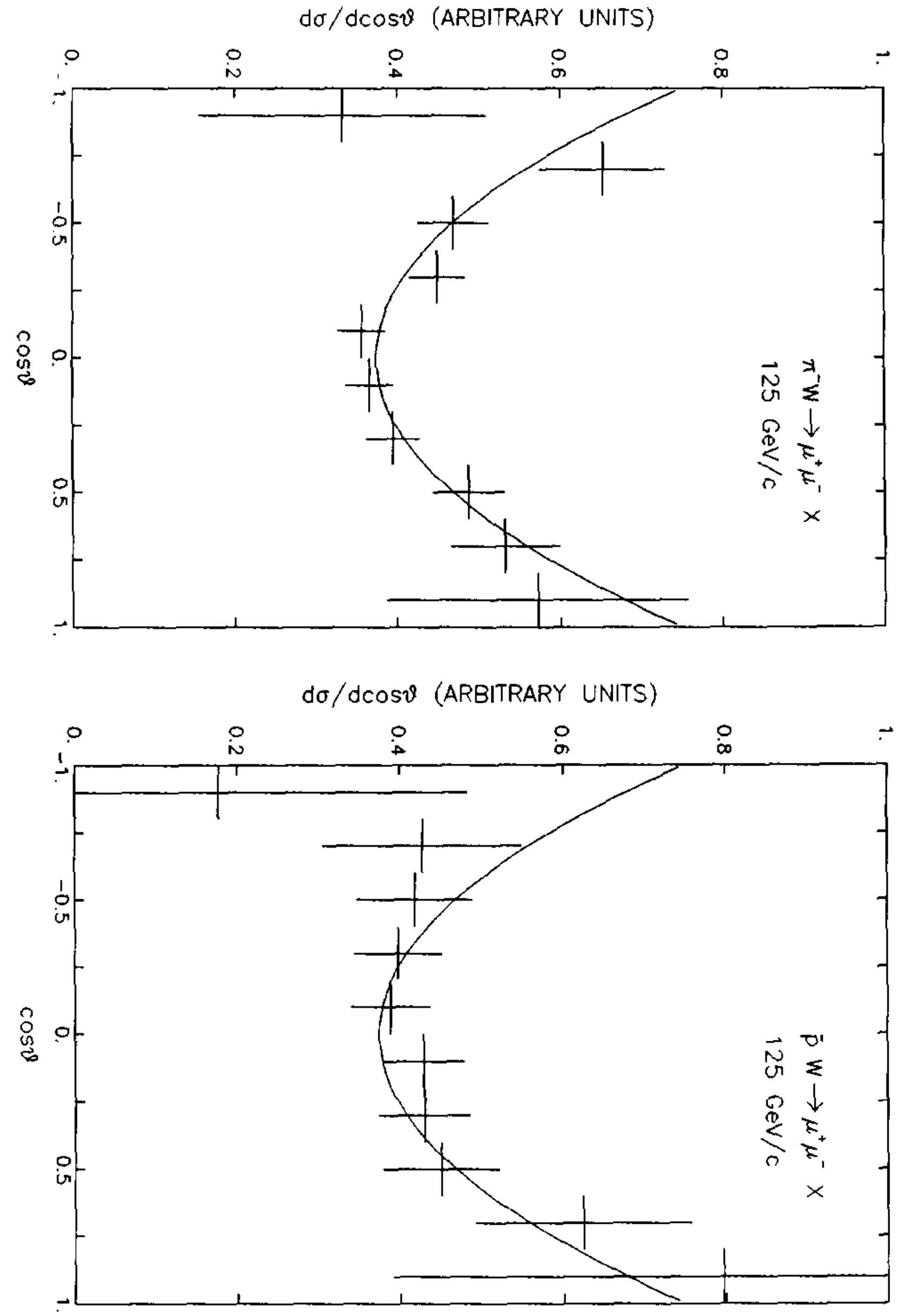

dσ/dcosϑ (ARBITRARY UNITS)
cosϑ
$\pi^- W \to \mu^+ \mu^- X$
125 GeV/c
dσ/dcosϑ (ARBITRARY UNITS)
cosϑ
$\bar{p}\, W \to \mu^+ \mu^- X$
125 GeV/c

Fig. 24b

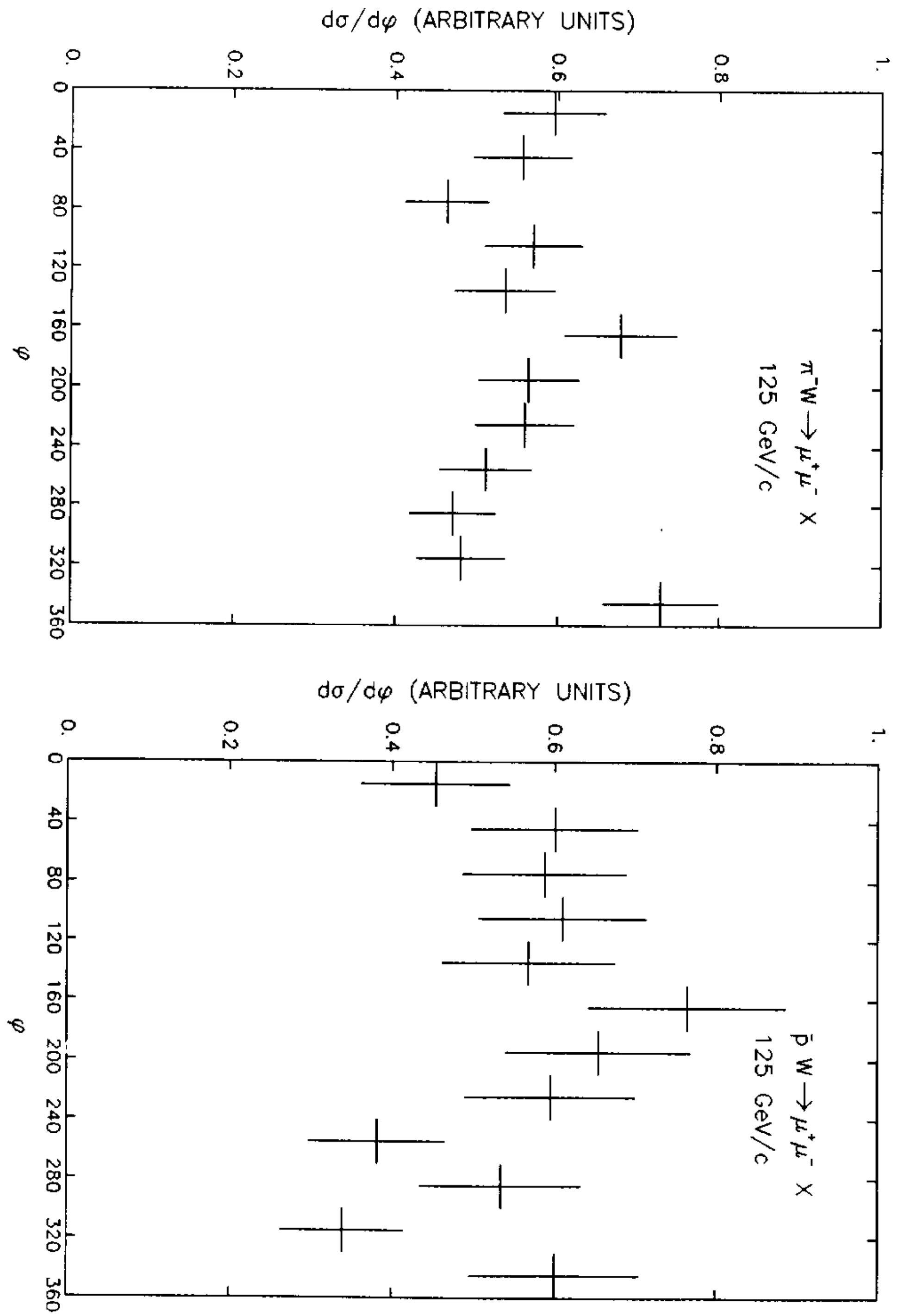
dσ/dφ (ARBITRARY UNITS)
0. 0.2 0.4 0.6 0.8 1.
0 40 80 120 160 200 240 280 320 360
φ
$\pi^- W \to \mu^+\mu^- X$
125 GeV/c
dσ/dφ (ARBITRARY UNITS)
0. 0.2 0.4 0.6 0.8 1.
0 40 80 120 160 200 240 280 320 360
φ
$\bar{p} W \to \mu^+\mu^- X$
125 GeV/c

Fig. 25a,b

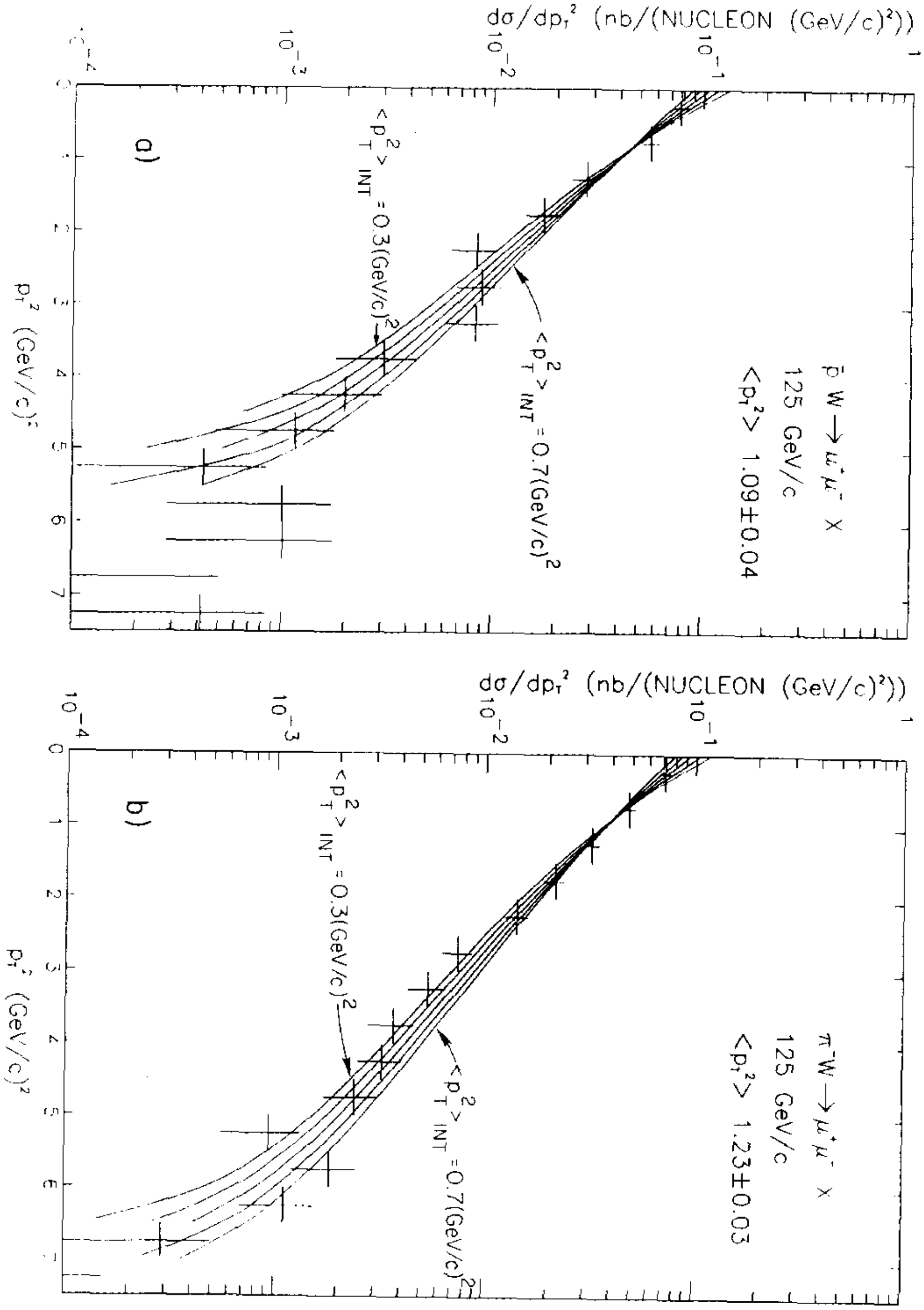

a)
$\bar{p}W \to \mu^+\mu^- X$
125 GeV/c
$\langle p_T^2 \rangle$ 1.09±0.04
$\langle p_T^2 \rangle_{INT}$ =0.3(GeV/c)^2
$\langle p_T^2 \rangle_{INT}$ =0.7(GeV/c)^2
$d\sigma/dp_T^2$ (nb/(NUCLEON (GeV/c)^2))
p_T^2 (GeV/c)^2
b)
$\pi^- W \to \mu^+\mu^- X$
125 GeV/c
$\langle p_T^2 \rangle$ 1.23±0.03
$\langle p_T^2 \rangle_{INT}$ =0.3(GeV/c)^2
$\langle p_T^2 \rangle_{INT}$ =0.7(GeV/c)^2
$d\sigma/dp_T^2$ (nb/(NUCLEON (GeV/c)^2))
p_T^2 (GeV/c)^2

Fig. 25c,d

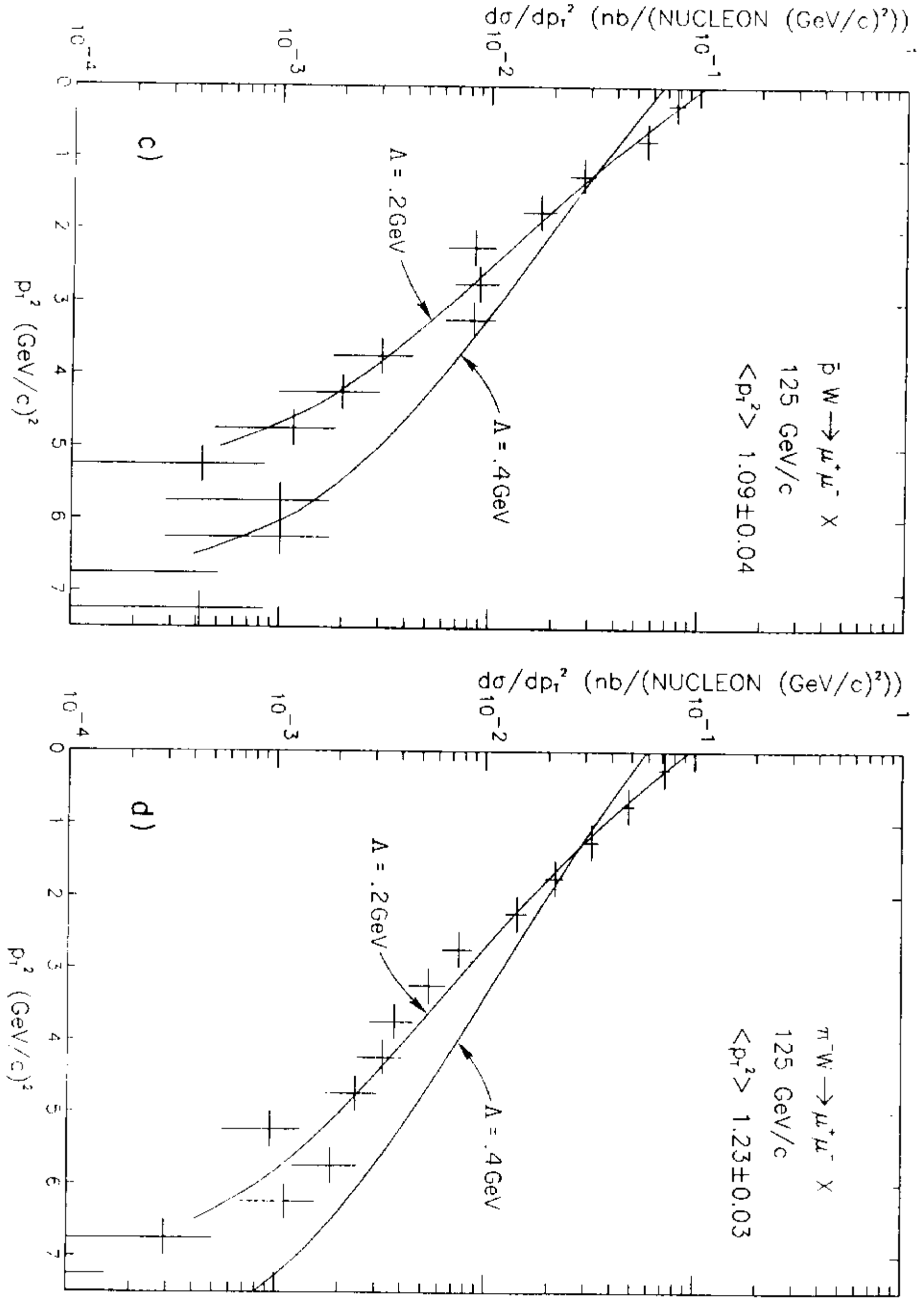

$d\sigma/dp_T^2$ (nb/(NUCLEON (GeV/c)^2))
c)
Λ = .2GeV
Λ = .4GeV
$\bar{p}W \rightarrow \mu^+\mu^-$ X
125 GeV/c
$\langle p_T^2 \rangle$ 1.09±0.04
p_T^2 (GeV/c)^2
$d\sigma/dp_T^2$ (nb/(NUCLEON (GeV/c)^2))
d)
Λ = .2GeV
Λ = .4GeV
$\pi^-W \rightarrow \mu^+\mu^-$ X
125 GeV/c
$\langle p_T^2 \rangle$ 1.23±0.03
p_T^2 (GeV/c)^2

Fig. 26

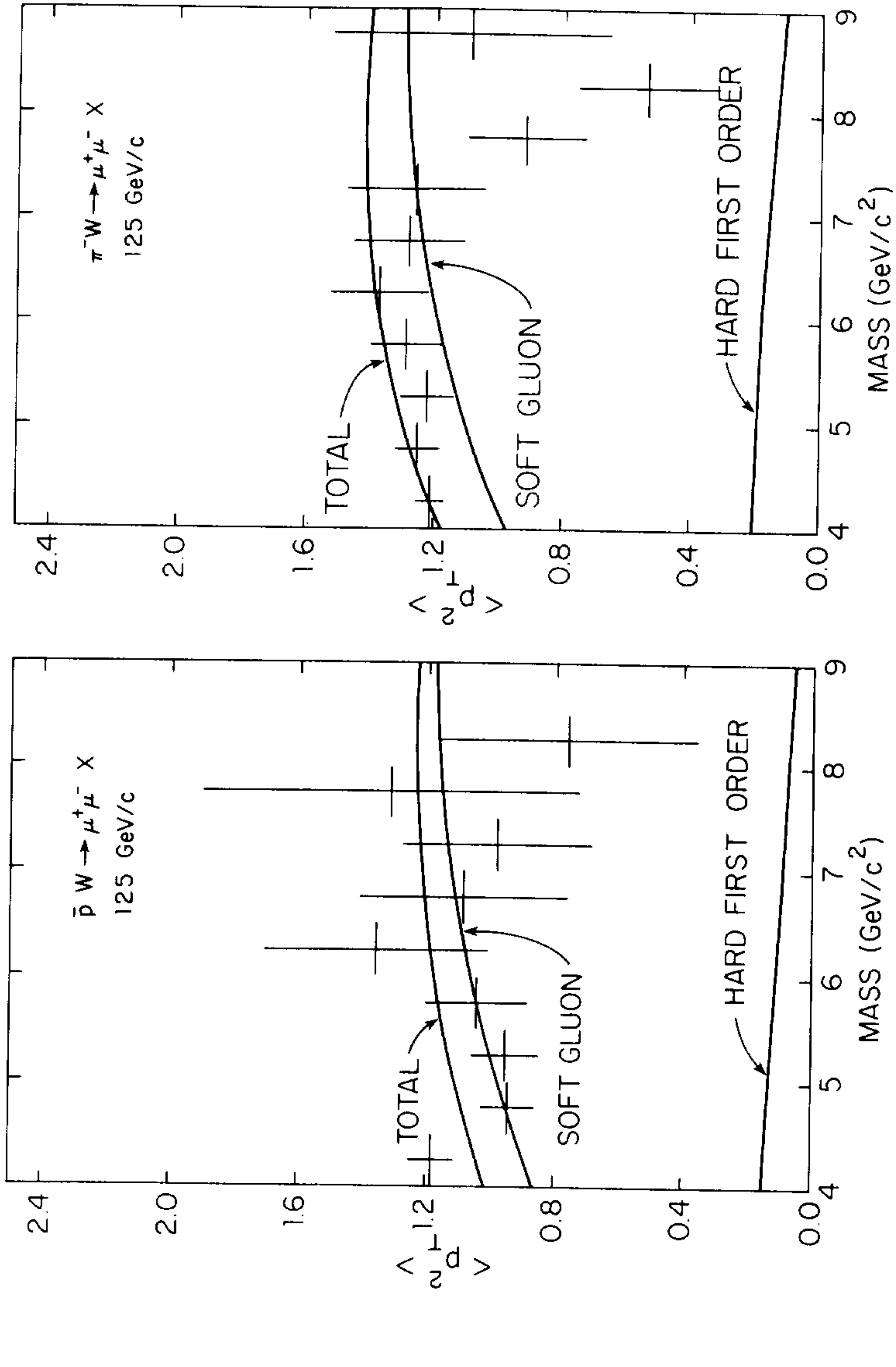

$\pi^- W \rightarrow \mu^+\mu^- X$
125 GeV/c
TOTAL
SOFT GLUON
HARD FIRST ORDER
$\langle p_T^2 \rangle$
MASS (GeV/c^2)
$\bar{p}\, W \rightarrow \mu^+\mu^- X$
125 GeV/c
TOTAL
SOFT GLUON
HARD FIRST ORDER
$\langle p_T^2 \rangle$
MASS (GeV/c^2)

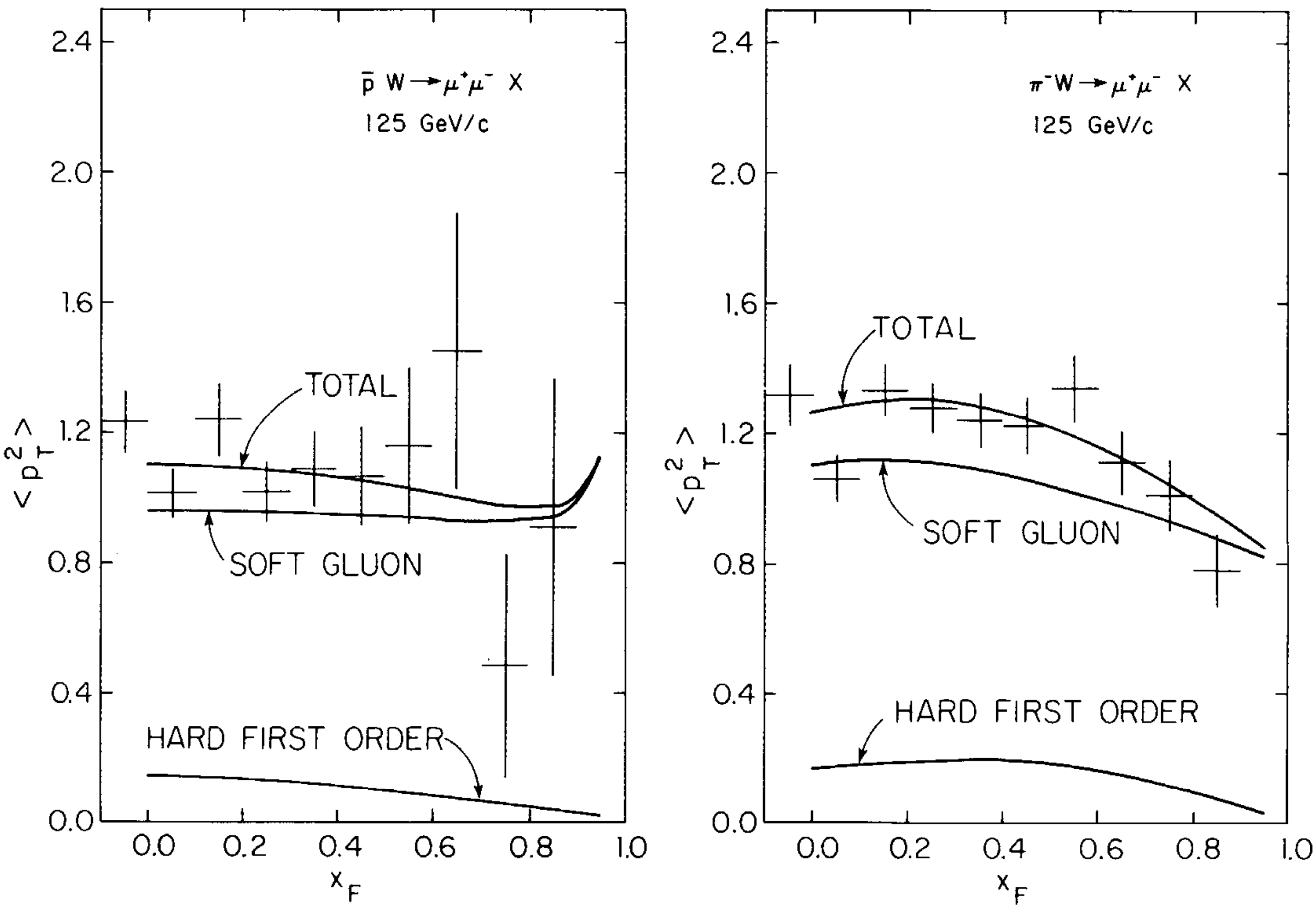
$\bar{p}\,W \rightarrow \mu^+\mu^-\,X$
125 GeV/c
$\pi^- W \rightarrow \mu^+\mu^-\,X$
125 GeV/c
TOTAL
SOFT GLUON
HARD FIRST ORDER
$\langle p_T^2 \rangle$
x_F
2.4
2.0
1.6
1.2
0.8
0.4
0.0
0.2
0.6
1.0

Fig. 27